Genomic architecture of the self-incompatibility locus in apple provides insights into the evolution of collaborative non-self recognition

Aurélie Mesnil[1,2], Vincent Castric[3], Gianluca Lombardi[4], Marie Monniaux[3], Somia Saidi[1,5], Xilong Chen[1,2], William Marande[6], Johann Confais[5], Anne-Laure Fuchs[1], Enrique Dapena[7], Anthony Venon[1,2], Takashi Tsuchimatsu[8], Alessandra Carbone[4,9], Xavier Vekemans[3], Amandine M. Cornille[1,2]

1 Université Paris Saclay, INRAE, CNRS, AgroParisTech, GQE-Le Moulon, Gif-sur-Yvette, France
2 Division of Science, New York University Abu Dhabi, Saadiyat Island, Abu Dhabi, United Arab Emirates
3 Univ. Lille, CNRS, UMR 8198 – Evo-Eco-Paleo, F-59000 Lille, France
4 Sorbonne University, CNRS, IBPS, Computational, Quantitative and Synthetic Biology Department, UMR 7238, Paris, France
5 Université Paris-Saclay, INRAE, BioinfOmics, URGI, 78026 Versailles, France
6 CNRGV, INRAe Toulouse, France
7 SERIDA, Villaviciosa, Spain
8 Graduate School of Science, The University of Tokyo, Japan
9 Institut Universitaire de France

Abstract

Self-incompatibility (SI) systems prevent self-fertilization, thereby maintaining genetic diversity in flowering plants. Among them, collaborative non-self recognition (CNSR) is the most widespread, yet its genomic architecture remains poorly understood. Using 27 haplotype-resolved genomes from wild and domesticated apples (*Malus* spp.), we dissected the structure and evolution of the S-locus. We identified 17 S-RNase alleles and 500 pollen-expressed S-locus F-box brother (SFBB) genes across 18 families. The S-locus exhibits hallmark features of a supergene, including suppressed recombination, TE accumulation, and an excess of non-synonymous polymorphisms. Nonetheless, long-term balancing selection preserves both the integrity and diversity of entire S-haplotypes. Recurrent associations between SFBB families and transposable elements, coupled with gene conversion signatures, suggest a dynamic mechanism for reshuffling recognition specificities. Our results provide a detailed view of how a multigenic, tightly linked recognition system is maintained in a woody perennial, and highlight the

interplay between structural constraints and selection in sustaining functional diversity and reproductive barriers.

Main

Self-incompatibility (SI) prevents self-fertilization and enforces outcrossing in many flowering plants, thereby maintaining genetic diversity and long-term adaptation[1–3]. In the Maleae tribe of the Rosaceae family, containing *Malus* species (the apple trees), SI is primarily controlled by a gametophytic self-incompatibility locus (S-locus) that encodes the S-RNase, acting as a pistil-side toxin, and a multigene family of S-locus F-box brothers (SFBBs), which serve as pollen-side anti-toxins[4,5]. This collaborative non-self recognition (CNSR) system necessitates multiple SFBB proteins to recognize and neutralize non-self S-RNases, allowing successful fertilization under outcrossing[6,7]. While empirical investigations into this mechanism have advanced in model species from other flowering plant families, such as *Petunia* (Solanaceae)[8] and *Antirrhinum* (Plantaginaceae)[9], the complex genomic organization and evolutionary dynamics of the CNSR system of Maleae within Rosaceae remain incompletely understood.

Building on this framework, previous studies indicate that the S-locus may develop features of a supergene, such as structural rearrangements, recombination suppression, and long-term balancing selection that maintain co-adapted gene complexes[10–12]. However, the extent to which these features apply to SI loci remains poorly documented. In particular, the mechanisms behind SFBB expansion, diversification, and maintenance—including tandem duplications, gene conversion, transposable elements (TEs), and selective pressures—are still unclear[13,14]. Theoretical investigations suggest that natural selection will favor S-haplotypes that are as "complete" as possible, meaning that they possess pollen anti-toxins covering all S-RNase alleles found in the population, except the one carried by its own haplotype[15,16]. Hence, it is expected that genomic processes will tend to reach this optimal. However, some recent realistic simulations suggest that the dynamic nature of these processes could lead to substantial variation in the anti-toxin composition of S-haplotypes encoding the same S-RNase[17]. Here, we present the first haplotype-resolved characterization of the S-locus in *Malus*, leveraging 27 high-quality phased S-haplotypes from both wild and cultivated apple genomes. We annotated 500 SFBB genes, revealing 18 distinct phylogenetic families, and examined their patterns of duplication, diversification, and co-association with *S*-RNases. Using structural modeling, codon-level selection analysis, and genome-wide TE mapping, we reveal that tandem duplications, positive selection, and

gene conversion — possibly involving nearby TEs — contribute to SFBB turnover across haplotypes. Despite extensive divergence, S-haplotypes preserve conserved *S*-RNase–SFBB combinations, consistent with a non-self recognition model under balancing selection.

Our findings highlight the *Malus* S-locus as a compelling model to study how genomic structure and evolutionary processes interact to maintain multigenic recognition systems. They also raise broader questions about the genomic limits of diversification and recognition capacity in long-lived perennials under strong selective pressures.

Results

Conserved genomic architecture of SI loci with the same S-allele

To investigate the genome architecture and evolution of the S-locus in *Malus*, we analyzed 27 fully assembled S-haplotypes (Supplementary Table 1, Supplementary Fig. 1), including 14 from *M. domestica* (12 dessert, two cider) and 13 from wild relatives (*M. sylvestris, M. sieversii*, *M. orientalis*). At the S-locus located in chromosome 17, each haplotype contained a single S-RNase gene, which grouped into 17 clearly distinct allelic lineages (Supplementary Table 3, Fig. S1A). A 100% amino acid identity was typically observed between gene copies within alleles (Supplementary Fig. 1B), indicating strong purifying selection. One exception, haplotype h32 from *M. orientalis*, exhibited only 66.9% similarity with two MdS9 allele sequences from *M. domestica*. Controlled pollinations are necessary to confirm phenotypic recognition equivalence. Several wild haplotypes carried previously uncharacterized alleles (h24, h25, h29, h31). The *S*-RNase phylogeny (Supplementary Fig. 2a) was incongruent with the species tree (based on chromosome 17 single-copy genes), showing extensive interspecific allele sharing. This pattern is consistent with ancestral trans-species polymorphism, which is expected for an S-locus subject to long-term balancing selection[18], or with adaptive introgression between species[19,20].

We identified 500 intron-less SFBB genes (17–20 per haplotype; ~1.2 kb each), carrying a 5′ F-box domain and a 3′ FBA domain (Supplementary Text 1, Supplementary Table 6). These gene sequences clustered into 18 phylogenetic families, labeled SFBB1 to SFBB18 (Supplementary Text 1, Supplementary Table 6, Supplementary Fig. 3). We compared the presence/absence patterns of each SFBB family across different S-haplotypes, defined by the evolutionary tree of *S-RNase* genes (Fig. 1a, b). Each *S*-haplotype had a specific combination of SFBB families, which was strongly associated with its *S*-RNase allele (Mantel test, *p*-value = 0.024, Fig. 1c). For example, the *M. orientalis* h32 SFBB repertoire was nearly identical to that of the two *M. domestica MdS9* haplotypes, except for a duplication

of the SFBB3 family. Moreover, the SFBB gene order was highly conserved within haplotypes carrying the same *S*-RNase (Fig. 1c), with some minor differences (e.g., h3 vs. other *MdS2* haplotypes) that may reflect assembly quality (Supplementary Fig. 4, see quality assembly index (LAI)). Large syntenic blocks with low overall structural divergence were observed between haplotypes sharing the same allele even when they belonged to different species (Fig. 2a), suggesting strong constraints on SFBB organization.

In contrast, haplotypes with different *S*-RNases exhibited more divergent architectures (Fig. 1d), although some gene blocks (e.g., SFBB4 to SFBB6 and SFBB5 to SFBB14) were consistently located at the 5′ and 3′ ends, respectively. Central regions were more structurally variable and harbored more inversions and unaligned segments (Fig. 2b, Supplementary Fig. 5). Haplotypes sharing *S*-RNases had significantly longer synteny blocks ($p < 2.2e{-}16$). At the same time, those with different alleles had larger inversion sizes ($p = 1.3e{-}4$), supporting the role of structural variation in maintaining S-haplotype divergence.

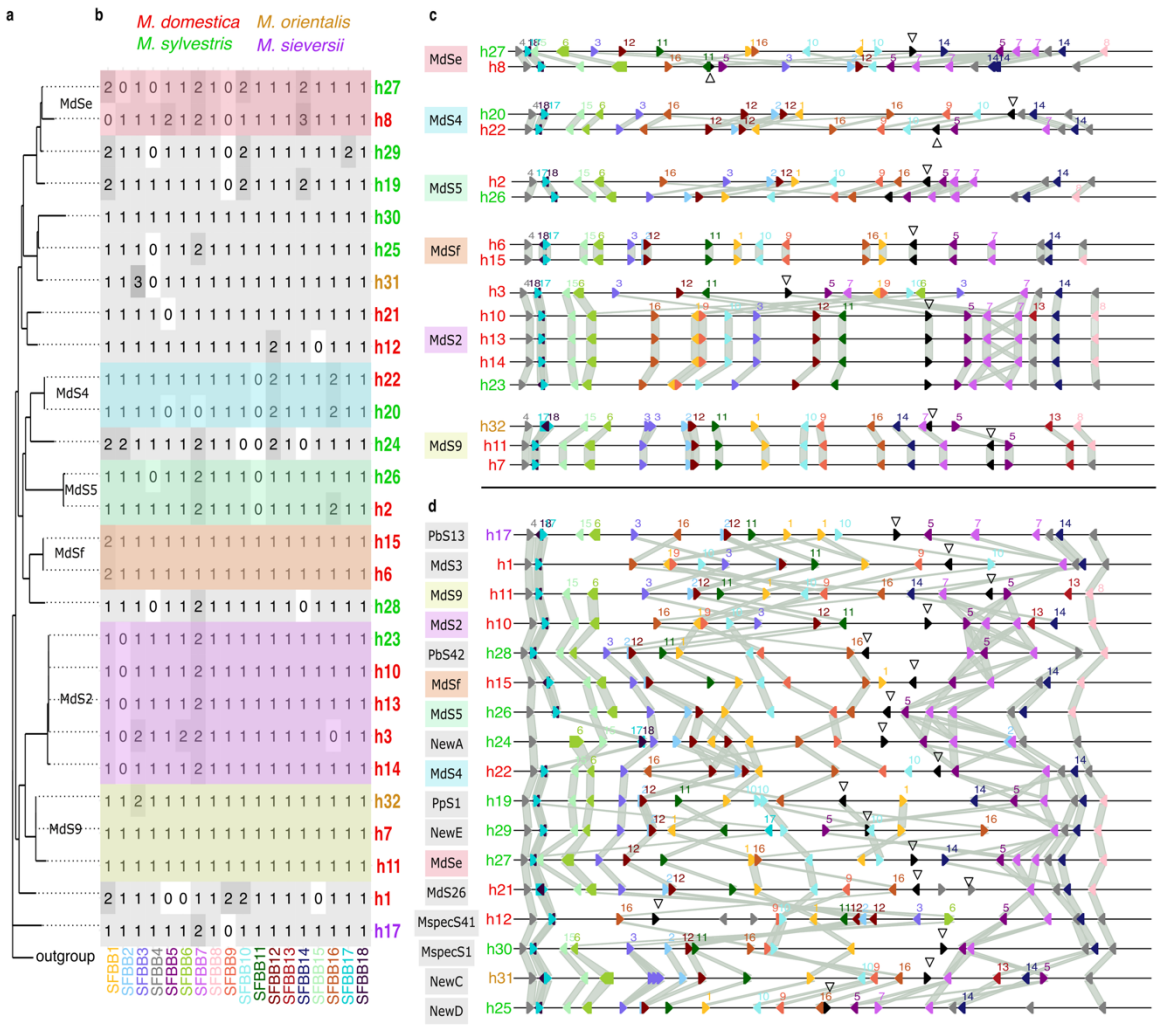

Fig. 1: Fig. 1 | Evolution, diversity, and organization of the S-locus in wild and cultivated apples. **(a)** Phylogenetic tree of S-RNase protein sequences across 27 S-haplotypes (labeled h1–h30). **(b)** Heatmap showing SFBB family counts per S-haplotype (rows) and gene family (columns). **(c)** Gene organization of SFBBs (colored by family) and S-RNase (black arrowhead) within the S-locus across haplotypes sharing the same S-RNase allele. Gray ribbons link orthologous SI genes. **(d)** S-locus structure across haplotypes with different S-RNase alleles; locus lengths are normalized to h30 for comparison.

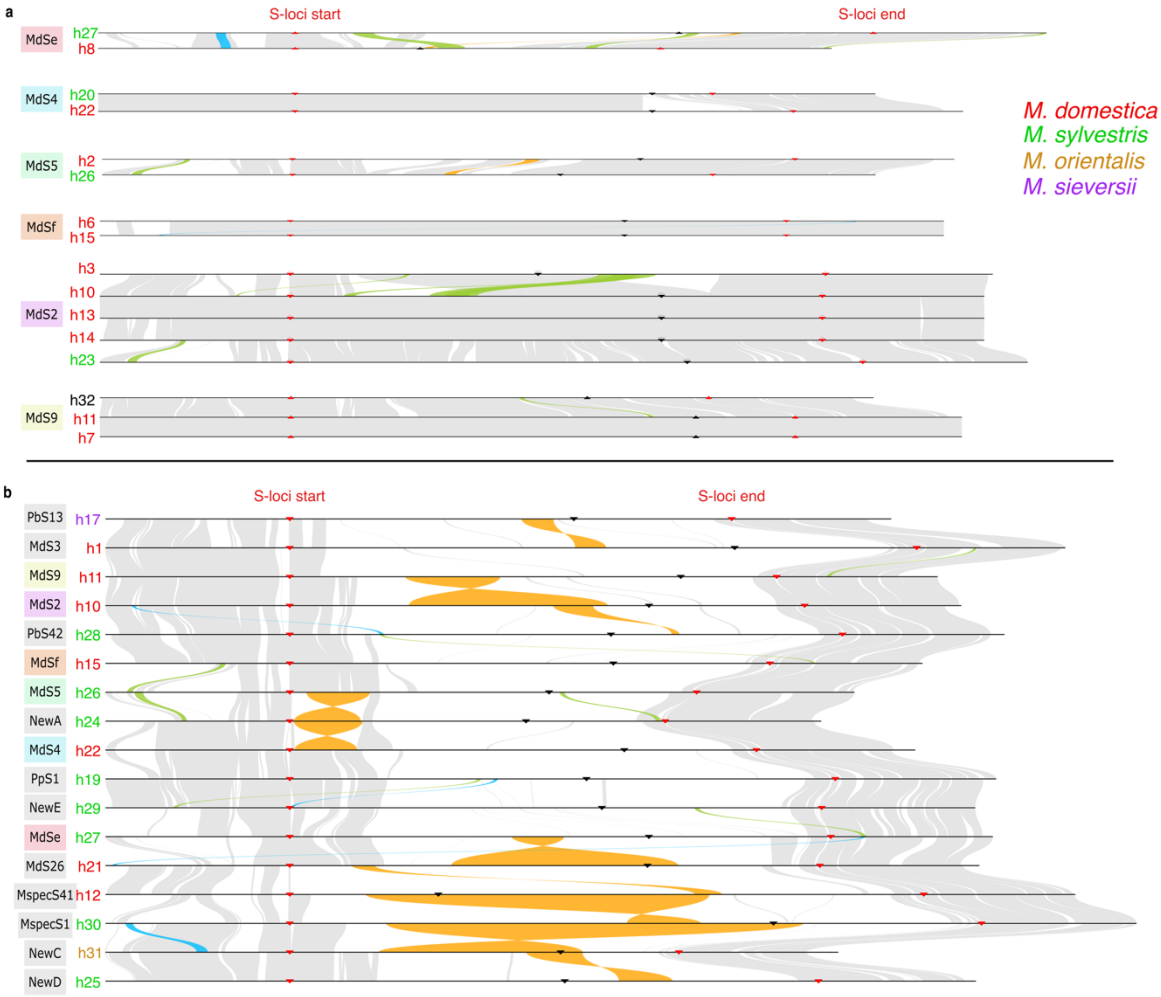

Fig. 2: Structural variation at the *Malus* S-locus.

(a) Whole-locus alignments of haplotypes sharing the same S-RNase (as in Fig. 2c) showing conserved synteny and structural rearrangements detected by SyRI (Synteny and Rearrangement Identifier). Colored curves represent syntenic blocks and rearrangements.

(b) Whole-locus alignments of haplotypes carrying different S-RNase alleles (as in Fig. 1d), highlighting greater structural divergence. Structural variant contributions are quantified in Supplementary Fig. 5. Alignments extend 500 kb upstream and downstream of the S-locus. Red triangles mark locus boundaries; black triangles mark S-RNase gene positions.

Each S-haplotype includes one S-RNase and several SFBB genes, which are key parts of the SI system in the Malae tribe[5]. We also identified the limits of the S-locus using conserved flanking genes,

including an upstream NF-Y gene and two downstream PI3/PI4 kinase family genes. The locus averaged 1.35 Mb (±0.11). It contained about 42 annotated genes, approximately three times fewer than observed in matched control regions (Supplementary Fig. 6). Consequently, it was highly enriched in TEs, particularly LTRs (~85% *vs.* 70% genome-wide, Supplementary Fig. 7a,c, Wilcoxon-Mann-Whitney test, p-value = 2.9e−10). *S*-locus annotated genes were grouped into 55 orthologous clusters using Syntenet[21], classified into four categories (Supplementary Fig. 8, Supplementary Table 7). Apart from SFBB and *S*-RNase genes, 38 clusters encoded diverse functions (e.g., kinases, transcription factors, transporters), suggesting possible recruitment or retention due to structural dynamics or regulation. Gene content clustering across haplotypes revealed both conserved and variable clusters (Supplementary Fig. 2b), with high TE content and variable gene presence, reinforcing the view of the *S*-locus as a structurally dynamic region.

Genetic diversity (π)[22,23] computed in sliding windows peaked in the *S*-locus region in all four species, especially in *M. sylvestris* and *M. sieversii*, and was significantly enriched in the top 1% π windows (empirical $p < 0.05$; Supplementary Fig. 9), supporting long-term balancing selection. To avoid confounding effects of positive selection acting on SFBB genes, variants located within SFBB coding regions were excluded from subsequent analyses of coding variation. Even after this filtering, we observed an excess of non-synonymous substitutions (nS/S > 1; Supplementary Fig. 10), consistent with supergene-like behavior, where recombination suppression reduces purifying selection and promotes mutation accumulation[24].

Finally, comparing across species, with different CNSR systems, the number of SFBB genes and families in *Malus* (~18) was similar to that in *Petunia* (~18 SLFs)[13] but lower than in *Antirrhinum* (~32 SLFs)[9] (Table 1).

150 **Table 1. Comparative architecture of the S-locus across flowering plants with CNSR SI systems.**
151 Summary of key genomic features of the S-locus across species with collaborative non-self
152 recognition (CNSR)-based self-incompatibility. Shown are the number of pollen-expressed genes
153 (SFBBs or SLFs), S-locus size (Mb), number of gene families (from sequence/function-based
154 clustering), chromosomal position (when known), and references. Data are drawn from published
155 studies and the present work (Malus). In species like *Petunia* and *Citrus*, the S-locus was inferred
156 from BACs or partial assemblies.

Model	**Plant family**	**Number of pollen genes**	**Mean size of the S-locus (Mb)**	**Number of pollen gene families**	**Location**	**References**
Apple (*Malus*)	Rosaceae	16–20 *SFBB*s	1.35	18	Peri-telomeric, long arm of chromosome 17 (17 chromosomes)	This study
Snapdragon (*Antirrhinum*)	Plantaginaceae	32 *SLF/SFB*	1.20	31	Peri-telomeric, short arm of chromosome 8 (8 chromosomes)	[9,25]
Potatoes	Solanaceae	12 *SLF*s	13	8	Chromosome 1 (12 chromosomes)	[26]
Petunia	Solanaceae	16–20 *SLF*s	Unknown	18	Sub-centromeric, chromosome 3 (7 chromosomes)	[13,27]
Coffea	Rubiaceae	Unknown	0.008	Unknown	Chromosome 5 (11 chromosomes)	[28]
Citrus	Rutaceae	11–17 *SLF*s	0.198 to 0.370 (BAC)	12	Unknown	[14,29]
Pyrus and *Malus*	Rosaceae	17–21 SFBBs	1.35 to 2.64	22	Peri-telomeric, long arm of chromosome 17 (17 chromosomes)	[30]

Pineapple (*Ananas*)	Bromeliaceae (Monocot)	Unknown	Unknown	Unknown	LG02 (25 chromosomes)	[31]

157

158 **Multiple evolutionary and genomic mechanisms contribute to *SFBB* gene diversification and**
159 **maintenance within the *Malus* S locus**
160 A major question regarding S-locus architecture is how new recognition specificities are generated and
161 maintained with multiple pollen determinant genes and how they spread across S-haplotypes with
162 different *S-RNase* alleles[15–17]. We obtained several lines of evidence suggesting that multiple
163 evolutionary forces shape the diversity of *SFBB* genes within the *Malus* S-locus. Together, our results
164 support a model where tandem duplication, gene conversion, and positive selection promote SFBB
165 diversification (Fig. 3f), while structural and functional constraints maintain recognition compatibility
166 with resident S-RNase alleles, preserving a diversified but tightly co-adapted SI system in *Malus*.
167 First, tandem and proximal duplications were found to be the dominant modes contributing to
168 SFBB expansion (Fig. 3a), contrasting with segmental duplications that dominated elsewhere in
169 chromosome 17. These local duplications likely provided the raw material for functional diversification
170 of S-alleles. Secondly, signatures of positive selection (dN/dS > 1, Supplementary Table 8) were
171 detected in SFBBs, with CodeML identifying codons under strong positive selection (Fig. 3b,
172 Supplementary Table 9). Several of these residues were conserved across multiple S-haplotypes and
173 were significantly associated with specific SFBB families (Table 2, Supplementary Table 10). These
174 amino acids (aa) clustered in regions of predicted surface interaction based on Boltz-1 structural
175 modeling[32] (Supplementary Fig. 13) and exhibited high MuLAN local attention scores, suggesting
176 functional relevance[33] (Supplementary Fig. 12). Multivariate analysis of aa positions across families
177 supported this pattern of divergence (Supplementary Fig. 11).
178 In parallel, we observed strong sequence conservation within SFBB families despite their
179 occurrence on divergent S-haplotypes (Fig. 3d, Supplementary Table 11), consistent with inter-
180 haplotype gene conversion. A quasi-Poisson model identified allele pairs with significantly elevated
181 conversion rates (MdS2–MspecS1, MdS2–MdSe, MdS2–MdSf), independent of their phylogenetic
182 distance (Supplementary Fig. 14). Gene conversion events were also inferred from the recurrent
183 association of specific SFBB families with nearby TEs, within 4 kb (Fig. 3e, Supplementary Fig. 15,
184 Supplementary Table 12). These SFBB–TE pairs were significantly more frequent than expected under
185 random association models (permutation test, $p \leq 0.01$) and were observed across multiple S-haplotypes
186 carrying distinct S-RNase alleles. The TE consensus sequences enriched for such associations do not
187 belong to any specific classification (Supplementary Table 13), but all of these consensus sequences
188 correspond to incomplete copies, with match on RepBase[34]. Such conserved SFBB–TE co-occurrences,
189 along with similar distances to TE consensus and similar insertion ages (Supplementary Fig. 15a–b),

support the hypothesis of sequence block transfers across haplotypes, via gene conversion. Importantly, SFBB–TE associations remained correlated with specific S-RNase alleles, indicating that only compatible combinations were retained—suggesting strong post-conversion selection filters.

194 **Table 2 | Amino acid sites associated with SFBB gene families in Malus S-haplotypes.**
195 Summary of amino acid (aa) positions showing significant associations with SFBB gene families across
196 27 phased S-haplotypes. For each position, the number of aa variants, mean intra-family diversity, mean
197 number of families per site, and FDR-adjusted p-values from multinomial regression are shown. FBA:
198 F-box–associated domain. Positively associated sites highlight candidates for SFBB diversification and
199 allele-specific recognition. Full data in Supplementary Tables 10 and 13.

Amino acid position	SFBB domain	Total number of aa variants	aa diversity within families	Family diversity per aa	*p*-value	Adjusted *p*-value
297	–	10	1.33	2.40	1.1e−244	5.7e−244
299	–	10	1.44	2.60	3.0e−188	4.2e−188
336	FBA	11	2.22	3.64	5.0e−98	5.0e−98
356	FBA	7	1.50	3.86	4.9e−215	1.6e−214
358	FBA	11	1.28	2.09	2.2e−263	2.2e−262
421	FBA	11	1.83	3.00	9.0e−191	1.5e−190
429	FBA	10	1.39	2.50	3.5e−199	7.0e−199
476	FBA	7	1.39	3.57	3.8e−203	9. 5e−203
543	–	12	2.00	3.00	8.1e−175	1.0e−174
549	–	8	1.61	3.63	3.6e−166	4.0e−166

200

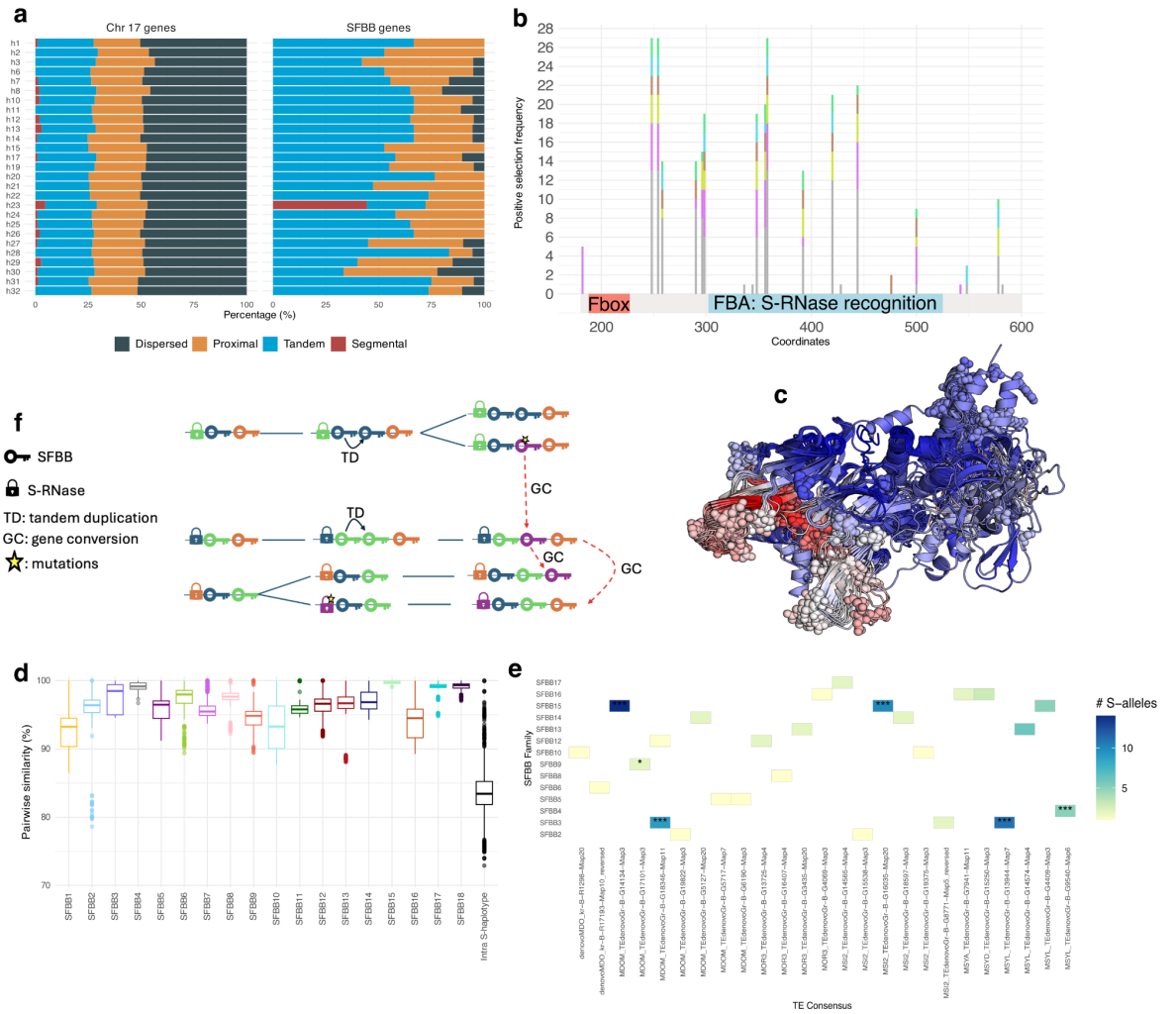

Fig. 3. Evolutionary forces shaping SFBB diversity at the *Malus* S-locus.

Central diagram illustrates the interplay of duplication, selection, gene conversion, and transposable elements (TEs) in SFBB diversification.

(a) Duplication modes for SFBB genes across haplotypes, compared with other chromosome 17 genes. Tandem duplications dominate SFBB expansion.

(b) Positively selected codons in SFBB proteins, primarily in the FBA domain but also in the interdomain region. Bar colors reflect associated S-RNase alleles; grey indicates unassigned alleles.

(c) In predicted SFBB model 3D structures (Boltz-1), selected residues cluster near S-RNase interaction surfaces. Superimposed SFBB models are colored with MuLAN attention scores; red-to-white colors correspond to high while blue tones to low scores. High attention scores indicate residue functional

importance. Note that the longest sequence for each S-allele was chosen as representative, totaling 17 sequences, and the resulting structures were aligned in PyMOL to minimize pairwise root mean square deviation of atomic positions.

(d) Sequence similarity of SFBB genes (Clustal Omega), comparing within-family (>90%) versus within-haplotype (~82%) identity.

(e) Heatmap of SFBB–TE co-occurrence across haplotypes. Colors indicate the number of distinct S-RNase alleles per association; asterisks denote significant associations (permutation test, 10,000 reps; $*p \leq 0.05$, $***p \leq 0.01$). See Supplementary Table 14.

Predicting molecular interactions between SFBB and S-RNase

S-RNase polymorphisms drive SI specificity and show pronounced hypervariability (Supplementary Fig. 16). Codon-based analyses identified eight positively selected codons conserved within each *S*-RNase allele and distributed across the coding region, not confined to hypervariable segments. Several sites lie outside previously predicted recognition regions[35,36], yet 3D models (Boltz-1; Supplementary Fig. 17) indicated surface exposure. MuLAN attention scores were generally low at these positions (Supplementary Fig. 18), suggesting sequence-based models alone incompletely capture functional relevance.

To identify candidate SFBB families responsible for detoxifying particular S-RNases, we examined pattern of presence/absence of different SFBBs across haplotypes sharing the same *S*-RNase. SFBB2 was absent from all MdS2 haplotypes (h14, h13, h3, h10, h23, Supplementary Table 13), suggesting its role in detoxifying MdS2 S-RNase. SFBB11 was absent from both MdS4 (h20, h22) and MdS5 (h2, h26) haplotypes (Supplementary Table 14), suggesting putative detoxification of multiple targets, as already demonstrated for some SLF families in *Petunia*[8]. Family-specific amino acid deviations at conserved positions also linked SFBB genes to particular *S*-alleles—for example, SFBB12 in MdS2 haplotypes consistently showed a non-consensus residue at position 299 (Supplementary Table 10). SFBB18 was universally present and unmutated at selected sites, suggesting a role in recognizing unrepresented *S*-RNases that were not represented in our study.

Despite these patterns, structural interactions predictions alone did not discriminate interacting from non-interacting SFBB – S-RNase pairs in *Malus*. Although Boltz-1 models yielded overall high confidence scores (pLDDT, pTM, i-pLDDT, i-pTM; pLDDT > 0.6, pTM > 0.3), score distributions for expected, unsupported and unknown interactions largely overlapped (Supplementary Fig. 19 and 20). Nevertheless, predictions for SFBB proteins alone, and, to a lesser extent, for S-RNase alone showed

245 higher and more consistent confidence values (pTM > 0.8, Supplementary Fig. 20 and 21), suggesting
246 that the structural models for single chains were more reliable than the SFBB-SRNase interaction
247 models.
248 The same pipeline applied to *Petunia*—with includes validated SLF–*S*-RNase interactions (S9-
249 SLF1, S9-SLF17)[8] —produced higher confidence scores (pLDDT > 0.8, i-pLDDT > 0.65, pTM > 0.7;
250 Supplementary Fig. 20, 21, 22 and 23). However, known and unknown interaction classes still
251 overlapped, showing that specificity is not resolved by these metrics. Chain-level i-pLDDT scores
252 further revealed a clear species difference: *Petunia* S-RNases consistently exhibit higher structural
253 confidence than *Malus* S-RNases, whereas SFBB/SLF proteins show similar score ranges in both genera
254 (Supplementary Fig. 22). This indicates that the structural predictions perform better for *Petunia* S-
255 RNases. However, interaction categories (expected, unsupported, unknown) remain fully intermixed
256 across the score space, indicating that global structural confidence does not resolve interaction
257 specificity. Noticeable, in *Petunia*, positively selected sites mapped to surface regions overlapping high
258 MuLAN scores (Supplementary Fig. 22–23).
259
260 **Discussion**
261 Higher rates of outcrossing in hermaphrodite plant species foster genetic diversity and adaptive potential
262 in plants[1–3], leading to higher macroevolutionary success[37]. In *Malus*, this is enforced by the S-locus,
263 where S-RNases and SFBB proteins mediate SI. Despite its importance, the genomic organization and
264 evolution of this locus have remained elusive due to the limited availability of reliable haplotype data.
265 Leveraging 27 fully resolved S-haplotypes, we present a comprehensive view of S-locus diversity,
266 highlighting extensive structural variation, dynamics of SFBB gene content, and signatures of
267 evolutionary forces acting on this system.
268
269 **Architecture and expansion of the *Malus* S-locus**
270 We confirmed the peri-telomeric position of the S-locus on chromosome 17 and estimated its size at
271 ~1.35 Mb, consistent with prior work in *Malus* and *Pyrus*[30]. Phylogenetic analysis assigned the 27
272 haplotypes to 17 distinct S-RNase alleles, with considerable redundancy in MdS2 and MdS9. On
273 average, 18.5 SFBB genes were annotated per haplotype, organized into 18 phylogenetic families. Gene
274 order and composition were strongly conserved among haplotypes sharing the same S-RNase, but
275 diverged among different S-RNase haplotypes—suggesting a coupling between S-RNase identity and
276 SFBB gene repertoire, as expected in CNSR systems[6,17].

277 The *Malus* S-locus is markedly smaller than its homologs in other CNSR species (e.g., >13 Mb
278 in *Solanum tuberosum*[26] or >3 Mb in *Antirrhinum*[9]), yet it shows signs of substantial local expansion
279 compared to *Gillenia trifoliata*, a Rosaceae species with a 55-kb non-self SI region[38]. The microsynteny
280 detected between an SFBB-like gene from *Gillenia* and a *Malus* SFBB gene, as well as between a
281 nearby transposable element, suggests a shared ancestral origin between the two loci[38]. The *Gillenia*
282 region is non-functional, and its smaller size could reflect progressive genomic degeneration in *Gillenia*
283 and/or local duplication events in *Malus*, followed by functional diversification. Together, these
284 processes likely underlie the evolution of the complex multigenic recognition system observed in
285 *Malus*.
286
287 **Constraints on gene copy number and recognition repertoire**
288 Across CNSR systems, the number of SFBB or SLF genes per haplotype roughly matches the number
289 of distinct gene families: 18 in *Malus*, ~32 in *Antirrhinum*[9], and 18–20 in *Petunia*[13]. This near one-to-
290 one correspondence may reflect an evolutionary constraint whereby each S-haplotype maintains the
291 whole set of anti-toxins, with the exception of the one targeting its own S-RNase. Indeed, theory predicts
292 that maintaining just enough SFBBs to cover all non-self S-RNases of the population (i.e., reaching
293 maximal "completeness") minimizes fitness costs associated with redundancy and maximizes
294 reproductive success[15].
295 In our data, some SFBBs, such as SFBB11, exhibited signs of broader recognition. This
296 suggests selection may favor the evolution of multi-target SFBBs to limit the expansion of the locus,
297 while assuring detoxification of all extant S-alleles. Indeed, in *M. domestica*, more than 30 distinct S-
298 alleles have been reported[39], while the number of SFBB is limited to 18. Such optimization likely
299 reflects trade-offs between specificity, redundancy, and genome size constraints imposed by
300 recombination suppression at the S-locus. It is not clear whether differences in the total number of
301 SFBB/SLF genes between *Malus* (18) and *Antirrhinum* (32) are due to differences in the average degree
302 of promiscuous interactions in toxin recognition, or whether it is due to differences in number of S-
303 alleles maintained at the species level, which is still unknown in *Antirrhinum*.
304
305 **Gene duplication, selection, and exchange**
306 SFBB expansion in *Malus* primarily involved tandem and proximal duplications, in contrast to the
307 dispersed duplication patterns seen elsewhere on chromosome 17. These duplications likely facilitated

308 neofunctionalization. Signals of positive selection—particularly in the substrate-binding FBA
309 domain—suggest adaptive diversification to expand recognition specificity.
310 We also detected evidence of gene conversion and interallelic exchange: high sequence
311 similarity across SFBB families, conserved SFBB–TE pairings, and recurrent TE–SFBB associations
312 across divergent haplotypes. These observations suggest that gene conversion and recombination have
313 helped propagate functional motifs while preserving co-adapted combinations under purifying
314 selection.
315 While TEs likely did not mediate gene conversion directly, their conserved proximity to SFBBs
316 and the dominance of TIR/MITE elements suggest a role in duplicative reshuffling and S-locus
317 evolution.
318
319 **Supergene features and recombination suppression**
320 The *Malus* S-locus bears hallmark features of a supergene: tightly linked co-adapted genes, suppression
321 of recombination, TE accumulation, and signs of reduced purifying selection. Haplotypes sharing the
322 same S-RNase allele showed greater collinearity and structural conservation than those carrying
323 different alleles, consistent with recombination barriers that preserve functional S-RNase–SFBB
324 modules.
325 The buildup of TEs and excess nonsynonymous substitutions suggests reduced selection
326 efficacy due to Hill–Robertson interference[40], a feature common in other supergenes[10,11]. Long-term
327 balancing selection, which preserves diverse S-haplotypes over time, coexists with this degenerative
328 context, highlighting the evolutionary tension between maintaining diversity and the mutational burden.
329
330 **Limits of current interaction models**
331 Using Boltz-1 and MuLAN, we attempted to predict SFBB–S-RNase interactions but failed to
332 distinguish interacting versus non-interacting pairs in *Malus* clearly. In contrast, the same approach
333 successfully recovered validated interactions in *Petunia*[8]. This suggests that SI recognition in *Malus*
334 may involve more complex or subtle molecular interfaces—potentially including conformational
335 dynamics, multimeric assemblies, or regulatory layers (e.g., post-translational modifications or
336 lncRNA-based modulation, as in *Fragaria*)[41].
337 These findings underscore the limitations of current *in silico* models for decoding the molecular
338 logic of the non-self recognition SI system of Maleae. Functional studies—such as expression assays,

CRISPR mutagenesis, or in vitro binding experiments—will be essential for validating SFBB-S-RNase interaction predictions and refining models.

Outlook

Our haplotype-resolved characterization reveals the *Malus* S-locus as a dynamic, multigenic, and supergene-like system shaped by local duplications, gene conversion, TE activity, and strong balancing selection. Beyond offering mechanistic insights into SI maintenance, our results establish *Malus* as a model for investigating how genome architecture, selection, and recombination jointly shape complex recognition systems in plants. Future population-scale and structural variant analyses will clarify how SI evolves and breaks down across wild and cultivated Malus lineages.

Methods

Dataset description

Twenty-seven assembled haplotypes (Supplementary Table 1) from *Malus* species, including both cultivated apple (*M. domestica,* 16 genotypes, comprising 14 dessert varieties and two cider varieties) and wild relatives (11 genotypes from *M. sylvestris*, one *M. sieversii*, and two *M. orientalis*) were examined in this study. Among the individuals used to produce this dataset, 17 were diploids. In most cases, two haplotype assemblies were obtained per individual (Gala and Fuji cultivars, the cider individual, the *M. orientalis* individual, and the four *M. sylvestris* individuals grown at IDEEV). For the Red Delicious, Honeycrisp, Brown Snout, Costard, Bardsey Island, and Newton cultivars, and for *M. sieversii* and *M. sylvestris*, only one haplotype was kept from previous studies due to the unavailability of the second haplotype or insufficient assembly quality. For Golden Delicious and Hanfu, the haplotypes were derived from a double haploid individual, the GDHH13 *M. domestica* reference genome[42], and a tri-haploid individual[43]. This dataset combines 15 already available haplotype assemblies and 12 new sequenced haplotypes from which only chromosome 17 was retained for this study, as this chromosome hosts the SI locus in *Malus*[44] (Fig. 1).

The 27 haplotypes displayed high assembly completeness, with genome sizes ranging from ~600 Mb to 660 Mb, scaffold N50 values of ~9–39 Mb (average N50 = 33.09 Mb ± 6.86), and BUSCO [45] completeness scores generally > 95%. Repetitive content varied moderately between haplotypes (65–76%). Details about the genome assemblies and gene annotations are provided in Supplementary Table 1 and Supplementary Text 1. For convenience, all haplotypes were identified with an ID from h1 to

371 h32. To avoid bias due to heterogeneous annotations, all haplotypes were reannotated using a single,
372 standardized gene annotation pipeline.
373
374 **Construction of an *S-RNase* and *SFBB* gene database**
375 An S-locus gene database, consisting of all *S-RNase* and *SFBB* sequences available in public
376 repositories, was built as a raw material to investigate the genomic architecture of these genes in the
377 genome assemblies described above. Public *S-RNase* DNA sequences[46–49] and *SFBB* DNA sequences
378 [50,51] were collected. The homologous sequences of the *S-RNase* and *SFBB* genes were then recovered
379 using BLASTN searches on the GenBank database with the parameter -e-value 0.001 and added to
380 complete the S-locus gene database. The *S-RNase* database was split between exon 1 and 2 sequences
381 to avoid mis-mapping due to high polymorphism of the intron between individuals. The accession
382 numbers of the genes are provided in Supplementary Tables 2 and 5.
383
384 **S-RNase assignment of each haplotype**
385 Using the database of publicly available *S-RNase* sequences constructed above (Supplementary Table
386 2), the Maloideae *S-RNase* sequences in the database were aligned to *S-RNase* sequences from the
387 haplotypes using Clustal Omega[52] to assign a given *S-RNase* allele to each haplotype (Supplementary
388 Table 3 and Supplementary Fig. 1).
389
390 **Haplotype assembly and gene annotation**
391 Thirty-one haplotype assemblies sourced from publicly available data and newly sequenced genotypes
392 were constructed using PacBio HiFi sequences. Each haplotype was defined as a set of chromosomes
393 transmitted together (Supplementary Table 1 and Supplementary Text 2).
394 Among these, 15 haplotype assemblies were obtained from the literature. Twelve haplotype
395 assemblies were from 10 *M. domestica* cultivars: double haploid Golden Delicious (one haplotype
396 available, GDDH13), Fuji (two haplotypes), Gala (two haplotypes), Red Delicious (one haplotype
397 available), Honeycrisp (one haplotype), tri-haploid Hanfu (one haplotype available), Brown Snout (one
398 haplotype available), Costard, Bardsey Island (one haplotype available), and Newtons (one haplotype
399 available). Additionally, three haplotype assemblies were used, with one from *M. sieversii* and two from
400 *M. sylvestris*.
401 The dataset was enriched with six newly sequenced genomes, representing 12 haplotypes.
402 These new genomes represented one *M. domestica* genotype (Xuanina, used for cider production), one

403 *M. orientalis* genotype from Armenia, and four *M. sylvestris* samples, one each from Austria, Denmark,
404 France, and Romania. Each newly sequenced genome contributes two parental haplotypes, resulting in
405 a total of 12 supplementary haplotypes. Details about DNA extraction, sequencing, and assembly of the
406 seven newly sequenced genomes are summarized in Supplementary Table 1 and Supplementary Text
407 2. Briefly, PacBio sequencing and assembly of the resulting reads generated an average assembly size
408 of 642 Mb, similar to publicly available assemblies (average of 636.5 Mb), with an average scaffold
409 N50 value of 28.12 Mb, which was lower than the average scaffold N50 of publicly available assemblies
410 (average of 37 Mb).
411
412 **Characterization of *SFBB* gene families**
413 To cluster *SFBB* genes from all haplotypes into families, all complete SFBB protein sequences were
414 aligned using Clustal Omega v1.2.4[52]. The alignment was used as input for IQ-tree[53] with ModelFinder[54]
415 for a first run to determine the best-fitting substitution model using 1,000 bootstrap replicates. Using
416 the resulting phylogenetic tree, the hierarchical clustering method of Ward[55] was used with the
417 cophenetic distance matrix, using R[56] and the software packages *ape* v5.7-1[57], *FactoClass* v1.2.8[58], and
418 *stats* v4.3.1[56]. Additionally, OrthoFinder[59] was run on SFBB protein sequence alignments derived from
419 each haplotype. To validate the defined SFBB families, identity percentages were computed from
420 pairwise SFBB alignments (from the same families or different families) using the *pairwiseAlignment*
421 command from the R package *Biostrings* v2.68.1[60].
422 The *Malus* S-locus is located in the peri-telomeric region on the long arm of chromosome 17[44].
423 Therefore, chromosome 17 contigs and annotated genes were extracted using the Helixer/Eggnog
424 pipeline (Supplementary Text 2), followed by analysis of the SI regions to define their size and gene
425 content.
426
427 **Phylogenetic analysis of S-RNases**
428 To determine the haplotypes of the S-alleles, S-RNase protein sequences were aligned to reference
429 sequences listed in Supplementary Table 2 using Clustal Omega v1.2.4[52]. S-RNase sequences
430 associated with S-alleles from previous studies were used to identify S-alleles in the S-haplotype
431 dataset. Specifically, phylogenetic relationships among all S-RNase sequences were examined using
432 IQ-tree[53] with ModelFinder[54] in the first run to determine the best-fitting substitution model using 1,000
433 bootstrap replicates.
434

435 **Sequences and gene synteny within S-loci**

436 To examine the synteny across the S-loci from the 27 *Malus* haplotypes, regions encompassing 500 kb
437 upstream and downstream of S-locus sequences were aligned using the nucmer tool in MUMmer[61].
438 SyRI (Synteny and Rearrangement Identifier) v1.6.3[62] was then used to identify the syntenic path
439 (longest set of colinear regions), structural rearrangements (inversion, translocations, and duplications),
440 local variations (single nucleotide polymorphisms [SNPs], insertion/deletions [InDels], copy-number
441 variation [CNV]) within syntenic blocks and structural rearrangements, and unaligned regions. SyRI
442 takes alignment blocks identified by the initial aligner and identifies larger regions consisting of
443 multiple consecutive one-to-one alignment blocks. Finally, PlotSR[63] was used to visualize synteny
444 using the output from SyRI.

445 To generate gene synteny plots, S-loci annotation gff files from Apollo[64] were converted to bed
446 files using agat_convert_sp_gff2bed.pl from AGAT[65], which were used as input for the R package
447 *gggenomes* v0.9.9.9000[66]. Identity between S-locus genes was computed using Diamond[67] based on
448 their corresponding amino acid (aa) sequences.

449 Syntenic relationships across several S-loci were examined using the network-based approach
450 with the R package Syntenet v1.9.1[21], which treats anchor pairs (duplicates retained from a large-scale
451 duplication event) from synteny comparisons as connected nodes of an undirected unweighted graph[68].

452

453 **Nucleotide diversity analysis with Pixy**

454 Nucleotide diversity (π) across the genome was calculated using Pixy v1.2.6.beta1 software[22], which
455 accurately estimates π from VCF files that include invariant sites and accounts for missing data. π was
456 computed in non-overlapping 10-kb windows using the following parameters: --stats pi --window_size
457 10000 --populations population_file.txt to use the species information for each sample in the dataset.

458 The input VCF file was originally generated in Chen et al., (2025)[69] and includes multiple
459 phased haploid genomes from several *Malus* species. From this dataset, a subset of 41 samples was
460 extracted, representing four species relevant to our study: *M. domestica* (n=10), *M. orientalis* (n=9), *M.*
461 *sieversii* (n=10), and *M. sylvestris* (n=12). The analysis was restricted to chromosome 17, which
462 harbours the S-locus. The coordinates of the S-locus in the GDDH13 reference genome[70], corresponding
463 to haplotype h1 in our study, were defined as 30,032,275 bp and 31,732,190 bp, and windows were
464 classified as either inside or outside the S-locus.

465 To identify outlier windows with significantly higher π than the remaining genomes, the
466 windows with the top 1% highest-π values within each species were defined independently. To

467 determine whether the S-locus was enriched for high-diversity windows, a permutation-based
468 enrichment test was performed using R[56]. The empirical *p*-value was calculated as the proportion of
469 permutations in which the number of outlier windows in the S-locus was equal to or greater than the
470 observed count. A significant *p*-value ($p < 0.05$) indicates that high-diversity windows are non-
471 randomly concentrated in the S-locus, consistent with a signal of balancing selection.
472
473 **Detection of SNP density and non-synonymous/synonymous ratio along chromosome 17**
474 We used the SnpEff[71]-annotated VCF file corresponding to chromosome 17 to investigate the
475 distribution of genetic variation across the S-locus. Single nucleotide polymorphisms (SNPs) were
476 classified according to their predicted functional effects into synonymous or non-synonymous variants.
477 Variants located within SFBB coding regions, where recurrent positive selection is expected, were
478 excluded to avoid upward bias in the nS/S ratio. SNP counts were aggregated in non-overlapping
479 windows of 5 kb along the chromosome, from which we calculated both the density of SNPs and the
480 ratio of non-synonymous to synonymous substitutions (nS/S). To visualize these patterns, we
481 implemented a custom Python script relying on cyvcf2[72], pandas[73], and matplotlib[74]. The script
482 produced a three-panel figure with (i) the nS/S ratio, (ii) the SNP density per window, and (iii) a gene
483 track. Gene coordinates were retrieved from the GFF3 annotation file, and all annotated genes were
484 represented as blocks along the chromosome, with SFBB genes highlighted in a distinct color.
485
486 **Signatures of selection at SI genes**
487 To determine whether the *SFBB* genes evolved neutrally or by natural selection (positive or purifying),
488 the codeml program in the PAML package v4.9[75] was used. Codeml computes the ratio of
489 nonsynonymous (dN) to synonymous (dS) substitutions for various models of sequence evolution. The
490 most likely model explaining the data is chosen based on a likelihood ratio test computed among
491 models. Three pairs of site-specific models allowed us to test for recurrent, diversifying selection (M0
492 and M3, M1a and M2a, and M7 and M8). One SFBB protein sequence alignment for each haplotype
493 was used. To assess whether aa identity at each aligned position was significantly associated with the
494 *SFBB* gene family, a multinomial regression model was fitted for each position that showed at least two
495 different aa and was present in at least two families. For each position, a null model (aa ~ 1) was
496 compared to a full model (aa ~ Family) using a likelihood ratio test. *P*-values were computed from the
497 χ^2 distribution and adjusted for multiple testing using the Benjamini–Hochberg procedure to control the
498 false discovery rate (FDR). Multiple correspondence analysis (MCA), which is specifically designed

499 for categorical data and better captures variation in aa composition across discrete sites, was performed
500 to investigate the clustering of *SFBB* genes based on aa identity at key positions. For each gene, aa
501 residues at conserved positions were extracted and treated as categorical variables. The MCA was
502 conducted using the *FactoMineR* package[76] in R[56] with the SFBB family provided as a supplementary
503 qualitative variable. Individuals (genes) were projected onto the first two dimensions, and family labels
504 were used for colouring.

505 For S-RNases, 27 protein sequences were aligned using Clustal Omega v1.2.4[52]. To identify
506 codon positions likely involved in allele-specific recognition in the S-RNase sequences, evidence from
507 multiple complementary approaches was combined. First, the Fixed Effects Likelihood (FEL) method
508 available on the datamonkey web platform[77] was applied for codon alignment restricted to one
509 representative sequence per S-allele to focus on substitutions that occurred between allelic groups rather
510 than within them. In parallel, the site models implemented in codeml (PAML[78]) were used to detect
511 codon sites evolving under positive selection based on likelihood ratio tests comparing models, allowing
512 for $\omega > 1$ (e.g., M2a, M8) against their respective null models. The results from both methods were
513 compared to retain only robust candidates. To assess whether these positively selected sites were
514 conserved within allelic groups, the full codon alignment was examined, including all available
515 sequences per allele. For each candidate site, intra-allelic variation was quantified by counting the
516 number of distinct codons observed within each group. Positions showing no variation within any allele,
517 i.e., monomorphic within-group but polymorphic between groups, were considered strong candidates
518 for functional divergence related to allele-specific interactions.

519

520 **Search for duplicated genes**

521 To examine how multiple *SFBB* genes were generated and proliferated, the classify_gene_pairs
522 command in the R/Bioconductor package *doubletrouble*[79] was used with the standard scheme (binary
523 = FALSE). In short, intra-haplotypes protein similarity searches were performed using DIAMOND[67]
524 (sensitive mode, e-value = 1e−10, top hits = 5) to identify the entire set of paralogous gene pairs for
525 each haplotype. Paralogous gene pairs in the same syntenic blocks were classified as arising from
526 segmental duplication. A tandem duplication is a segmental duplication that results from an unequal
527 crossing over[80,81]. A few genes separate proximal gene pairs[82] and can originate from ancient tandem
528 duplication events disrupted by the insertion of other genes[83]. Dispersed duplication occurs through
529 unpredictable and random patterns by mechanisms that remain unclear, generating two gene copies that
530 are neither neighboring nor colinear[84].

531

532 **Signatures of gene conversion in *SFBB* genes**

533 Intra-*SFBB* family gene conversion signatures were detected using GENECONV[85], which scans aligned
534 sequences and identifies segments (tracts) that are (1) identical or nearly identical, (2) longer than
535 expected by chance, and (3) shared between sequences that are otherwise divergent. GENECONV tests
536 gene conversion using 10,000 permutations and assesses significant gene alignment using Bonferroni
537 correction as well as the Karlin-Altschul score. To identify potential preferential gene conversion
538 between specific S-allele pairs, a global table of gene conversion events was compiled, with each event
539 associated with the S-alleles of the two haplotypes involved. For each event, the corresponding S-allele
540 pair was annotated. Because S-alleles were unevenly represented across the 27 S-haplotypes, each S-
541 allele was assigned a weight equal to the inverse of its frequency across the set of assemblies. To enable
542 robust statistical testing, a bootstrap procedure was implemented. In each replicate, 10 S-haplotypes
543 were randomly selected, and only gene conversion events between S-alleles present in that subset were
544 retained. The number of events per S-allele pair was then counted and associated with the corresponding
545 mean weight. After repeating this procedure 500 times, a dataset was obtained with multiple
546 observations per pair. A quasi-Poisson regression model using the glm function from the R package
547 *stats*[56] was then used to test whether some S-allele pairs exhibited significantly higher or lower gene
548 conversion frequencies than expected. The model was fitted using the number of conversion events as
549 the response variable, the S-allele pair as a predictor, and the mean weight as a statistical weight to
550 account for allelic representation bias.

551

552 **TE distribution and enrichment analysis around *SFBB* genes**

553 TEs within the S-locus were annotated using a pan-genomic TE library built from a representative set
554 of apple genomes. The TE consensus libraries were first generated using the *TEdenovo* pipeline from
555 REPET v3.0 using Tedenovo[86], and then using these libraries the TEs of the following genomes were
556 annotated using TEannot[87]: the reference cultivar GDDH13[70], one haplotype from a cider variety
557 (unpublished data), one haplotype from each European *Malus sylvestris* population (unpublished data),
558 one haplotype of *M. orientalis* (unpublished data), and one haplotype of *M. sieversii*[88]. These libraries
559 were concatenated, and redundancy was removed using PASTEC[89] with thresholds of at least 98%
560 identity and 95% coverage. Sequences showing high similarity to *SFBB* genes (>90%) or classified as
561 potential host genes (PHGs) by PASTEC were excluded. The resulting curated database was then used

562 to determine shared and non-shared TEs insertions across genomes in S-locus regions using
563 *panREPET*[90].
564 To identify potentially recurrent associations between TEs and *SFBB* gene families
565 independently of the *S-RNase* allele, a permutation test was performed. For each TE consensus–*SFBB*
566 family pair, the number of distinct S-alleles (nS-alleles) observed among the haplotypes where the
567 association occurred was counted. TE–*SFBB* proximity was restricted to ≤ 4 kb as a conservative
568 threshold. Inter-*SFBB* distances within the S-locus are generally orders of magnitude larger (commonly
569 tens of kb; Supplementary Fig. 23), so a 4-kb window targets elements that are genuinely co-located
570 with an *SFBB* gene, encompassing likely regulatory flanks and the range of plausible short
571 recombination/gene-conversion footprints while limiting noise from distant TEs. This number was then
572 compared to a null distribution obtained by randomly permuting the S-alleles across haplotypes. At
573 each iteration, S-alleles were shuffled across haplotypes while preserving the TE–*SFBB* associations.
574 An empirical *p*-value was calculated as the proportion of permutations in which the number of S-alleles
575 was equal to or greater than the observed value. This approach allows us to detect TE–*SFBB*
576 associations that recur across multiple S-alleles more frequently than expected by chance, suggesting
577 possible gene conversion or recombination events within the S-locus. These associations were
578 visualized as heatmaps using the R package *ggplot2*[91].
579
580 **Protein–protein interactions**
581 The sequences from the different families were analysed using MuLAN[33], a sequence-based deep-
582 learning method designed to predict changes in binding affinity induced by mutations affecting protein
583 sequences. In addition, MuLAN can be run on single sequences to compute scores for each residue
584 based on a local attention mechanism, normalized in the range [0, 1], which correlates with interacting
585 or functional regions. Finally, the sequences in each family were aligned. The score profiles at the
586 aligned positions were plotted, highlighting the experimentally determined positive selection sites
587 (Supplementary Fig. 12, Supplementary Fig. 18, and Supplementary Fig. 22). Predicted structures for
588 protein complexes were obtained with Boltz-1[32], using the 1.0.0 version of the package. For each
589 complex, multiple sequence alignments were automatically retrieved using the MMseqs2 server and
590 five alternative structures were generated, setting an initial random seed of 42. For each case, we then
591 selected the predicted structure with the highest associated confidence score. We did not employ
592 additional steering potentials as no steric clashes were observed in the model's outputs. In the
593 comparison of model structures of complexes generated from *Malus* and *Petunia* sequences, we

evaluated structural differences with different confidence measures of the predicted protein–protein interaction: pLDDT (predicted local distance difference test) and i-pLDDT (interface pLDDT), that measure local confidence averaged over residues, and pTM (predicted template modeling score) and i-pTM (interface pTM), that measure overall accuracy of the structure and relative orientation of the subunits.

Data availability

The coding sequences and protein sequences of SFBB and S-RNase genes are available in the ZENODO repository: DOI https://doi.org/10.5281/zenodo.17226708. All analysis files and codes are available at https://github.com/CornilleEclecticLab/Apple-SI/tree/main.

Funding

This research was funded by ANR JCJC PLEASURE ANR-21-CE20-0005 and a Tamkeen research fund under AD454 NYUAD led by AMC.

Authors contributions

AMC obtained funding. AV, WM, XC, AM, and AMC generated, assembled, and anchored the genome sequences. AM, GL, SS, ALF, AC, and AMC analyzed the data. All co-authors discussed the results. AM, AMC, VC, MM, XV, and AC wrote the manuscript with critical input from other co-authors.

Conflicts of interest

The authors declare that they have no financial conflict of interest with the content of this article.

References

1. Charlesworth, D. Balancing Selection and Its Effects on Sequences in Nearby Genome Regions. *PLoS Genet.* **2**, e64 (2006).

2. Glémin, S. & Galtier, N. Genome Evolution in Outcrossing Versus Selfing Versus Asexual Species. in *Evolutionary Genomics* (ed. Anisimova, M.) vol. 855 311–335 (Humana Press, Totowa, NJ, 2012).

3. Wright, S. I., Ness, R. W., Foxe, J. P. & Barrett, S. C. H. Genomic Consequences of Outcrossing and Selfing in Plants. *Int. J. Plant Sci.* **169**, 105–118 (2008).

4. Minamikawa, M. *et al.* Apple S locus region represents a large cluster of related, polymorphic and pollen-specific F-box genes. *Plant Mol. Biol.* **74**, 143–154 (2010).

5. Sassa, H. *et al. S Locus F-Box Brothers* : Multiple and Pollen-Specific F-Box Genes With *S* Haplotype-Specific Polymorphisms in Apple and Japanese Pear. *Genetics* **175**, 1869–1881 (2007).

6. Fujii, S., Kubo, K. & Takayama, S. Non-self- and self-recognition models in plant self-incompatibility. *Nat. Plants* **2**, 16130 (2016).

7. Williams, J. S., Wu, L., Li, S., Sun, P. & Kao, T.-H. Insight into S-RNase-based self-incompatibility in Petunia: recent findings and future directions. *Front. Plant Sci.* **6**, (2015).

8. Kubo, K. *et al.* Collaborative Non-Self Recognition System in S-RNase–Based Self-Incompatibility. *Science* **330**, 796–799 (2010).

9. Zhu, S. *et al.* The Snapdragon Genomes Reveal the Evolutionary Dynamics of the *S* -Locus Supergene. *Mol. Biol. Evol.* **40**, msad080 (2023).

10. Jay, P. *et al.* Supergene Evolution Triggered by the Introgression of a Chromosomal Inversion. *Curr. Biol.* **28**, 1839-1845.e3 (2018).

11. Jay, P., Jeffries, D., Hartmann, F. E., Véber, A. & Giraud, T. Why do sex chromosomes progressively lose recombination? *Trends Genet.* **40**, 564–579 (2024).

12. Kay, T., Helleu, Q. & Keller, L. Iterative evolution of supergene-based social polymorphism in ants. *Philos. Trans. R. Soc. B Biol. Sci.* **377**, 20210196 (2022).

644 13. Kubo, K. *et al.* Gene duplication and genetic exchange drive the evolution of S-RNase-based self-
645 incompatibility in Petunia. *Nat. Plants* **1**, 14005 (2015).

646 14. Liang, M. *et al.* Evolution of self-compatibility by a mutant Sm-RNase in citrus. *Nat. Plants* **6**,
647 131–142 (2020).

648 15. Bod'ová, K., Priklopil, T., Field, D. L., Barton, N. H. & Pickup, M. Evolutionary Pathways for the
649 Generation of New Self-Incompatibility Haplotypes in a Nonself-Recognition System. *Genetics*
650 **209**, 861–883 (2018).

651 16. Harkness, A., Goldberg, E. E. & Brandvain, Y. Diversification or collapse of self-incompatibility
652 haplotypes as outcomes of evolutionary rescue. Preprint at https://doi.org/10.1101/641613 (2019).

653 17. Erez, K., Jangid, A., Feldheim, O. N. & Friedlander, T. The role of promiscuous molecular
654 recognition in the evolution of RNase-based self-incompatibility in plants. *Nat. Commun.* **15**, 4864
655 (2024).

656 18. Vekemans, X. & Slatkin, M. Gene and allelic genealogies at a gametophytic self-incompatibility
657 locus. *Genetics* **137**, 1157–1165 (1994).

658 19. Castric, V., Bechsgaard, J., Schierup, M. H. & Vekemans, X. Repeated Adaptive Introgression at
659 a Gene under Multiallelic Balancing Selection. *PLoS Genet.* **4**, e1000168 (2008).

660 20. Charlesworth, D. Balancing Selection and Its Effects on Sequences in Nearby Genome Regions.
661 *PLoS Genet.* **2**, e64 (2006).

662 21. Almeida-Silva, F., Zhao, T., Ullrich, K. K., Schranz, M. E. & Van De Peer, Y. syntenet: an
663 R/Bioconductor package for the inference and analysis of synteny networks. *Bioinformatics* **39**,
664 (2023).

22. Korunes, K. L. & Samuk, K. PIXY : Unbiased estimation of nucleotide diversity and divergence in the presence of missing data. *Mol. Ecol. Resour.* **21**, 1359–1368 (2021).

23. Nei, M. & Li, W. H. Mathematical model for studying genetic variation in terms of restriction endonucleases. *Proc. Natl. Acad. Sci.* **76**, 5269–5273 (1979).

24. Jay, P., Véber, A. & Giraud, T. Stepwise expansion of recombination suppression on sex chromosomes and other supergenes through lower load advantage and deleterious mutation sheltering. Preprint at https://doi.org/10.1101/2025.06.27.661902 (2025).

25. Yang, Q., Zhang, D., Li, Q., Cheng, Z. & Xue, Y. Heterochromatic and genetic features are consistent with recombination suppression of the self-incompatibility locus in *Antirrhinum*. *Plant J.* **51**, 140–151 (2007).

26. Jing, X. *et al.* Genetic diversity of the self-incompatibility locus in diploid potato. *J. Integr. Agric.* S2095311924004209 (2024) doi:10.1016/j.jia.2024.12.011.

27. Harbord, R. M., Napoli, C. A. & Robbins, T. P. Segregation Distortion of T-DNA Markers Linked to the Self-Incompatibility (S) Locus in Petunia hybrida. *Genetics* **154**, 1323–1333 (2000).

28. Vázquez, N. *et al.* BDBM 1.0: A Desktop Application for Efficient Retrieval and Processing of High-Quality Sequence Data and Application to the Identification of the Putative Coffea S-Locus. *Interdiscip. Sci. Comput. Life Sci.* **11**, 57–67 (2019).

29. Cao, Z.-H. *et al.* An *S* -locus F-box protein as pollen *S* determinant targets non-self S-RNase underlying self-incompatibility in *Citrus*. *J. Exp. Bot.* **75**, 3891–3902 (2024).

30. Gu, C. *et al.* Long-read genome sequencing reveals the sequence characteristics of pear self-incompatibility locus. *Mol. Hortic.* **5**, 13 (2025).

686 31. Chen, L.-Y. *et al.* The bracteatus pineapple genome and domestication of clonally propagated
687 crops. *Nat. Genet.* **51**, 1549–1558 (2019).

688 32. Wohlwend, J. *et al.* Boltz-1 Democratizing Biomolecular Interaction Modeling. Preprint at
689 https://doi.org/10.1101/2024.11.19.624167 (2024).

690 33. Lombardi, G. & Carbone, A. MuLAN: Mutation-driven Light Attention Networks for investigating
691 protein-protein interactions from sequences. Preprint at https://doi.org/10.1101/2024.08.24.609515
692 (2024).

693 34. Jurka, J. *et al.* Repbase Update, a database of eukaryotic repetitive elements. *Cytogenet. Genome*
694 *Res.* **110**, 462–467 (2005).

695 35. Ishimizu, T. *et al.* Identification of regions in which positive selection may operate in S-RNase of
696 Rosaceae: Implication for *S* -allele-specific recognition sites in S-RNase. *FEBS Lett.* **440**, 337–342
697 (1998).

698 36. Ushijima, K. *et al.* Cloning and characterization of cDNAs encoding S-RNases from almond
699 (Prunus dulcis): primary structural features and sequence diversity of the S-RNases in Rosaceae.
700 *Mol. Gen. Genet. MGG* **260**, 261–268 (1998).

701 37. Goldberg, E. E. *et al.* Species Selection Maintains Self-Incompatibility. *Science* **330**, 493–495
702 (2010).

703 38. Wang, R. *et al.* Characterisation of the Gillenia S-locus provides insight into evolution of the
704 nonself-recognition self-incompatibility system in apple. *Sci. Rep.* **15**, 14630 (2025).

705 39. Kim, H.-T. *et al.* Identification and characterization of *S-RNase* genes in apple rootstock and the
706 diversity of *S-RNases* in *Malus* species. *J. Plant Biotechnol.* **43**, 49–57 (2016).

707 40. Branco, S. *et al.* Multiple convergent supergene evolution events in mating-type chromosomes.
708 *Nat. Commun.* **9**, 2000 (2018).

709 41. Du, J. *et al.* Molecular characteristics of *S-RNase* alleles as the determinant of self-incompatibility
710 in the style of *Fragaria viridis*. *Hortic. Res.* **8**, (2021).

711 42. Daccord, N. *et al.* High-quality de novo assembly of the apple genome and methylome dynamics
712 of early fruit development. *Nat. Genet.* **49**, 1099–1106 (2017).

713 43. Qin, S. *et al.* A chromosome-scale genome assembly of Malus domestica, a multi-stress resistant
714 apple variety. *Genomics* **115**, 110627 (2023).

715 44. Aguiar, B. *et al.* Convergent Evolution at the Gametophytic Self-Incompatibility System in Malus
716 and Prunus. *PLOS ONE* **10**, e0126138 (2015).

717 45. Simão, F. A., Waterhouse, R. M., Ioannidis, P., Kriventseva, E. V. & Zdobnov, E. M. BUSCO:
718 assessing genome assembly and annotation completeness with single-copy orthologs.
719 *Bioinformatics* **31**, 3210–3212 (2015).

720 46. Dreesen, R. S. G. *et al.* Analysis of Malus S-RNase gene diversity based on a comparative study of
721 old and modern apple cultivars and European wild apple. *Mol. Breed.* **26**, 693–709 (2010).

722 47. Larsen, B., Ørgaard, M., Toldam-Andersen, T. B. & Pedersen, C. A high-throughput method for
723 genotyping S-RNase alleles in apple. *Mol. Breed.* **36**, 24 (2016).

724 48. Ma, X., Cai, Z., Liu, W., Ge, S. & Tang, L. Identification, genealogical structure and population
725 genetics of S-alleles in Malus sieversii, the wild ancestor of domesticated apple. *Heredity* **119**, 185–
726 196 (2017).

727 49. Vieira, J., Ferreira, P. G., Aguiar, B., Fonseca, N. A. & Vieira, C. P. Evolutionary patterns at the
728 RNase based gametophytic self - incompatibility system in two divergent Rosaceae groups
729 (Maloideae and Prunus). *BMC Evol. Biol.* **10**, 200 (2010).

730 50. Minamikawa, M. *et al.* Apple S locus region represents a large cluster of related, polymorphic and
731 pollen-specific F-box genes. *Plant Mol. Biol.* **74**, 143–154 (2010).

732 51. Okada, K., Moriya, S., Haji, T. & Abe, K. Isolation and characterization of multiple F-box genes
733 linked to the S 9 - and S 10 -RNase in apple (Malus × domestica Borkh.). *Plant Reprod.* **26**, 101–
734 111 (2013).

735 52. Sievers, F. & Higgins, D. G. Clustal Omega. *Curr. Protoc. Bioinforma.* **48**, (2014).

736 53. Minh, B. Q. *et al.* Corrigendum to: IQ-TREE 2: New Models and Efficient Methods for
737 Phylogenetic Inference in the Genomic Era. *Mol. Biol. Evol.* **37**, 2461–2461 (2020).

738 54. Kalyaanamoorthy, S., Minh, B. Q., Wong, T. K. F., Von Haeseler, A. & Jermiin, L. S. ModelFinder:
739 fast model selection for accurate phylogenetic estimates. *Nat. Methods* **14**, 587–589 (2017).

740 55. Ward, J. H. Hierarchical Grouping to Optimize an Objective Function. *J. Am. Stat. Assoc.* **58**, 236–
741 244 (1963).

742 56. R Core Team. R: A Language and Environment for Statistical Computing. *R Foundation for*
743 *Statistical Computing* (2021).

744 57. Paradis, E. & Schliep, K. ape 5.0: an environment for modern phylogenetics and evolutionary
745 analyses in R. *Bioinformatics* **35**, 526–528 (2019).

58. Campo Elias Pardo *et al.* FactoClass: Combination of Factorial Methods and Cluster Analysis. The R Foundation https://doi.org/10.32614/cran.package.factoclass (2008).

59. Emms, D. M. & Kelly, S. OrthoFinder: phylogenetic orthology inference for comparative genomics. *Genome Biol.* **20**, 238 (2019).

60. H. Pagès, P. A. Biostrings. Bioconductor https://doi.org/10.18129/B9.BIOC.BIOSTRINGS (2017).

61. Marçais, G. *et al.* MUMmer4: A fast and versatile genome alignment system. *PLOS Comput. Biol.* **14**, e1005944 (2018).

62. Goel, M., Sun, H., Jiao, W.-B. & Schneeberger, K. SyRI: finding genomic rearrangements and local sequence differences from whole-genome assemblies. *Genome Biol.* **20**, 277 (2019).

63. Goel, M. & Schneeberger, K. plotsr: visualizing structural similarities and rearrangements between multiple genomes. *Bioinformatics* **38**, 2922–2926 (2022).

64. Dunn, N. A. *et al.* Apollo: Democratizing genome annotation. *PLOS Comput. Biol.* **15**, e1006790 (2019).

65. Jacques Dainat *et al.* NBISweden/AGAT: AGAT v1.5.0. Zenodo https://doi.org/10.5281/ZENODO.3552717 (2025).

66. Hackl, T., Ankenbrand, M., van Adrichem, B., Wilkins, D. & Haslinger, K. gggenomes: effective and versatile visualizations for comparative genomics. Preprint at https://doi.org/10.48550/ARXIV.2411.13556 (2024).

67. Buchfink, B., Xie, C. & Huson, D. H. Fast and sensitive protein alignment using DIAMOND. *Nat. Methods* **12**, 59–60 (2015).

766 68. Zhao, T. & Schranz, M. E. Network approaches for plant phylogenomic synteny analysis. *Curr.*
767 *Opin. Plant Biol.* **36**, 129–134 (2017).

768 69. Chen, X. *et al.* Gene flow from the European wild apple and selection shaped the domesticated
769 apple (*Malus domestica* Borkh.) genome. Preprint at https://doi.org/10.1101/2025.09.18.676739
770 (2025).

771 70. Daccord, N. *et al.* High-quality de novo assembly of the apple genome and methylome dynamics
772 of early fruit development. *Nat. Genet.* **49**, 1099–1106 (2017).

773 71. Cingolani, P. *et al.* A program for annotating and predicting the effects of single nucleotide
774 polymorphisms, SnpEff: SNPs in the genome of Drosophila melanogaster strain w^{1118} ; iso-2; iso-
775 3. *Fly (Austin)* **6**, 80–92 (2012).

776 72. Pedersen, B. S. & Quinlan, A. R. cyvcf2: fast, flexible variant analysis with Python. *Bioinformatics*
777 **33**, 1867–1869 (2017).

778 73. McKinney, W. Data Structures for Statistical Computing in Python. in 56–61 (Austin, Texas,
779 2010). doi:10.25080/Majora-92bf1922-00a.

780 74. Hunter, J. D. Matplotlib: A 2D Graphics Environment. *Comput. Sci. Eng.* **9**, 90–95 (2007).

781 75. Yang, Z. PAML 4: Phylogenetic Analysis by Maximum Likelihood. *Mol. Biol. Evol.* **24**, 1586–
782 1591 (2007).

783 76. Lê, S., Josse, J. & Husson, F. **FactoMineR** : An *R* Package for Multivariate Analysis. *J. Stat. Softw.*
784 **25**, (2008).

785 77. Weaver, S. *et al.* Datamonkey 2.0: A Modern Web Application for Characterizing Selective and
786 Other Evolutionary Processes. *Mol. Biol. Evol.* **35**, 773–777 (2018).

787 78. Yang, Z. PAML 4: Phylogenetic Analysis by Maximum Likelihood. *Mol. Biol. Evol.* **24**, 1586–
788 1591 (2007).

789 79. Almeida-Silva, F. & Van De Peer, Y. *doubletrouble:*an R/Bioconductor package for the
790 identification, classification, and analysis of gene and genome duplications. Preprint at
791 https://doi.org/10.1101/2024.02.27.582236 (2024).

792 80. Freeling, M. Bias in Plant Gene Content Following Different Sorts of Duplication: Tandem, Whole-
793 Genome, Segmental, or by Transposition. *Annu. Rev. Plant Biol.* **60**, 433–453 (2009).

794 81. Hahn, M. W. Distinguishing Among Evolutionary Models for the Maintenance of Gene Duplicates.
795 *J. Hered.* **100**, 605–617 (2009).

796 82. Wang, Y., Wang, X. & Paterson, A. H. Genome and gene duplications and gene expression
797 divergence: a view from plants. *Ann. N. Y. Acad. Sci.* **1256**, 1–14 (2012).

798 83. Freeling, M. *et al.* Many or most genes in *Arabidopsis* transposed after the origin of the order
799 Brassicales. *Genome Res.* **18**, 1924–1937 (2008).

800 84. Wang, Y., Ficklin, S. P., Wang, X., Feltus, F. A. & Paterson, A. H. Large-Scale Gene Relocations
801 following an Ancient Genome Triplication Associated with the Diversification of Core Eudicots.
802 *PLOS ONE* **11**, e0155637 (2016).

803 85. Sawyer, S. Statistical tests for detecting gene conversion. *Mol. Biol. Evol.*
804 https://doi.org/10.1093/oxfordjournals.molbev.a040567 (1989)
805 doi:10.1093/oxfordjournals.molbev.a040567.

806 86. Flutre, T., Duprat, E., Feuillet, C. & Quesneville, H. Considering Transposable Element
807 Diversification in De Novo Annotation Approaches. *PLoS ONE* **6**, e16526 (2011).

808 87. Quesneville, H. *et al.* Combined Evidence Annotation of Transposable Elements in Genome
809 Sequences. *PLoS Comput. Biol.* **1**, e22 (2005).

810 88. Sun, X. *et al.* Phased diploid genome assemblies and pan-genomes provide insights into the genetic
811 history of apple domestication. *Nat. Genet.* **52**, 1423–1432 (2020).

812 89. Hoede, C. *et al.* PASTEC: An Automatic Transposable Element Classification Tool. *PLoS ONE* **9**,
813 e91929 (2014).

814 90. Saidi, S., Blaison, M., Rodríguez-Ordóñez, M. D. P., Confais, J. & Quesneville, H. panREPET: a
815 reference-free pipeline for detecting shared Transposable Elements from pan-genomes to retrace
816 their dynamics in a species. Preprint at https://doi.org/10.1101/2024.06.17.598857 (2024).

817 91. Wickham, H. ggplot2. *WIREs Comput. Stat.* **3**, 180–185 (2011).

818

Supplementary Table 1: *Malus* assemblies used in this study

Haplo type	Species	Cultivar / Origin	Ploidy	Sequence length	Scaffold N50 (Mb)	Gene count	Protein coding genes (%)	Repeats (%)	Busco (%)	Chromosome 17 length (Mb)	References	Rq
h1	*M. domestica*	cult. Golden delicious	Doubled-haploid	656,833,032	37.632	49,762	51.6	65.4	96.9	34.749	Daccord *et al*., 2017	Kept for subsequent analysis
h2	*M. domestica*	cult. Gala	Diploid	657,696,253	37.966	51,889	93.6	74.85	95.7	32.702	Sun *et al*., 2020	Kept for subsequent analysis
h3	*M. domestica*	cult. Gala	Diploid	577,209,808	36.439	45,344	93.3	74.79	86.6	30.262	Sun *et al*., 2020	Kept for subsequent analysis
h4	*M. domestica*	RGTH1	Haploid	754,684,250	35.935				96.7		Tian *et al.,* 2022	Not kept for subsequent analysis ()
h6	*M. domestica*	cult. Fuji	Diploid	648,363,766	36.861	56,85	94.1	73.75	97.7	34.006	Li *et al*., 2024	Kept for subsequent analysis
h7	*M. domestica*	cult. Fuji	Diploid	647,946,317	37.293	52,523	93.8	74.15	97.6	34.212	Li *et al*., 2024	Kept for subsequent analysis
h8	*M. domestica*	cult. Red delicious	Diploid	625,992,033	37.632	49,554	93.4	74.16	97.4	33.496	Han *et al*., 2017	Kept for subsequent analysis
h9	*M. domestica*	cult. Honeycrisp	Diploid		31.600				1.9		Khan et al., 2022	Not kept for subsequent analysis
h10	*M. domestica*	cult. Honeycrisp	Diploid	648,227,795	32.8	51,523	93.6	74.6	97.6	33.450	Khan et al., 2022	Kept for subsequent analysis
h11	*M. domestica*	cult. Hanfu	Tri-haploid	652,502,298	37.139	51,127	93.6	75.26	97.6	33.999	Qin *et al*., 2023	Kept for subsequent analysis
h12	*M. domestica*	cult. Brown Snout	Diploid	645,430,038	37.911	50,416	93.6	75.08	97.7	34.188	Konyves *et al*., 2022	Kept for subsequent analysis
h13	*M. domestica*	cult. Costard	Diploid	645,735,903	37.048	50,379	64.1	75.23	97.6	33.906	Konyves *et al*., 2022	Kept for subsequent analysis
h14	*M. domestica*	cult. Bardsey Island	Diploid	650,288,218	37.701	50,343	93.8	75.28	97.7	34.850	Konyves *et al*., 2022	Kept for subsequent analysis
h15	*M. domestica*	cult. Newtons	Diploid	638,366,891	37.767	50,265	93.8	74.71	97.7	34.042	Konyves *et al*., 2022	Kept for subsequent analysis
h16	*M. sieversii*	Central Asia	Diploid		36.622				0.7		Sun *et al*., 2020	Not kept for subsequent analysis
h17	*M. sieversii*	Central Asia	Diploid	612,178,858	39.79	46,367	93.6	75.96	91.5	32.620	Sun *et al*., 2020	Kept for subsequent analysis

h18	*M. sylvestris*	Germany	Diploid		35.560				0.8		Sun *et al*., 2020	Not kept for subsequent analysis
h19	*M. sylvestris*	Germany	Diploid	601,478,285	35.227	49,446	56.8	74.02	92.7	31.469	Sun *et al*., 2020	Kept for subsequent analysis
h20	*M. sylvestris*	England	Diploid	639,737,487	36.902	50,379	93.8	74.94	97.7	33.873	Ruhsam *et al*., 2022	Kept for subsequent analysis
h21	*M. domestica*	cult. Xuanina	Diploid	644,465,789	29.167	50,762	57.0	74.57	97.1	33.655	This study	Kept for subsequent analysis
h22	*M. domestica*	cult. Xuanina	Diploid	625,304,225	9.418	48,696	93.7	74.6	95.8	32.333	This study	Kept for subsequent analysis
h23	*M. sylvestris*	Austria	Diploid	644,132,839	24.315	54,796	93.9	73.79	97.6	35.410	This study	Kept for subsequent analysis
h24	*M. sylvestris*	Austria	Diploid	633,775,122	18.97	50,424	93.7	74.11	97.3	33.610	This study	Kept for subsequent analysis
h25	*M. sylvestris*	Denmark	Diploid	638,694,078	24.423	54,188	93.9	74.06	97	34.908	This study	Kept for subsequent analysis
h26	*M. sylvestris*	Denmark	Diploid	633,317,074	30.454	50,573	93.8	74.25	97.1	32.936	This study	Kept for subsequent analysis
h27	*M. sylvestris*	France	Diploid	651,453,350	35.932	51,039	93.8	74.19	97.5	35.550	This study	Kept for subsequent analysis
h28	*M. sylvestris*	France	Diploid	634,091,149	33.34	49,538	93.7	73.75	97.4	32.920	This study	Kept for subsequent analysis
h29	*M. sylvestris*	Romania	Diploid	649,942,226	35.638	51,404	93.8	73.83	97.8	34.218	This study	Kept for subsequent analysis
h30	*M. sylvestris*	Romania	Diploid	643,103,033	30.517	50,104	93.7	74.04	97.8	35.246	This study	Kept for subsequent analysis
h31	*M. orientalis*	Armenia	Diploid	653,674,533	32.637	55,781	93.6	74.32	97.7	35.488	This study	Kept for subsequent analysis
h32	*M. orientalis*	Armenia	Diploid	652,365,126	32.639	51,253	93.8	74.8	98	33.672	This study	Kept for subsequent analysis

Supplementary Table 2: S-RNase database, public accessions from *Malus* and *Pyrus* genus

Accession	S allele	Species	Reference
ACS94938.4	EjS6	*Eriobotrya japonica*	Niska et al., 2010
AB002139.1	PpS1	*Pyrus pyrifolia*	Ishimizu et al., 1998 https://www.ncbi.nlm.nih.gov/pubmed/9700066
AB002140.1	PpS3	*Pyrus pyrifolia*	Ishimizu et al., 1998 https://www.ncbi.nlm.nih.gov/pubmed/9700066
AB002141.1	PpS5	*Pyrus pyrifolia*	Ishimizu et al., 1998 https://www.ncbi.nlm.nih.gov/pubmed/9700066
AB002142.1	PpS6	*Pyrus pyrifolia*	Ishimizu et al., 1998 https://www.ncbi.nlm.nih.gov/pubmed/9700066
AB002143.1	PpS7	*Pyrus pyrifolia*	Ishimizu et al., 1998 https://www.ncbi.nlm.nih.gov/pubmed/9700066
AB019184.1	MdSg	*Malus domestica*	Kitahara et al., 1999
AB032246.1	MdSd	*Malus domestica*	Kitahara et al., 2000
AB032247.1	MdSh	*Malus domestica*	Kitahara et al., 2000
AB035273.1	MdSe	*Malus domestica*	Matsumoto & Kitahara, 2000
AB035928.1	MtSt	*Malus transitoria*	Matsumoto et al., 2000
AB052683.1	MdSi	*Malus domestica*	Kitahara & Matsumoto, 2002
AB062100.1	MdSz	*Malus domestica*	Kitahara & Matsumoto, 2002
AB096138.1	MtSg	*Malus transitoria*	Matsumoto et al., 2000
AB104908.1	PpS8	*Pyrus pyrifolia*	Castillo et al., 2001
AB104909.1	PpS9	*Pyrus pyrifolia*	Castillo et al., 2002
AB236424.2	PcSq	*Pyrus communis*	Takasaki et al., 2006 https://www.ncbi.nlm.nih.gov/pubmed/16565843
AB236425.1	PcS1	*Pyrus communis*	Takasaki et al., 2006 https://www.ncbi.nlm.nih.gov/pubmed/16565843
AB236426.2	PcSr	*Pyrus communis*	Takasaki et al., 2006 https://www.ncbi.nlm.nih.gov/pubmed/16565843
AB236427.1	PcSd	*Pyrus communis*	Takasaki et al., 2006 https://www.ncbi.nlm.nih.gov/pubmed/16565843
AB236428.1	PcSe	*Pyrus communis*	Takasaki et al., 2006 https://www.ncbi.nlm.nih.gov/pubmed/16565843
AB236429.1	PcSb	*Pyrus communis*	Takasaki et al., 2006 https://www.ncbi.nlm.nih.gov/pubmed/16565843
AB236430.1	PcSa	*Pyrus communis*	Takasaki et al., 2006 https://www.ncbi.nlm.nih.gov/pubmed/16565843
AB236431.1	PcSa	*Pyrus communis*	Takasaki et al., 2006 https://www.ncbi.nlm.nih.gov/pubmed/16565843
AB236432.1	PcSk	*Pyrus communis*	Takasaki et al., 2006 https://www.ncbi.nlm.nih.gov/pubmed/16565843
AB258359.1	PcSc	*Pyrus communis*	Moriya et al., unpublished
AB258360.1	PcSg	*Pyrus communis*	Moriya et al., unpublished
AB258361.1	PcSi	*Pyrus communis*	Moriya et al., unpublished
AB258362.1	PcSm	*Pyrus communis*	Moriya et al., unpublished
AB258363.1	PcSn	*Pyrus communis*	Moriya et al., unpublished
AB258364.1	PcSp	*Pyrus communis*	Moriya et al., unpublished
AB258365.1	PcSs	*Pyrus communis*	Moriya et al., unpublished
AB258366.1	PcSt	*Pyrus communis*	Moriya et al., unpublished
AB284262.1	PpSk	*Pyrus pyrifolia*	Kim et al., 2007
AB426604.1	PpS12	*Pyrus pyrifolia*	Okada et al., unpublished
AB426606.1	PpSk	*Pyrus pyrifolia*	Okada et al., unpublished
AB540121.1	MsS33	*Malus sieversii*	Matsumoto et al., 2010
AB540122.1	MdS34	*Malus domestica*	Matsumoto et al., 2010
AB731592.1	PcS25	*Pyrus communis*	Takasaki-Yasuda et al., unpublished
AB779646.1	PcS0	*Pyrus communis*	Takasaki-Yasuda et al., unpublished
AB779647.1	PcS00	*Pyrus communis*	Takasaki-Yasuda et al., unpublished
AF016918.1	MdS26	*Malus domestica*	Verdoodt et al., unpublished
AF016919.1	MdS27	*Malus domestica*	Verdoodt et al., unpublished
AF016920.1	MdS24	*Malus domestica*	Verdoodt et al., unpublished

AF327221.1	MdS10	*Malus domestica*	Van Nerum et al. unpublished
AF327222.1	MdS27b	*Malus domestica*	Van Nerum et al. unpublished
AF327223.1	MdS4	*Malus domestica*	Van Nerum et al. unpublished
AY249428.2	PpS13	*Pyrus pyrifolia*	Tan et al., unpublished
AY250989.3	PbS21	*Pyrus bretschneideri*	Tan et al., unpublished
D49527.1	PpS0000	*Pyrus pyrifolia*	Norioka et al., 1995
D49528.1	PpS000	*Pyrus pyrifolia*	Norioka et al., 1995
D50836.1	MdSc	*Malus domestica*	Sassa et al., 1996
D50837.1	MdSf	*Malus domestica*	Sassa et al., 1996
D88282.1	PsS5	*Pyrus serotina*	Sassa et Hirano., 1997
DQ135990.1	MdS31	*Malus domestica*	Kim et al., unpublished
DQ135991.1	MdS32	*Malus domestica*	Kim et al., unpublished
DQ224344.1	PbS35	*Pyrus bretschneideri*	Yang & Tan, unpublished
DQ414812.1	PbS13	*Pyrus bretschneideri*	Tan et al., unpublished
DQ414813.1	PbS34	*Pyrus bretschneideri*	Tan et al., unpublished
DQ494532.1	PbS21	*Pyrus bretschneideri*	Zhang et al., 2006
DQ494676.1	PbS34	*Pyrus bretschneideri*	Zhang et al., 2006
DQ839240.1	PuS35	*Pyrus ussuriensis*	Wuyun et al., unpublished
DQ991388.1	PbS16	*Pyrus bretschneideri*	Tan et al., unpublished
DQ995285.1	PbS39	*Pyrus bretschneideri*	Tan et al., unpublished
EF566872.1	PsiS28	*Pyrus sinkiangensis*	Zhang et al., unpublished
EF643630.1	PpS15	*Pyrus pyrifolia*	Zhang et al., unpublished
EF643631.2	PbS38	*Pyrus bretschneideri*	Tan et al., unpublished
EF643635.1	PbS16	*Pyrus bretschneideri*	Tan et al., unpublished
EF643636.1	PbS18	*Pyrus bretschneideri*	Tan et al., unpublished
EF643638.1	PbS19	*Pyrus bretschneideri*	Tan et al., unpublished
EF643639.1	PsiS22	*Pyrus sinkiangensis*	Tan et al., unpublished
EF643640.1	PbS27	*Pyrus bretschneideri*	Tan et al., unpublished
EF643641.1	PuS30	*Pyrus ussuriensis*	Tan et al., unpublished
EF689006.1	PuS42	*Pyrus ussuriensis*	Tan et al., unpublished
EF689007.1	PbS42	*Pyrus bretschneideri*	Tan et al., unpublished
EF689008.1	PbS22	*Pyrus bretschneideri*	Tan et al., unpublished
EU081888.1	PbS26	*Pyrus bretschneideri*	Tan et al., unpublished
EU081889.1	PbS12	*Pyrus bretschneideri*	Tan et al., unpublished
EU101462.1	PbS29	*Pyrus bretschneideri*	Tan et al., unpublished
EU101463.1	PbS26	*Pyrus bretschneideri*	Tan et al., unpublished
EU101464.1	PuS40	*Pyrus ussuriensis*	Tan et al., unpublished
EU101465.1	PpS5a	*Pyrus pyrifolia*	Tan et al., unpublished
EU101466.1	PbS17	*Pyrus bretschneideri*	Tan et al., unpublished
EU117115.1	PpS12	*Pyrus pyrifolia*	Tan et al., unpublished
EU336979.1	PuS32	*Pyrus ussuriensis*	Tan et al., unpublished
EU336980.1	PbS39	*Pyrus bretschneideri*	Tan et al., unpublished
EU360894.1	PbS20	*Pyrus bretschneideri*	Tan et al., unpublished
EU375364.1	PbS28	*Pyrus bretschneideri*	Tan et al., unpublished
EU477839.1	PcS21	*Pyrus communis*	Sanzol, https://www.ncbi.nlm.nih.gov/pubmed/19096853
EU477840.1	PcS21	*Pyrus communis*	Sanzol, https://www.ncbi.nlm.nih.gov/pubmed/19096853
FJ943264.1	MspecS1	*Malus spectabilis*	Zhang et al., unpublished
FJ943266.1	MspecS2	*Malus spectabilis*	Zhang et al., unpublished
FJ943268.1	MspecS3	*Malus spectabilis*	Zhang et al., unpublished

FJ943270.1	MspecS4	*Malus spectabilis*	Zhang et al., unpublished
FJ943272.1	MspecS5	*Malus spectabilis*	Zhang et al., unpublished
FJ946628.1	PpS46	*Pyrus pyrifolia*	Tan et al., unpublished
GQ180466.1	PcS4	*Pyrus communis*	Sanzol, https://www.ncbi.nlm.nih.gov/pubmed/20701704
KF468727.1	MsiS1	*Malus sikkimensis*	Gu, unpublished
KF468730.1	MsiS7	*Malus sikkimensis*	Gu, unpublished
KF588567.1	PcS126	*Pyrus communis*	Nikzad Gharehaghaji et al., unpublished
U12199.1	MdS2	*Malus domestica*	Broothaerts et al., 1995
U12200.1	MdS3	*Malus domestica*	Broothaerts et al., 1995
U19793.1	MdS9	*Malus domestica*	Broothaerts et al., 1995

Supplementary Table 3: S-loci coordinates, predicted SFBB number and S-alleles in studied haplotypes

Haplotype	Species	Cultivar/ origin	S-loci start on chr17	S-loci end on chr17	S-loci length	Predicted S-loci gene number	Predicted SFBBs number (complete sequences)	S-Rnase ID	Predicted S-RNase allele
h14	*M. domestica*	Bardsey Island	30701244	32097319	1396076	39	17	h14_chr17_3.1	MdS2
h12	*M. domestica*	Brown snout	29604507	31323943	1719437	43	18	h12_chr17_001110.1	MspecS4
h13	*M. domestica*	Costard	29699373	31095434	1396062	38	17	h13_chr17_3.1	MdS2
h7	*M. domestica*	Fuji	30197526	31518020	1320495	40	17	h7_chr17_6.1	MdS9
h6	*M. domestica*	Fuji	29893470	31195680	1302211	48	17	h6_chr17_001448.1	MdSf
h3	*M. domestica*	Gala	26135286	27539957	1404672	51	17	h3_chr17_3.1	MdS2
h2	*M. domestica*	Gala	28665960	29985017	1319058	49	17	h2_chr17_001456.1	MdS5
h1	*M. domestica*	Golden delicious double haploid (GDDH13)	30032275	31732190	1699916	33	16	h1_chr17_001308.1	MdS3
h11	*M. domestica*	Hanfu	29830584	31150956	1320373	42	18	h11_chr17_8.1	MdS9
h10	*M. domestica*	Honeycrisp	29310889	30706999	1396111	39	17	h10_chr17_4.1	MdS2
h15	*M. domestica*	Newtons	29920233	31222329	1302097	43	18	h15_chr17_001441.1	MdSf
h8	*M. domestica*	Red delicious	29883495	30810778	927284	48	17	h8_chr17_3.1	MdSe
h21	*M. domestica*	Xuanina	29544619	30982290	1437672	42	18	h21_chr17_001396.1	MdS26
h22	*M. domestica*	Xuanina	28259688	29525297	1265610	40	18	h22_chr17_001349.1	MdS4
h32	*M. orientalis*	Armenia	29847786	30941904	1094119	36	19	h32_chr17_001379.1	MdS9
h31	*M. orientalis*	Armenia	31699461	32754781	1055321	45	19	h31_chr17_5.1	NewC
h17	*M. sieversii*	Kazakstan	28636332	29834722	1198391	36	17	h17_chr17_3.1	PbS13
h20	*M. sylvestris*		30157545	31217444	1059900	37	16	h20_chr17_001396.1	MdS4
h19	*M. sylvestris*		27161358	28640677	1479320	39	20	h19_chr17_4.1	PpS1
h23	*M. sylvestris*	Austria	30930378	32432552	1502175	47	16	h23_chr17_2.1	MdS2
h24	*M. sylvestris*	Austria	29911385	30929757	1018373	40	14	h24_chr17_001105.1	NewA
h26	*M. sylvestris*	Denmark	29352325	30455556	1103232	38	17	h26_chr17_001363.1	MdS5
h25	*M. sylvestris*	Denmark	30768546	32202276	1433731	42	18	h25_chr17_2.1	NewD
h28	*M. sylvestris*	France	28763989	30262854	1498866	37	17	h28_chr17_001351.1	PbS42
h27	*M. sylvestris*	France	31333056	32800349	1467294	41	19	h27_chr17_3.1	MdSe
h29	*M. sylvestris*	Romania	29817762	31260259	1442498	49	19	h29_chr17_4.1	NewE
h30	*M. sylvestris*	Romania	30593311	32469098	1875788	47	17	h30_chr17_2.1	MspecS1

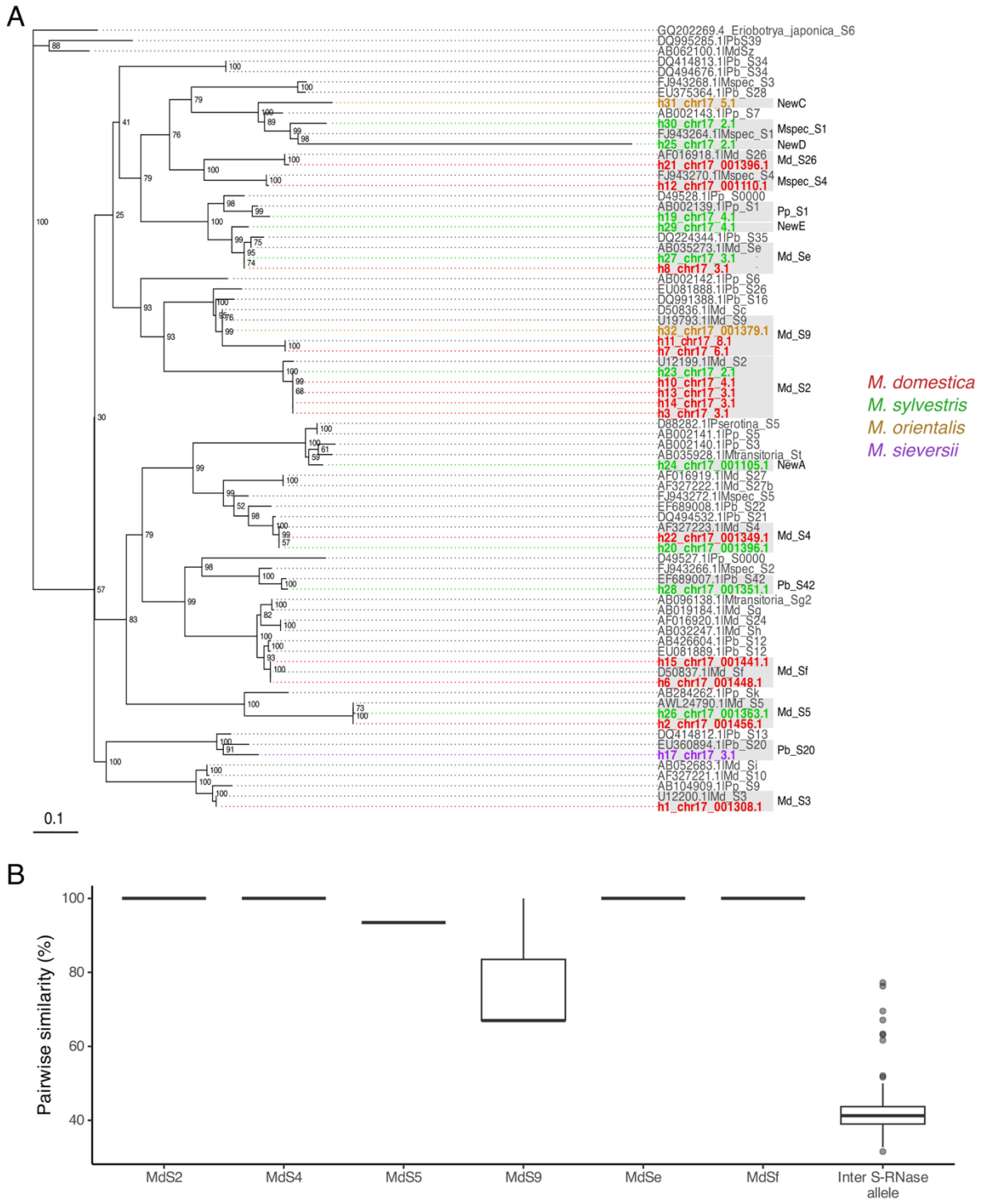

Supplementary Fig. 1: Phylogeny and similarity patterns of Malus S-RNases. (A) Maximum-likelihood phylogeny of S-RNase protein sequences including both annotated haplotype sequences from the present dataset and publicly available S-RNases. Species of origin are indicated: *Md* = *Malus domestica*; *Mspec* = *M. spectabilis*; *Msiev* = *M. sieversii*; *Pb* = *Pyrus breitschneideri*; *Pc* = *P. communis*; *Pp* = *P. pyrifolia*; *Pu* = *P. ussuriensis*. (B) Distribution of pairwise protein sequence similarities among S-RNases, computed in R based on amino acid identity (1 – distance). Boxplots show similarity values for S-RNases belonging to the same S-allele (intra-allelic comparisons) versus those belonging to different alleles (inter-allelic comparisons).

Supplementary Table 4: Expected and observed S-RNase alleles in *M. domestica* S-haplotypes from our dataset

Cultivar	**Expected S allele (references)**	**Observed S alleles**
Golden delicious	MdS2/MdS3 (Schneider et al., 2001 ; Ryan et al., 2020)	h1 (MdS3)
Fuji	MdS1/MdS9 (Kasajima et al., 2017 ; Ryan et al., 2020) or MdSf (Matsumoto et al., 1999a) or MdSc/MdSf (Sassa et al., 1994)	h6 (MdSf) / h7 (MdS9)
Honeycrisp	MdS2/MdS24 (Ryan et al., 2020)	h10 (MdS2)
Gala	MdS2/MdS5 (Matsumoto et al., 1999b) or MdS3/MdS5 (Ryan et al., 2020)	h2 (?) / h3 (MdS2)
Red delicious	MdS9/MdS28 (Ryan et al., 2020) MdSe = MdS28 (Kasajima et al., 2017)	h8 (?)
Newtons	Unknown	h15 (MdSf)
Brown snout	Unknown	h12 (MspecS4)
Hanfu	Unknown	h11 (MdS9)
Costard	Unknown	h13 (MdS3)
Bardsey Island	Unknown	h14 (MdS3)

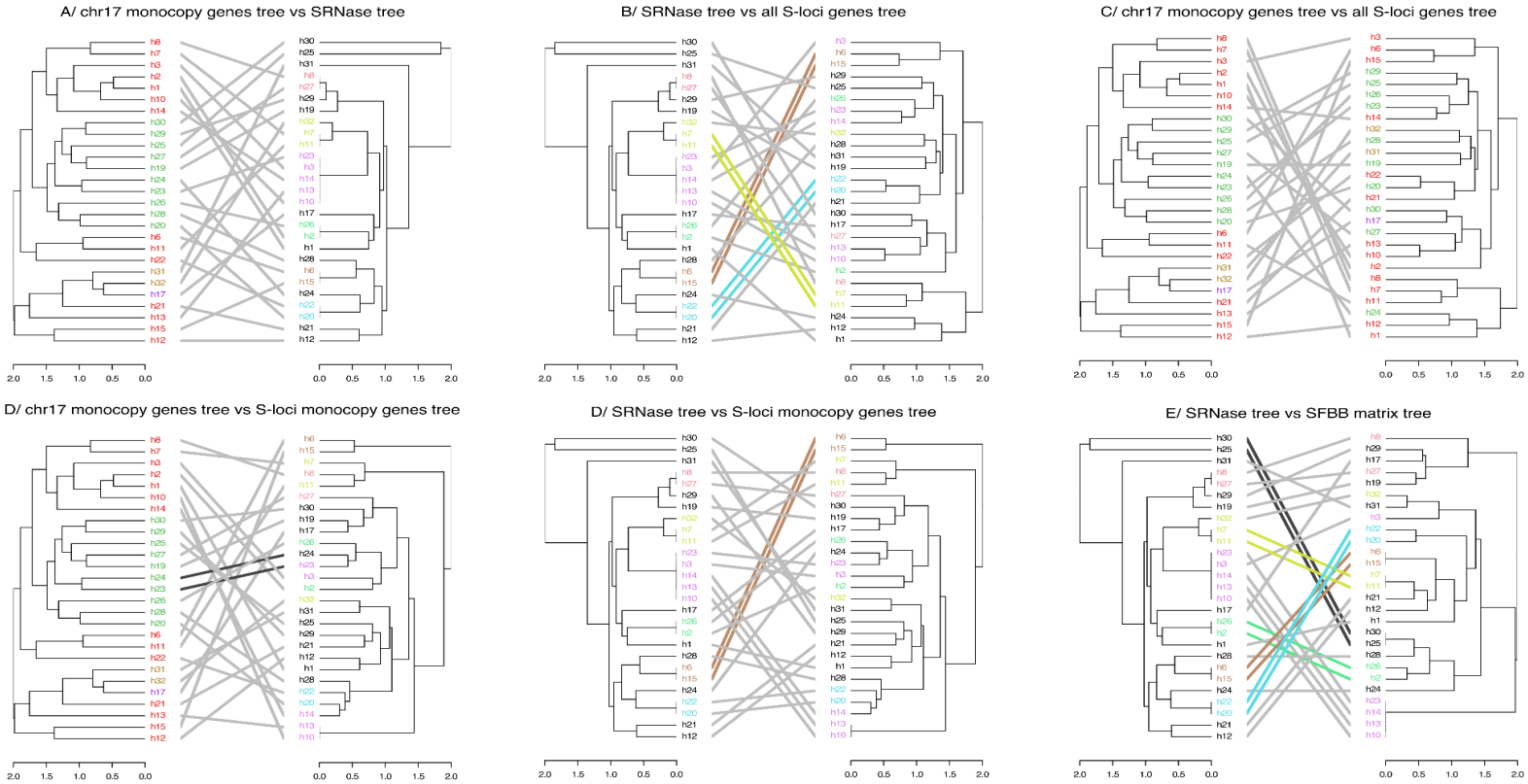

Supplementary Fig. 2: Tanglegram comparisons of phylogenetic trees related to S-locus components in apple trees. Tanglegrams illustrate topological comparisons between hierarchical clustering trees derived from different genomic features: **(A)** Species tree vs. *S-RNase* gene tree ; **(B)** *S-RNase* gene tree vs. tree based on all S-locus genes (including mono- and multi-copy genes) ; **(C)** Species tree vs. all S-loci gene tree **(D)** Species tree vs. tree based on S-locus single-copy genes only ; **(E)** *S-RNase* gene tree vs. S-locus single-copy genes tree ; **(F)** *S-RNase* gene tree vs. tree derived from presence/absence matrix of SFBB genes. Each line links identical haplotypes (h1 to h32) between the trees being compared. Colored connectors highlight haplotypes exhibiting strong or consistent topological congruence across comparisons. Horizontal axes indicate phylogenetic distances. Tree topologies were computed using hierarchical clustering based on pairwise genetic distances. Two independent color schemes are used to facilitate interpretation: 1. Species colors: Red = *M. domestica*; Green = *M. sylvestris*; Yellow = *M. orientalis*; Purple = *M. sieversii*. 2. S-allele colors: Colors correspond to specific S-alleles: Pink: MdS2 ; Brown: MdSf ; Light green: MdS5 ; Blue: MdS4 ; Light yellow: MdS9 ; Salmon: MdSe.

Supplementary Table 5: SFBB database, public accessions from *Malus* and *Pyrus* (excel file).

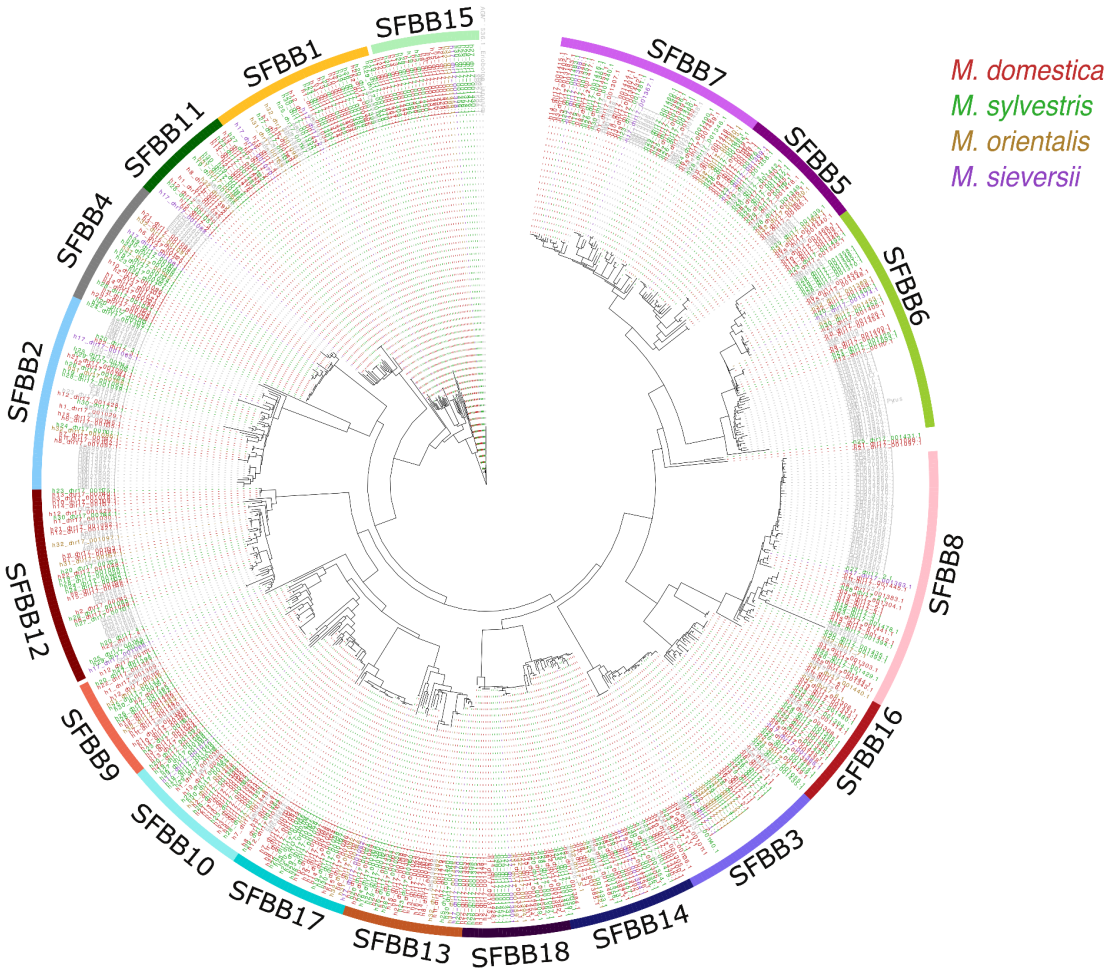

Supplementary Fig. 3: SFBB genes phylogeny and families determined using combination of classification methods. Phylogenetic tree based on the alignment of SFBB protein sequences from *Malus* S-haplotypes included in this study, along with publicly available SFBB sequences. Protein sequences were aligned using Clustal Omega (Sievers & Higgins, 2014), and the tree was inferred with IQ-TREE (Minh et al., 2020) using 1000 bootstrap replicates. Hierarchical clustering using Ward method was combined to Orthogroups identification using Orthofinder (Emms & Kelly, 2019) to determine SFBB families, which were compared to those of publicly available SFBB sequences. Tip labels are color-coded according to the species origin of the S-haplotype from which each SFBB sequence was derived.

Supplementary Table 6: SFBB from assembly set, coordinates and families (excel file).

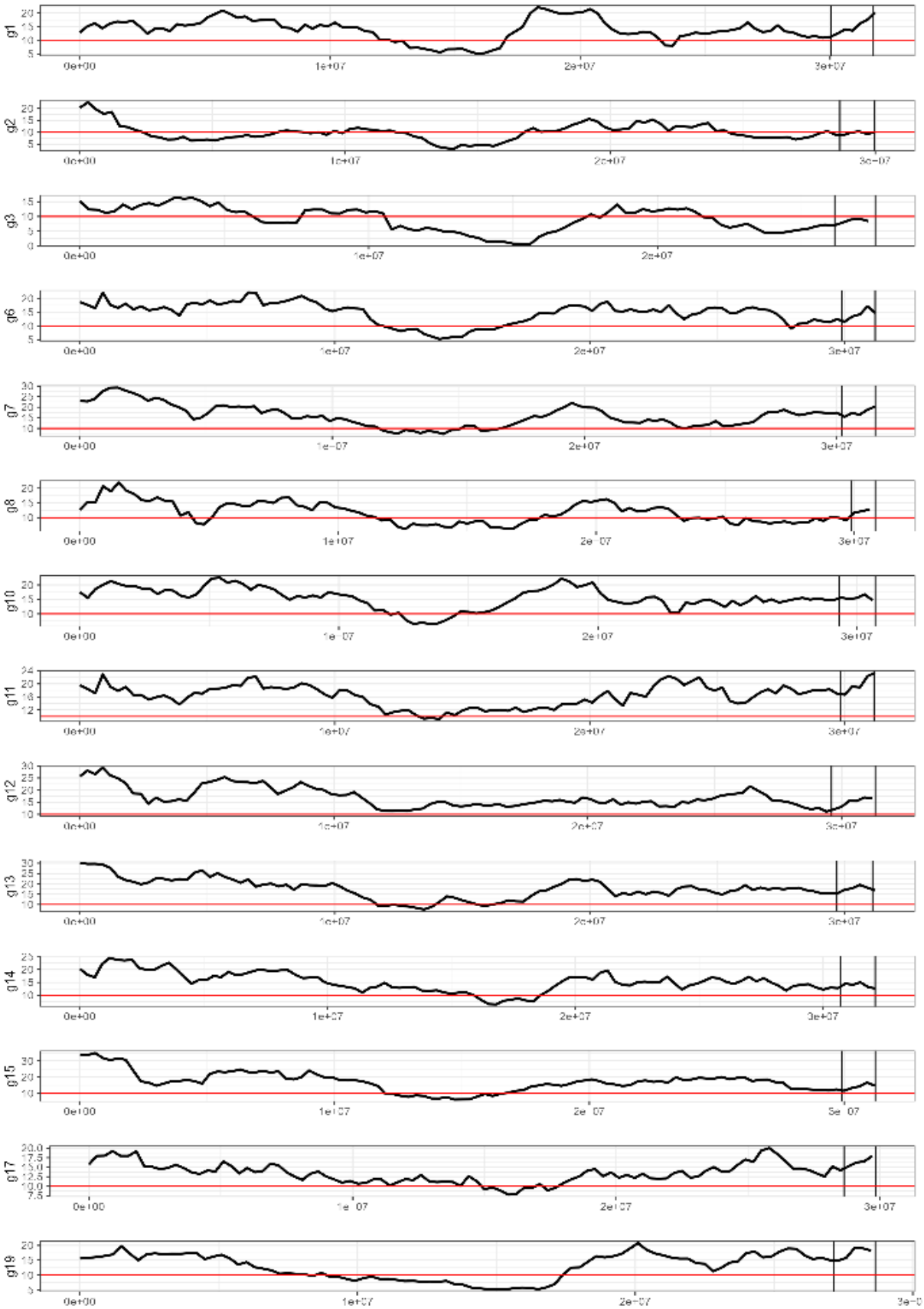

Supplementary Fig. 4: Variation of the LTR Assembly Index (LAI) along chromosome 17 for different *Malus* assemblies. Each panel corresponds to a distinct assembly. Black lines represent local LAI values, while

the horizontal red line indicates the quality threshold. The S-locus region is delimited by the two vertical bars at the right end of each plot.

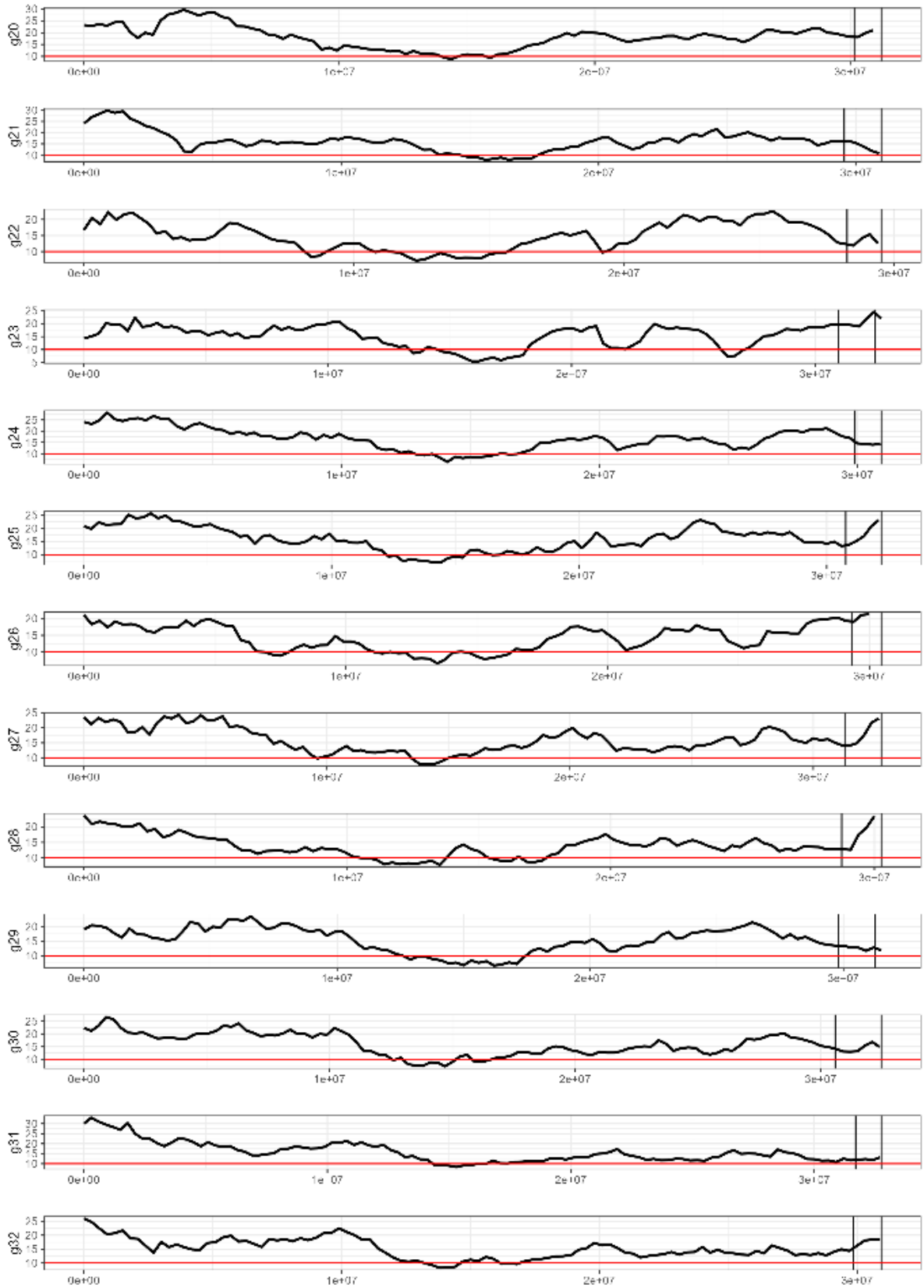

Supplementary Fig. 4 (continued)

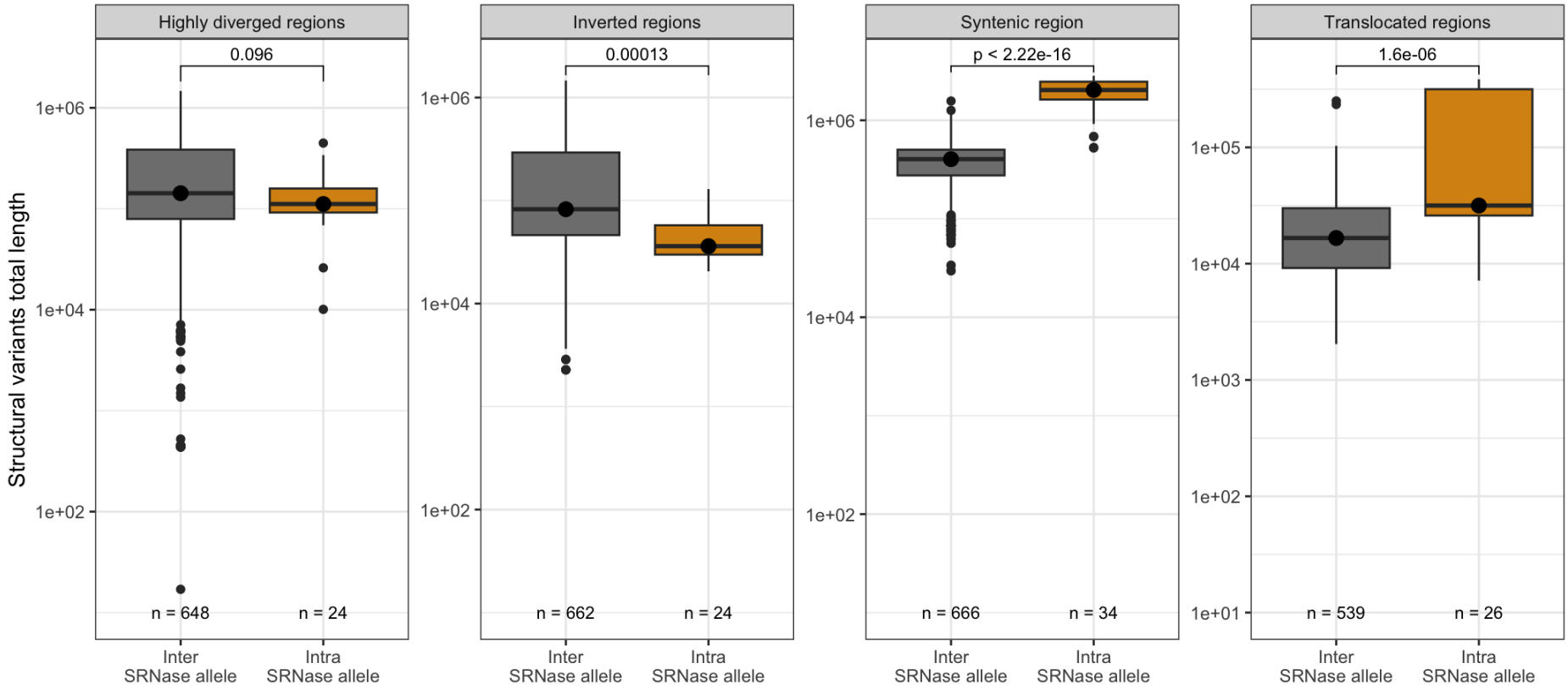

Supplementary Fig. 5: Structural variant and syntenic regions size distribution between S-locus haplotypes sharing the same or different S-RNase alleles. Boxplots showing the distribution of region sizes (in bp, log scale) for different types of structural variants detected in pairwise alignments of S-locus haplotypes, categorized by whether the two haplotypes share the same S-RNase allele (*intra S-RNase allele*, orange) or not (*inter S-RNase allele*, gray). Structural variant classes include inverted regions, translocated regions and highly diverged regions, as defined by SyRI. For each category, the median region size is indicated along with results from a Wilcoxon–Mann–Whitney test comparing intra vs. inter S-RNase groups. *W* statistics, *p*-values are reported above each plot. Syntenic regions are significantly larger between haplotypes with the same S-RNase allele (*p-value* < 2.2e−16), whereas inverted regions are significantly larger (*p-value* = 8.9e-5) in comparisons between different S-RNases, suggesting increased structural divergence between non-homologous S-haplotypes.

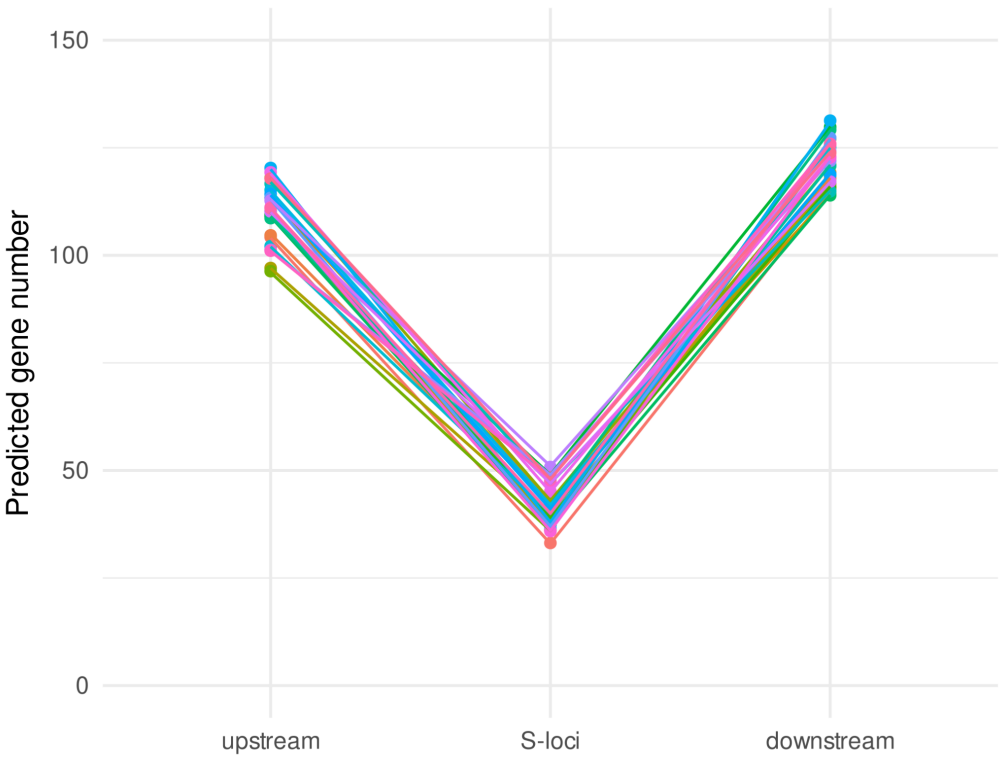

Supplementary Fig. 6: Predicted gene number inside S-loci and in same length regions (1.35 Mb) upstream and downstream. Each point is one haplotype region, and regions from the same haplotypes have the same color and are linked by the same color line.

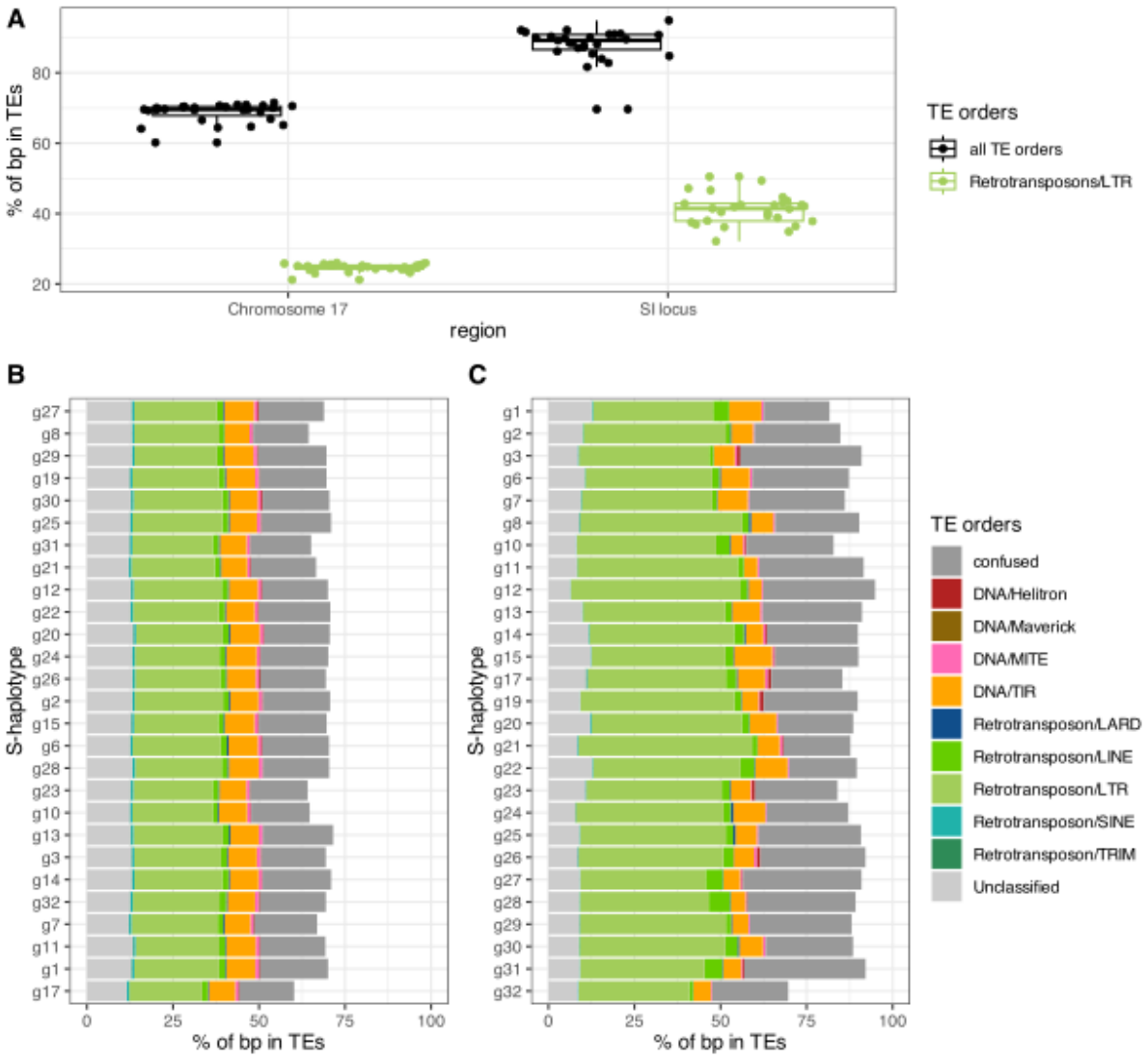

Supplementary Fig. 7: Chromosome 17 and S-loci TEs content in *Malus* haplotypes add7 window size. Base percentage in TE appears higher in S-loci than in chromosome 17 (A, black points) and the difference is more pronounced for LTR retrotransposons (A, green points). TEs families proportion appears conserved in different chromosome 17 (B) and less conserved across SI loci, even with the same S allele (C). The confused category corresponds to TEs for which the classification assigned multiple possible families without a clear preference for one family over another.

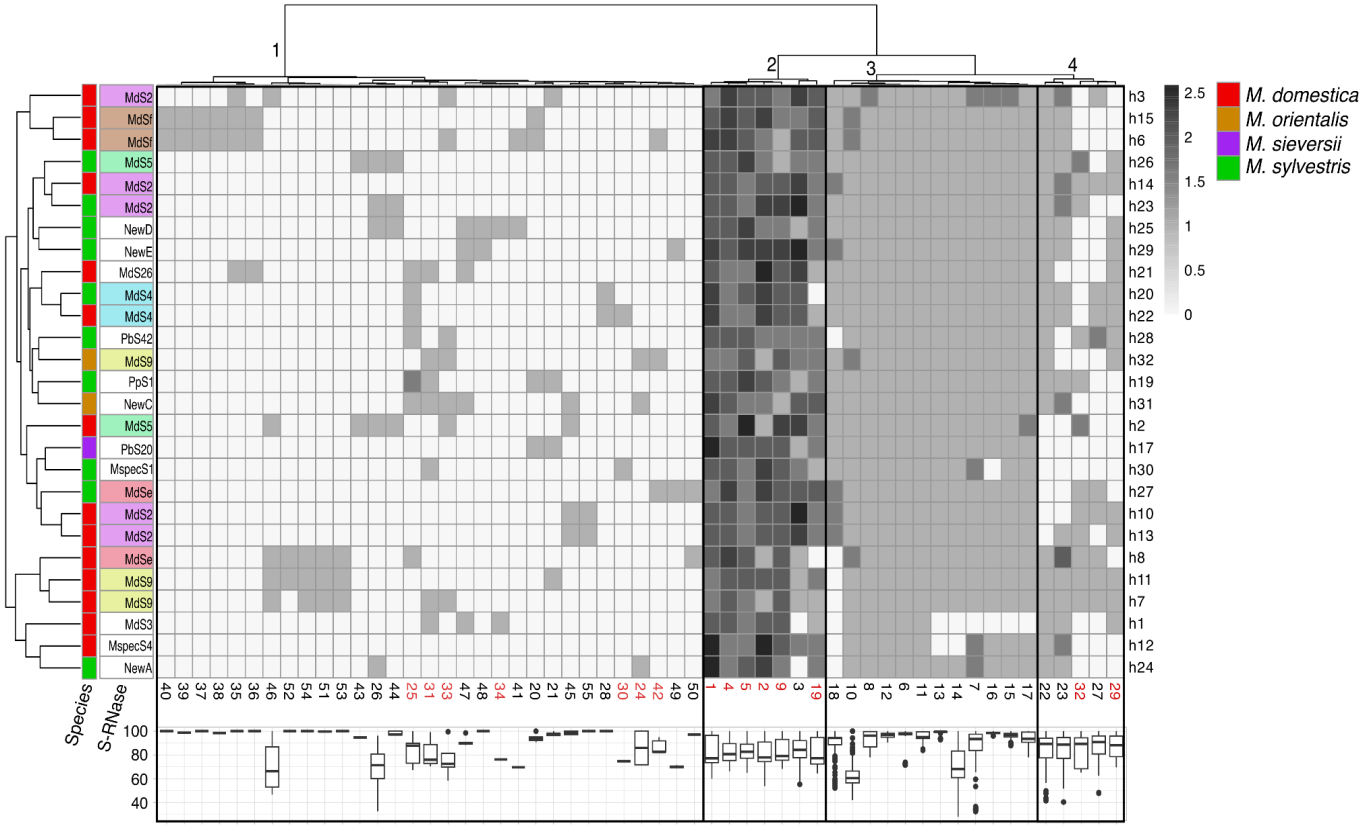

Supplementary Fig. 8: Heatmap showing the number of genes from each synteny cluster present in individual S-haplotypes. Each column represents a gene cluster inferred by syntenet from the *S*-locus region. Each row corresponds to an *S*-haplotype from one of four *Malus* species (*M. domestica*, *M. sylvestris*, *M. sieversii*, *M. orientalis*), annotated by species (left color strip) and *S*-allele (right color strip). The grayscale indicates the log-transformed gene count ($\log_2(n + 1)$) for each cluster within each *S*-haplotype. Cluster IDs are shown below each column; those highlighted in red contain known SFBB genes, which are involved in the self-incompatibility system. Both *S*-haplotypes and gene clusters were hierarchically clustered based on gene content similarity. Based on their distribution across S-haplotypes, gene clusters were grouped into four categories. Group 2 includes clusters 19, 3, 9, 2, 4, 1, and 5, which are present in all S-haplotypes in multiple copies. This group is composed mostly of SFBB gene clusters, with the exception of cluster 3, which contains genes encoding a serine/threonine-protein kinase and transcription factors. Group 3 contains clusters 15, 8, 16, 17, 7, 14, 13, 11, 6, 12, 10, and 18, which typically include a single gene copy per haplotype. These include the S-RNase gene (cluster 10), as well as genes encoding a DNA ligase, a C2H2-type zinc finger, and a coatomer subunit. Groups 1 and 4 consist of clusters that are not consistently present across all haplotypes. Clusters in group 1 are rarer than those in group 4. Notably, some SFBB gene clusters are also found in these two groups, indicating variable copy number and presence across haplotypes. The full gene composition of each cluster is provided in Supplementary Table 7.

Supplementary Table 7: Gene content of S-locus clusters across the 27 Malus haplotypes. For each cluster group and individual cluster, the table lists the gene identifiers present, their putative functions (e.g., SFBB family membership or other annotated domains), and the corresponding S-haplotypes when available (excel file).

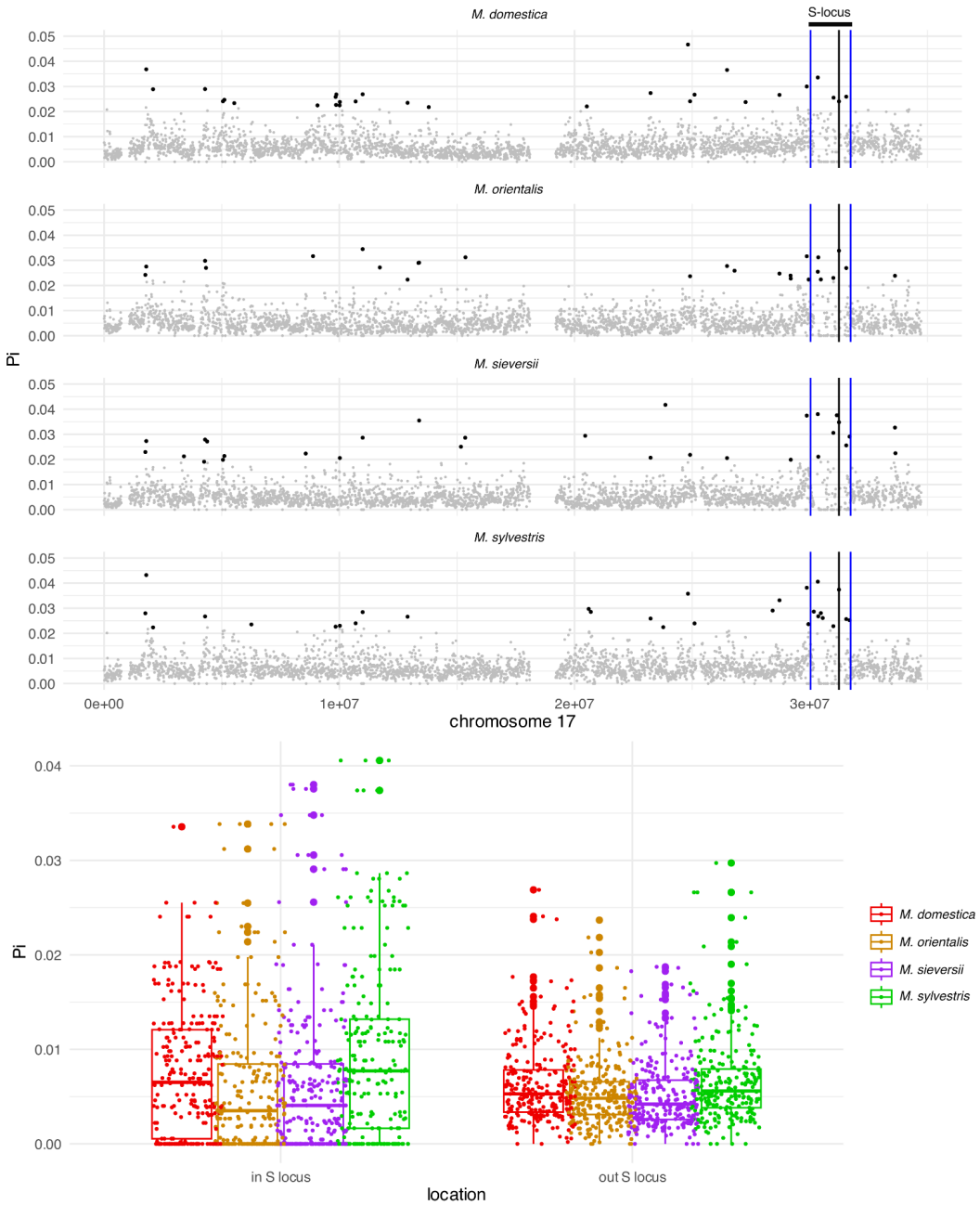

Supplementary Fig. 9: Nucleotide diversity (π) on chromosome 17 across four *Malus* species. (Top) Genome-wide distribution of nucleotide diversity on chromosome 17 in *M. domestica*, *M. orientalis*, *M. sieversii* and *M. sylvestris*, calculated in 10 kb non-overlapping windows using pixy. Black dots represent the top 1% windows in terms of π, calculated separately for each species. The region corresponding to the S-locus (as annotated in GDDH13, Daccord et al. 2017, corresponding to haplotype h1 in this study) is highlighted in blue. In all four species, the number of top 1% windows falling within the S-locus was significantly higher than expected by chance based on 10,000 random permutations (*M. domestica*: p-value = 1.07e-2, *M. orientalis*: 3e-4, *M. sieversii*: 1e-4, *M. sylvestris*: 1e-4). (Bottom) Boxplots of nucleotide diversity for 1,000 randomly sampled windows located inside vs. outside the S-locus, for each species. Each dot represents a 10 kb window. Colors correspond to species.

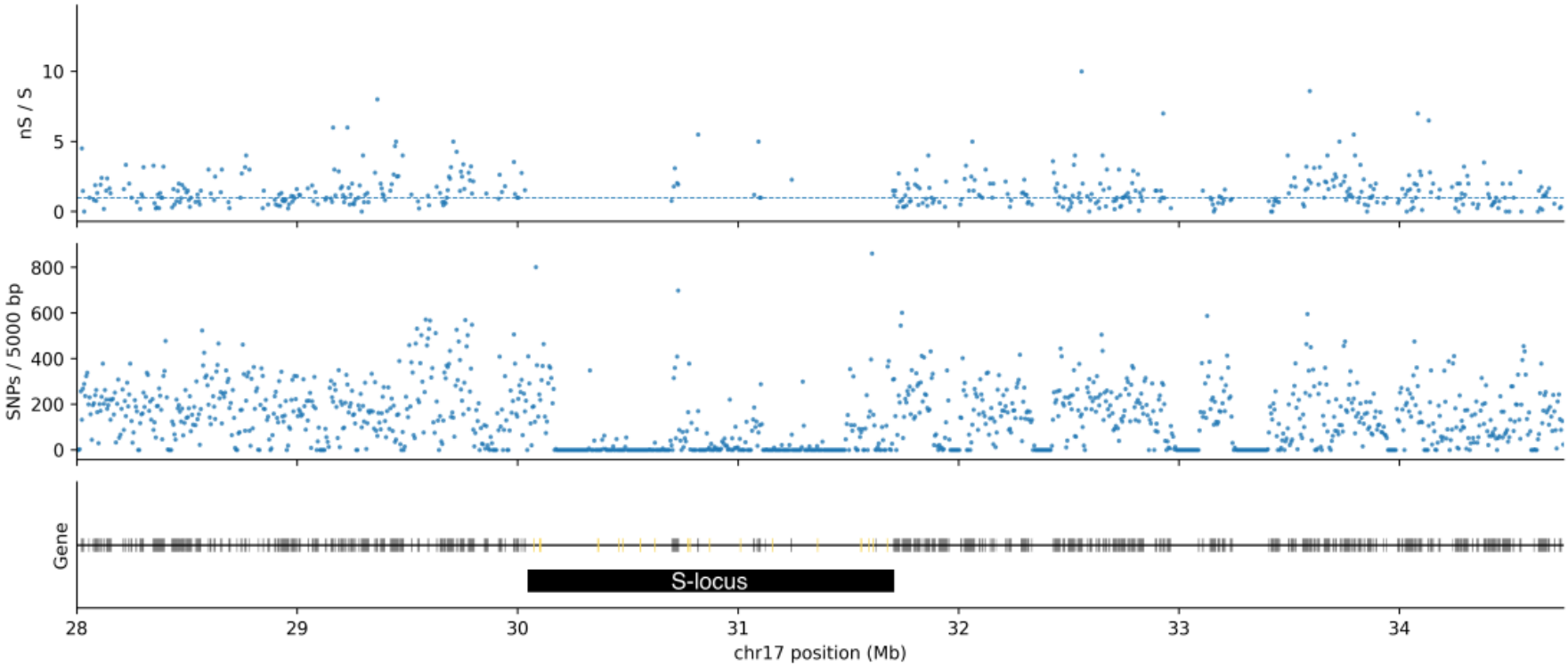

Supplementary Fig. 10: Distribution of SNP density and nS/S ratio along chromosome 17 in *Malus*. SNP density and the ratio of non-synonymous to synonymous variants (nS/S) were calculated in non-overlapping 5 kb windows along chromosome 17. (Top) Ratio of non-synonymous to synonymous substitutions (nS/S). The dashed horizontal line indicates a ratio of 1. (Middle) SNP density per 5 kb window. (Bottom) Gene track showing the position of annotated genes (gray rectangles) and SFBB genes (yellow rectangles) and the coordinates of the S-locus (black bar).

Supplementary Table 8: Detection of positive selection on SFBB genes in each S-haplotype using site models implemented in PAML / CodeML. Results of site models (M0, M1a, M2a, M3, M7, M8) fitted to codon alignments of SFBB genes from haplotypes h1 to h32. For each haplotype, the number of SFBB sequences included (**N**) and the total alignment length in codons (**S**) are indicated. **M0** assumes a single ω ratio for all sites and branches.**M1a** (neutral) and **M2a** (selection) compare models with and without a class of positively selected sites (ω > 1). **M3** allows discrete site classes with different ω values. **M7** (beta distribution) and **M8** (beta + ω > 1) are alternative site models for detecting selection. Model parameters shown include the log-likelihood (lnL), site class proportions (p_0, p_1, p_2), and dN/dS ratios (ω, ω_0, ω_1, ω_2) (excel file).

Supplementary Table 9: Likelihood ratio tests (LRTs) for detection of positive selection on SFBB genes in individual S-haplotypes. Results of model comparisons conducted using codeml (PAML) on codon alignments of SFBB genes from haplotypes h1 to h32. For each haplotype, three likelihood ratio tests were performed to evaluate the presence of **codons under positive selection**: **M0 vs M3**: compares a one-ratio model (M0) to a discrete model allowing for multiple site classes (M3), testing for variable selection pressure across sites. **M1a vs M2a**: tests for the presence of positively selected codons (ω > 1) by comparing a neutral model (M1a) to a selection model (M2a). **M7 vs M8**: compares a beta-distributed ω model (M7, without selection) to a model allowing an extra site class with ω > 1 (M8). For each comparison, the table reports log-likelihoods (lnL) of both models, the test statistic -2Δℓ, degrees of freedom (**K**), significance level (**alpha**), associated *p*-value, and the chi-squared critical value for 5% significance ($X^2(\alpha)$) (excel file).

Supplementary Table 10: Amino acids observed at positively selected sites across SFBB families in 27 S-haplotypes. For each of the 27 S-haplotypes, the table lists the amino acid residues found at the codon positions most frequently inferred to be under positive selection (posterior probability > 0.95 in PAML analyses). Each cell contains the amino acids present in the given haplotype for a given SFBB family; "absent" indicates that the SFBB gene was not detected in that haplotype (excel file).

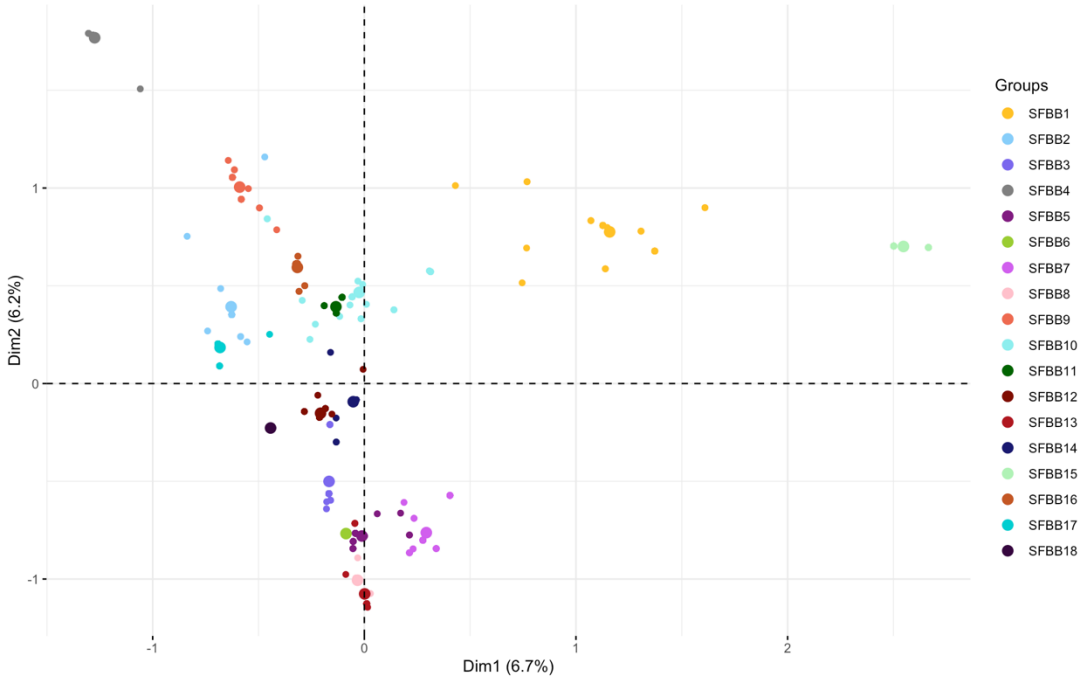

Supplementary Fig. 11. Clustering of SFBB genes based on amino acid identity at conserved positions. Multiple correspondence analysis (MCA) was performed using amino acid residues at selected conserved positions across SFBB genes. Each point represents a gene, colored according to its SFBB family. The first two dimensions, which together explain XX% of the total variance (Dim1: 6.7%, Dim2: 6.2%), reveal a structured separation of gene families. Families with similar amino acid profiles tend to cluster together, while others form

well-defined and distinct groups in the multivariate space. Ellipses represent 95% confidence intervals for each family.

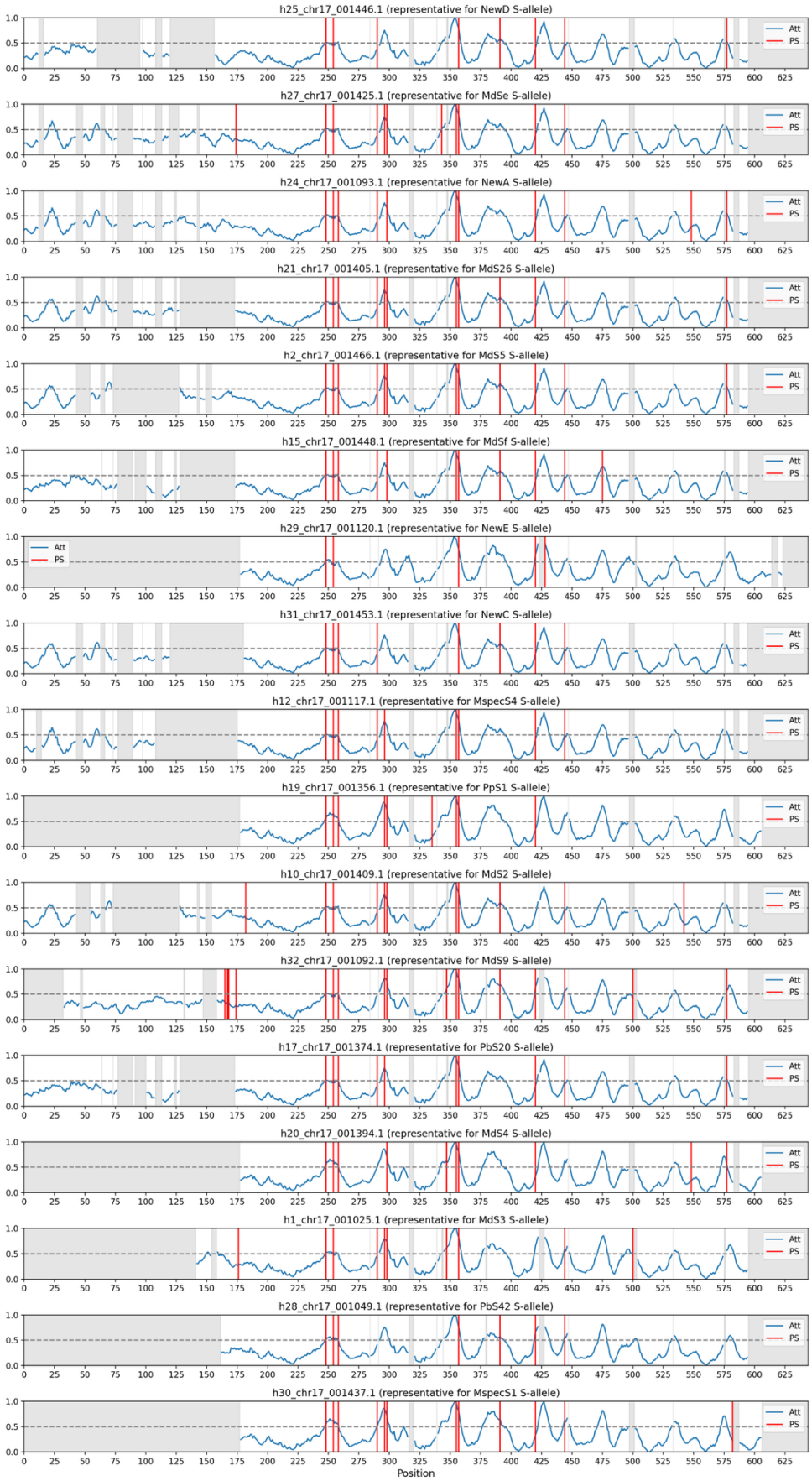

Supplementary Fig. 12: Alignment of MuLAN attention scores and positively selected sites across *Malus* SFBB proteins. For SFBB genes associated with a distinct S-allele, we plotted MuLAN attention scores (blue)

along the amino acid sequence to estimate the predicted functional relevance of each residue. Vertical red lines indicate sites inferred to be under positive selection. Several of these sites co-localize with peaks in attention scores, suggesting that positively selected residues tend to coincide with positions predicted to have high functional impact. Gray-shaded regions represent alignment gaps or poorly aligned regions excluded from the analysis.

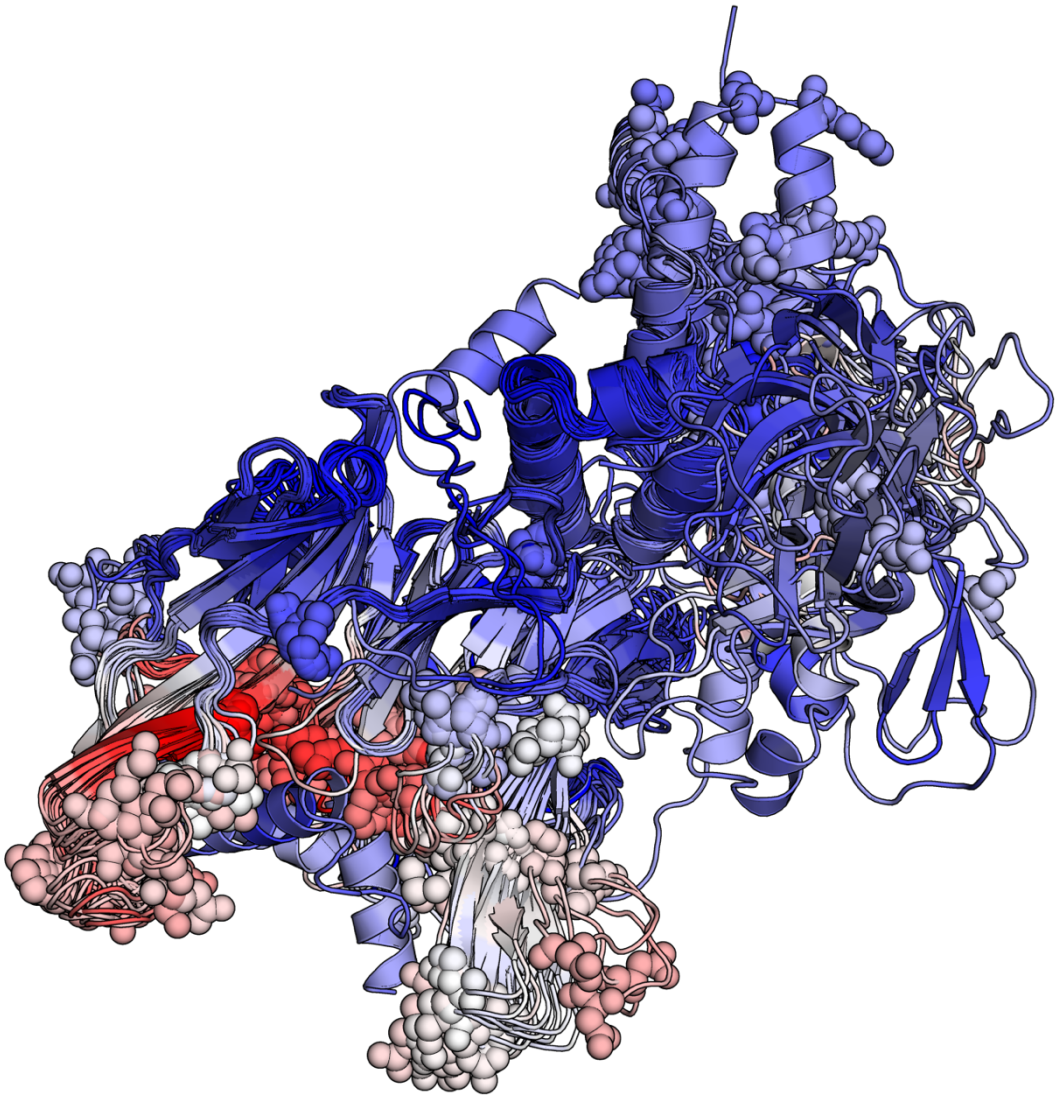

Supplementary Fig. 13: Structural representation of *Malus* SFBBs highlighting positively selected sites. Ribbon diagram of SFBB structures predicted by Boltz-1, showing the typical α/β fold. The longest sequence for each S-allele was chosen as representative, totalling 17 sequences, and the resulting structures were aligned in PyMOL to minimize pairwise root mean square deviation of atomic positions. The spheres indicate amino acid residues inferred to be under positive selection across SFBB families (posterior probability > 0.95, Bayes Empirical Bayes analysis, CodeML). These selected sites are broadly distributed on the surface of the protein, suggesting their potential involvement in allele-specific recognition or interaction with pistil determinants. Structural elements are colored according to MuLAN attention scores. Red-to-white colors correspond to high while blue tones to low scores.

Supplementary Table 11: Amino acid composition at conserved codon positions across SFBB families. Matrix summarizing amino acid (AA) frequencies at ten codon positions previously identified as highly associated with SFBB family identity (see Table 2). Each row corresponds to a codon position, and each column represents one SFBB family. Within each cell, the observed amino acids and their relative frequencies (≥3%) are listed, based on all SFBB gene sequences belonging to the corresponding family. Gray cells indicate positions that are invariant within a family (i.e., a single AA observed at 100% frequency). Rows on the right indicate the number and proportion of SFBB families for which each position is invariant, highlighting positions with family-specific conservation. Similarly, the bottom row shows the number and proportion of invariant positions per SFBB family. These results support the presence of family-specific amino acid signatures likely contributing to functional diversification among SFBB proteins.

SFBB family	SFBB 1	SFBB 2	SFBB 3	SFBB 4	SFBB 5	SFBB 6	SFBB 7	SFBB 8	SFBB 9	SFBB10	SFBB 11	SFBB 12	SFBB 13	SFBB 14	SFBB 15	SFBB 16	SFBB 17	SFBB 18	Number of invariant family	Percentage
position 297	F:1	H:0.82, L:0.14, N:0.05	P:0.74, H:0.26	P:1	N:1	N:1	N:1	E:0.96, G:0.04	F:1	F:1	P:1	H:0.97, Q:0.03	E:0.89, D:0.11	P:1	F:1	F:1	Y:1	P:1	13	72%
position 299	Q:0.61, E:0.33, H:0.06	S:0.95, W:0.05	Q:0.81, H:0.19	V:1	E:1	Q:1	E:0.9, D:0.1	E:1	L:1	L:0.93, M:0.03, Q:0.03	Q:1	L:0.84, I:0.16	E:1	Q:1	E:1	Q:1	L:1	L:1	12	67%
position 336	H:0.48, P:0.42, C:0.03, D:0.03, R:0.03	D:0.86, N:0.09, S:0.05	N:0.81, D:0.19	D:1	D:0.92, N:0.08	D:1	N:0.67, D:0.23, Y:0.1	D:1	D:0.65, N:0.26, V:0.09	D:0.63, H:0.17, A:0.07, N:0.07, V:0.07	D:0.5, A:0.27, S:0.18, T:0.05	D:1	N:0.85, D:0.11, S:0.04	D:1	H:1	D:0.9, N:0.1	S:1	D:1	8	44%
position 356	I:0.97, V:0.03	T:0.91, N:0.05, S:0.05	T:1	S:1	V:0.8, I:0.12, T:0.08	L:1	T:0.82, I:0.18	T:1	S:0.83, T:0.13, N:0.04	T:1	I:1	D:1	T:1	I:1	I:1	T:1	V:0.96, I:0.04	T:1	12	67%
position 358	G:0.85, A:0.06, I:0.06, V:0.03	Q:1	H:1	G:1	K:1	K:1	K:1	K:1	Q:1	Q:0.97, L:0.03	E:1	G:1	K:1	G:0.9, R:0.1	T:1	E:1	R:1	R:1	15	83%
position 421	E:0.82, D:0.06, G:0.06, K:0.03, R:0.03	D:0.95, Y:0.05	S:0.81, T:0.19	K:1	D:1	D:1	E:1	K:0.96, I:0.04	T:0.96, R:0.04	Q:0.7, D:0.1, E:0.07, N:0.07, K:0.03, T:0.03	K:1	K:1	K:1	K:1	E:1	T:0.79, N:0.14, K:0.07	K:1	K:1	11	61%
position 429	H:0.88, D:0.06, Y:0.06	N:0.91, H:0.05, S:0.05	P:1	L:1	P:1	P:1	P:1	P:1	S:1	H:0.83, S:0.13, T:0.03	Q:1	P:1	P:1	P:1	C:1	S:1	S:0.96, T:0.04	P:1	14	78%
position 476	E:0.88, K:0.12	L:0.95, T:0.05	N:0.81, K:0.19	Q:1	K:0.96, E:0.04	K:1	K:0.95, N:0.05	K:1	R:1	T:0.97, K:0.03	K:1	E:1	K:1	K:0.97, R:0.03	K:1	T:1	K:1	K:1	11	61%

position 543	T:0.85, S:0.15	S:1	C:0.94, F:0.03, Y:0.03	S:1	C:0.64, Y:0.2, F:0.16	C:1	C:0.97, S:0.03	R:0.74, H:0.19, C:0.07	S:0.78, N:0.17, D:0.04	C:0.9, S:0.07, Y:0.03	S:1	C:0.9, G:0.1	H:0.85, C:0.11, Q:0.04	C:0.93, H:0.07	T:0.72, I:0.28	S:0.93, N:0.07	S:1	G:1	6	33%
position 549	V:0.91, F:0.06, A:0.03	V:0.95, I:0.05	V:1	A:0.8, T:0.15, V:0.05	L:1	L:1	L:1	I:1	L:1	L:0.9, M:0.07, V:0.03	V:1	I:0.77, L:0.19, F:0.03	I:0.89, L:0.11	L:1	E:1	L:1	L:0.82, I:0.18	L:1	11	61%
Number of invariant positions	1	2	4	9	6	10	5	7	6	2	9	6	6	7	9	7	7	10	113	63%
Percentage	10%	20%	40%	90%	60%	100%	50%	70%	60%	20%	90%	60%	60%	70%	90%	70%	70%	100%		

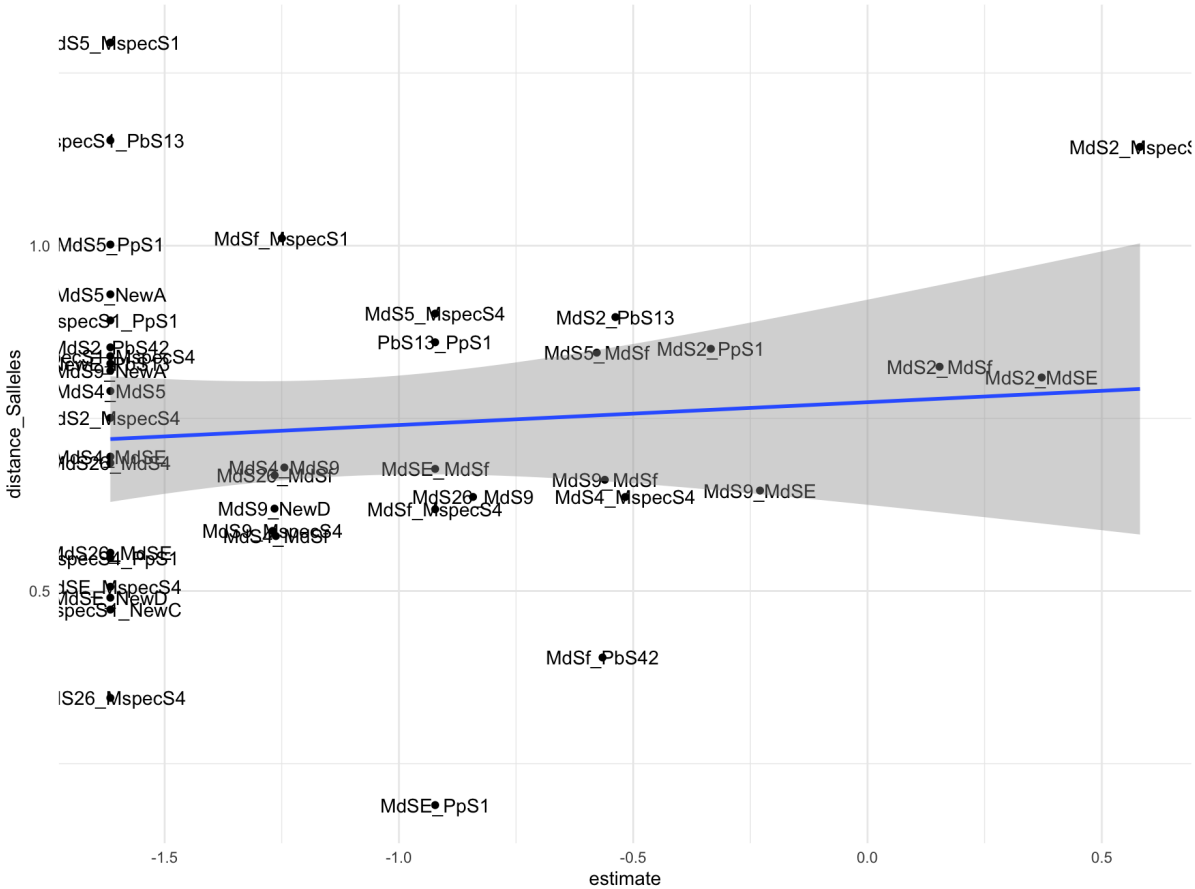

Supplementary Fig. 14. Relationship between phylogenetic distance of S-RNase alleles and frequency of gene conversion between S-haplotypes. Each point represents a pair of S-haplotypes, for which gene conversion events were inferred. The x-axis shows the estimate of gene conversion frequency (from the quasi-Poisson model), and the y-axis represents the cophenetic distance between the corresponding S-RNase alleles, extracted from the phylogenetic tree (Supplementary Fig. 1). The blue line shows the linear regression fit with 95% confidence interval (grey area). No significant correlation was detected (Pearson's r = 0.09, p = 0.57), suggesting that phylogenetic relatedness of S-RNases does not predict gene conversion intensity between their associated SFBB genes.

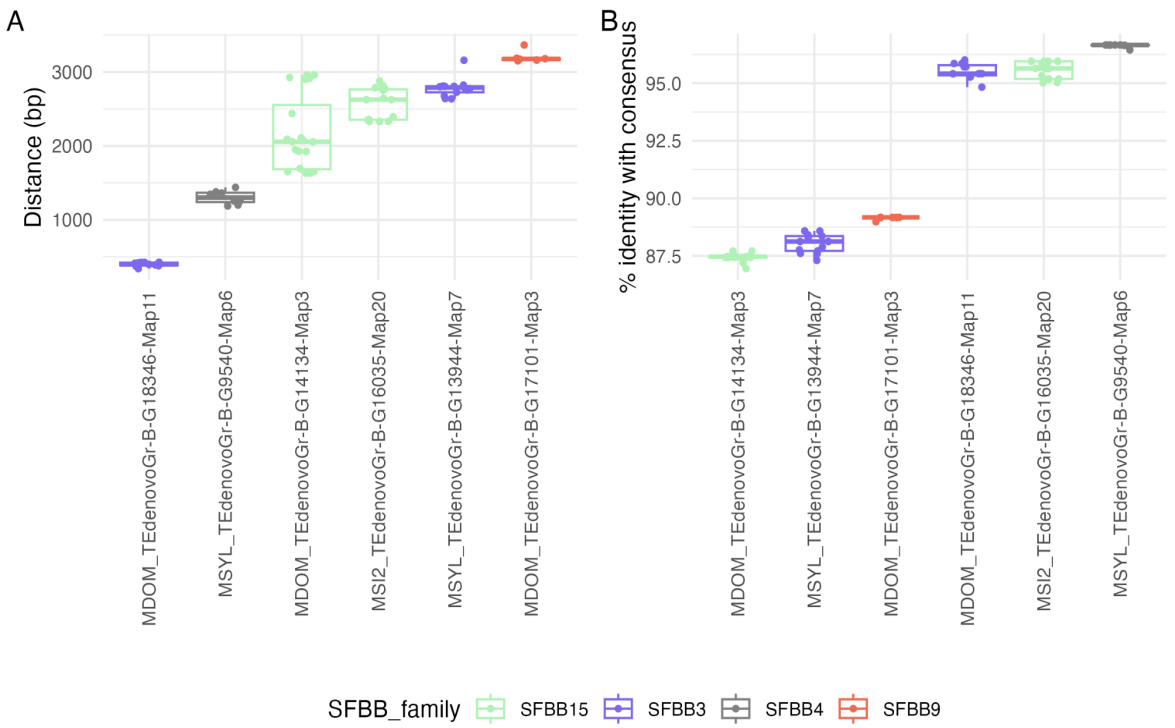

Supplementary Fig. 15: Distance and sequence identity of TE copies linked to SFBB gene families. (A) Distribution of distances (in base pairs) between SFBB genes and their associated TE copies, shown separately for each SFBB family. (B) Sequence identity (%) between TE copies associated with SFBB genes and the corresponding TE family consensus sequence.

Supplementary Table 13: Transposable elements (TEs) detected in association with SFBB genes in the Malus S-locus. Each row represents a TE consensus identified in proximity (< 4kb) to SFBB gene families across the 27 haplotypes analyzed. The columns indicate the class (I = retrotransposon, II = DNA transposon), order (e.g., LTR, TIR, MITE), superfamily (e.g., Ty/Gypsy, hAT, MuDR), and the closest match in RepBase (if any), which provides a putative annotation based on sequence similarity. "unclassified" indicates elements that could not be confidently assigned to a known TE category, and "–" marks missing or uncertain information.

TE REPET Consensus ID	Consensus size	class	order	superfamily	Match on RepBase
MSYL_TEdenovoGr-B-G9540-Map6	1818	II	TIR	hAT	HAT-4_Mad
MDOM_TEdenovoGr-B-G18346-Map11	691	II	TIR	hAT	HAT-10_Mad
MSI2_TEdenovoGr-B-G16035-Map20	649	II	TIR	MuDR	MuDR-4_Mad
MSYL_TEdenovoGr-B-G13944-Map7	574	I	LTR	Ty3/Gypsy	Gypsy-38_Mad
MDOM_TEdenovoGr-B-G14134-Map3	371	II	MITE	-	-
MDOM_TEdenovoGr-B-G17101-Map3	484	unclassified	unclassified	unclassified	-

Supplementary Table 12: Contextual information for TE–SFBB associations in the S-locus of *Malus*. This table reports only TE–SFBB pairs identified as significant in the permutation test. Each row corresponds to a TE copy located within 4 kb of an SFBB gene. For each TE, we report its consensus family, TE order, identity to the consensus, and haplotype of origin, along with the nearest upstream and downstream SFBB families and their respective distances. The relative position of the SFBB gene with respect to the TE (upstream, downstream, overlapping, or inside) is indicated. Haplotype metadata include species of origin and associated S-RNase allele. "Enriched" TE consensus and SFBB families pairs (excel file).

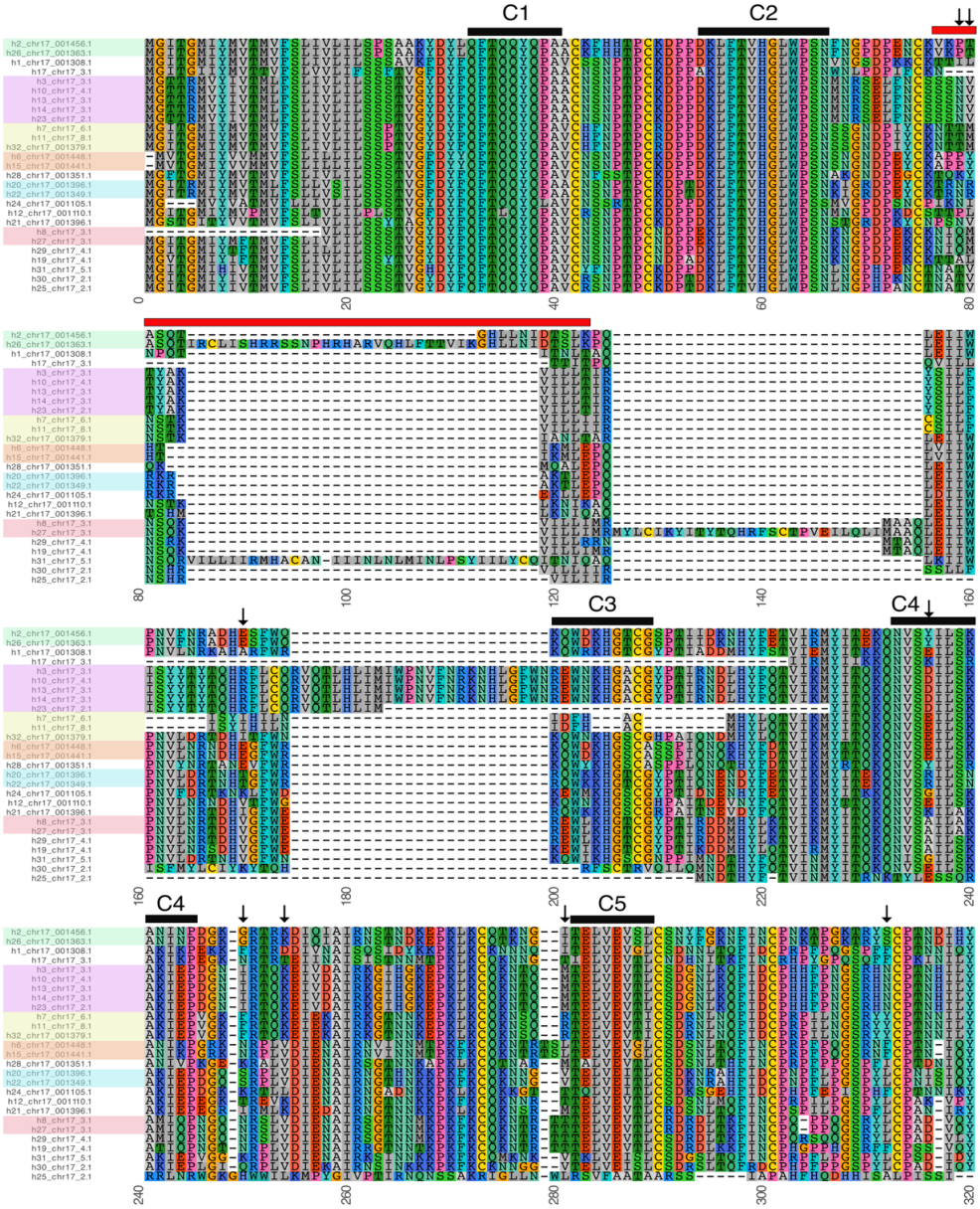

Supplementary Fig. 16: Multiple *Malus* S-RNase amino-acids sequence alignment. The background color of sequence names reflects their allele, with identical colors indicating the same S-RNase specificity. Each amino acid is represented by its one-letter code. Background colors indicate amino acid chemical properties, with similar colors assigned to residues of similar physicochemical characteristics (e.g., hydrophobic in grey, aromatic in cyan, acids in red, basics in blue, polar in green, specials in yellow, orange and pink). The alignment is divided into consecutive blocks of 80 amino acids for readability. Positions under diversifying selection are marked with an arrow (↓) above the alignment columns. Gaps introduced during the alignment process are shown in white. The putative hypervariable region (in red) defined by Ishimizu et al. (1998) and Ushijima et al. (1998) and five conserved regions (C1, C2, C3, C4 and C5) are underlined.

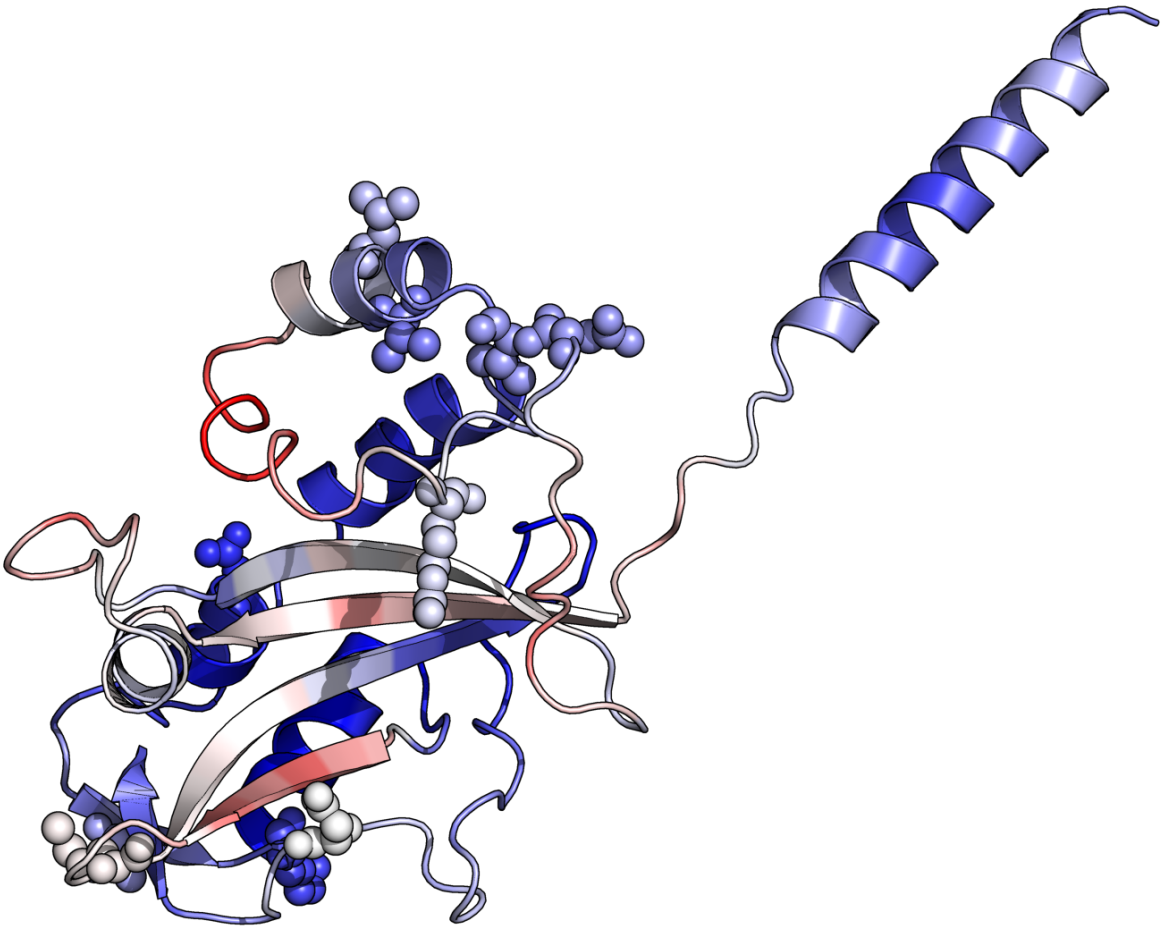

Supplementary figure 17: Structural representation of a *Malus* S-RNase highlighting positively selected sites. Ribbon diagram of a representative S-RNase protein structure (Accession MdS2_h23_chr17_2.1), showing the typical α/β fold. The spheres indicate amino acid residues inferred to be under positive selection across S-haplotypes (posterior probability > 0.95, Bayes Empirical Bayes analysis, CodeML). These selected sites are broadly distributed on the surface of the protein, suggesting their potential involvement in allele-specific recognition or interaction with pollen determinants. Structural elements are colored according to MuLAN attention scores. Red-to-white colors correspond to high while blue tones to low scores.

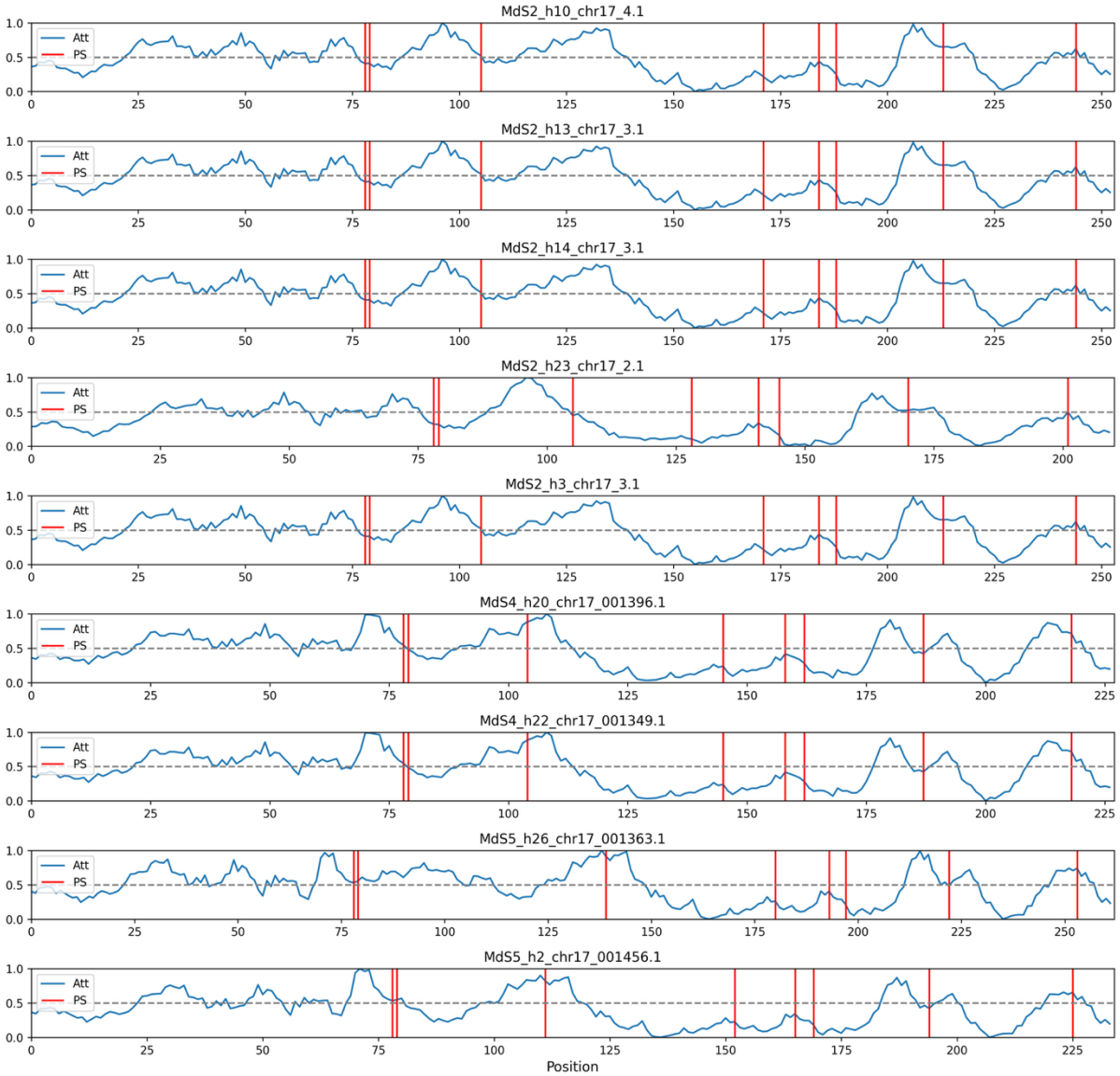

Supplementary Fig. 18: Comparison of MuLAN attention scores and positively selected sites across *Malus* S-RNase sequences. MuLAN attention scores (blue) are shown along the amino acid sequences of several S-RNases (MdS2, MdS4, MdS5). Vertical red lines mark positions inferred to be under positive selection (posterior probability > 0.95, CodeML analysis). While some positively selected sites coincide with peaks in attention scores, others appear in regions with low model-derived attention, suggesting that not all adaptively evolving residues are predicted to be functionally critical by the sequence-based model.

Supplementary Table 14. Putative targeting SFBB families determined for each S-RNases in the *Malus* dataset. Conclusions are based on the absence of SFBB families or on SFBB proteins mutations in S alleles. Sites located in the FBA domain, involved in the interaction with S-RNase are in bold characters.

S allele (S-RNase)	**Putative targeting SFBB family (supported by)**
MdS2 (5 haplotypes)	SFBB2 (absence from all haplotypes) SFBB3 (consistent AA variations on sites 299, **336**, **421** and **476**)
MdS4 (2 haplotypes)	SFBB11 (absence from all haplotypes)
MdS5 (2 haplotypes)	SFBB11 (absence from all haplotypes)
MdS9 (3 haplotypes)	SFBB12 (consistent AA variation on site 543), SFBB13 (consistent AA variation on sites 297, **336**, 543, 549), SFBB16 (consistent AA variation on site **336**)
MdSf (2 haplotypes)	SFBB5 (consistent AA variation on site **336**), SFBB7 (consistent AA variation on site **476**)
MdSe (2 haplotypes)	SFBB9 (absence from all haplotypes)

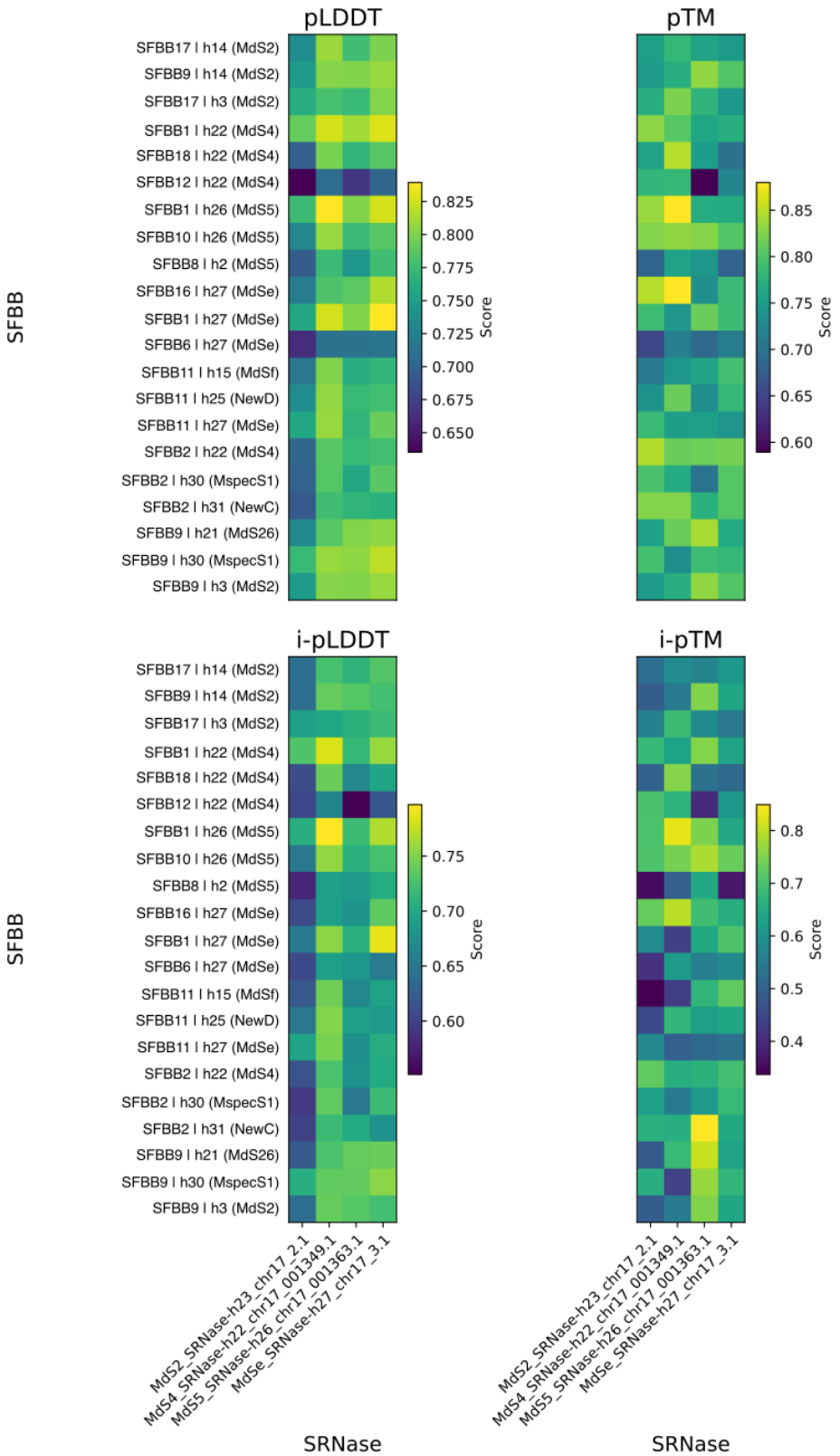

Supplementary Fig. 19: Predicted interaction scores between *Malus* SFBB proteins and S-RNases. Interaction predictions were computed using the Boltz-1 model for all pairwise combinations of 21 SFBB proteins (y-axis) and four S-RNase proteins (x-axis). Four different metrics are shown: pLDDT (predicted local distance difference test, top left), pTM (predicted template modeling score, top right), i-pLDDT (interface pLDDT, bottom left), and i-pTM (interface pTM, bottom right), each representing different confidence measures of the predicted protein–protein interaction. Lighter colors indicate higher predicted interaction scores. SFBB identifiers include family and haplotype. S-RNase identifiers include family, haplotype and gene id.

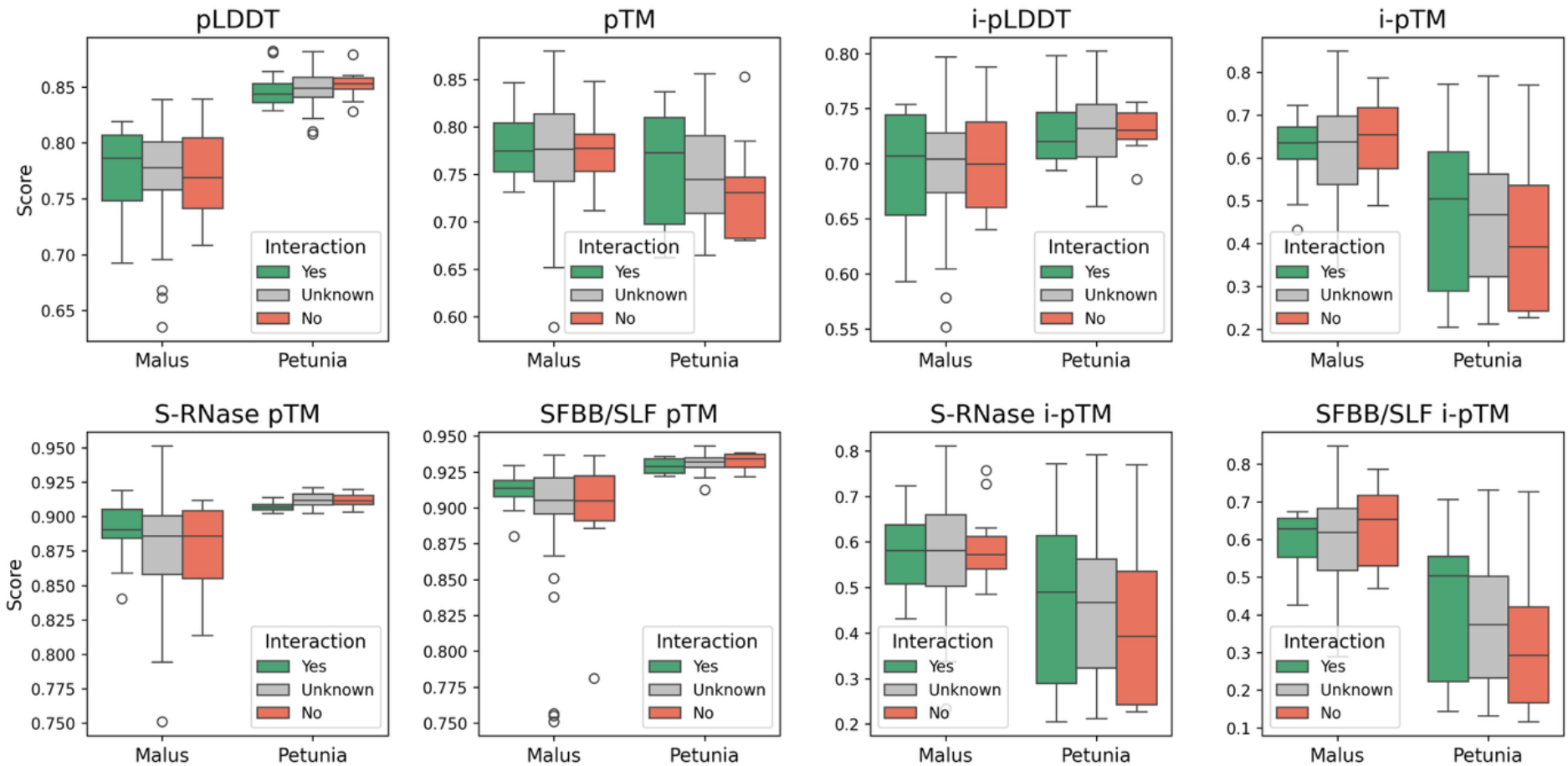

Supplementary Fig. 20: Structural confidence scores for S-RNase and SFBB/SLF models and predicted complexes in *Malus* and *Petunia*. Distributions of pLDDT, pTM, i-pLDDT and i-pTM scores for individual proteins and predicted SFBB/SLF–S-RNase complexes. Interaction categories correspond to expected (Yes, in green), unsupported (No, in red), or unknown (Unknown, in grey) functional relationships. In *Malus*, score distributions overlap substantially between categories, indicating that structural confidence metrics alone do not discriminate interacting from non-interacting pairs. In *Petunia*, mean scores are generally higher, but the separation between known and unknown interactions remains incomplete.

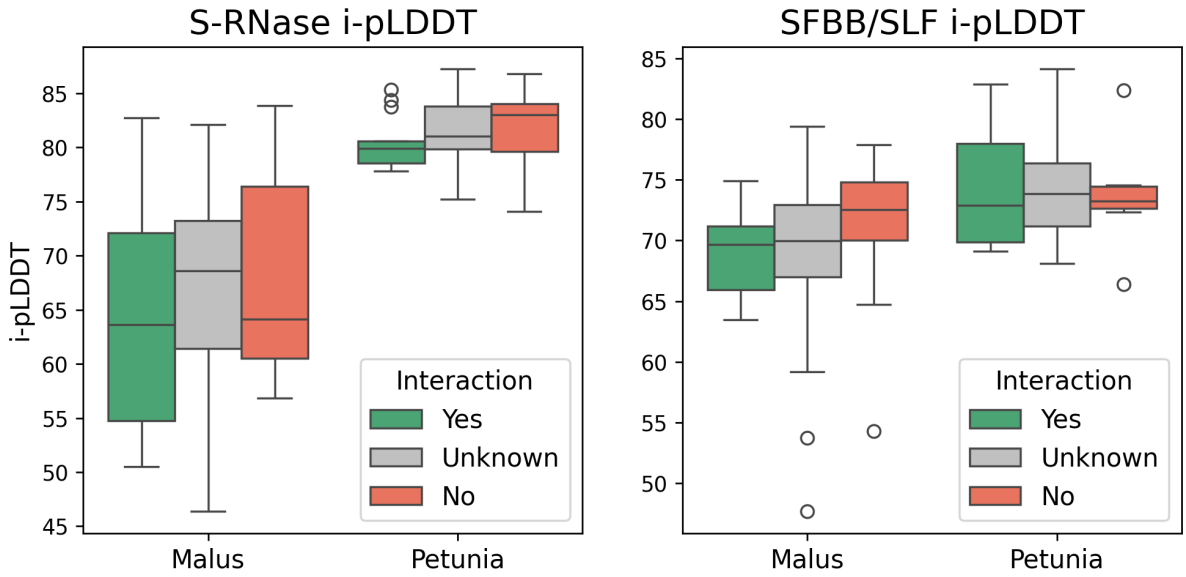

Supplementary Fig. 21: i-pLDDT confidence scores for individual S-RNase and SFBB/SLF protein models. i-pLDDT scores for isolated protein chains (i.e., outside the docking context) in *Malus* and *Petunia*. Chain-level models exhibit higher and more consistent confidence than complex-level models, indicating that the folded structures themselves are robustly predicted, whereas the inferred interfaces contribute most of the uncertainty. Although *Petunia* proteins show generally higher confidence values, these do not reliably distinguish known interacting pairs from non-interacting combinations.

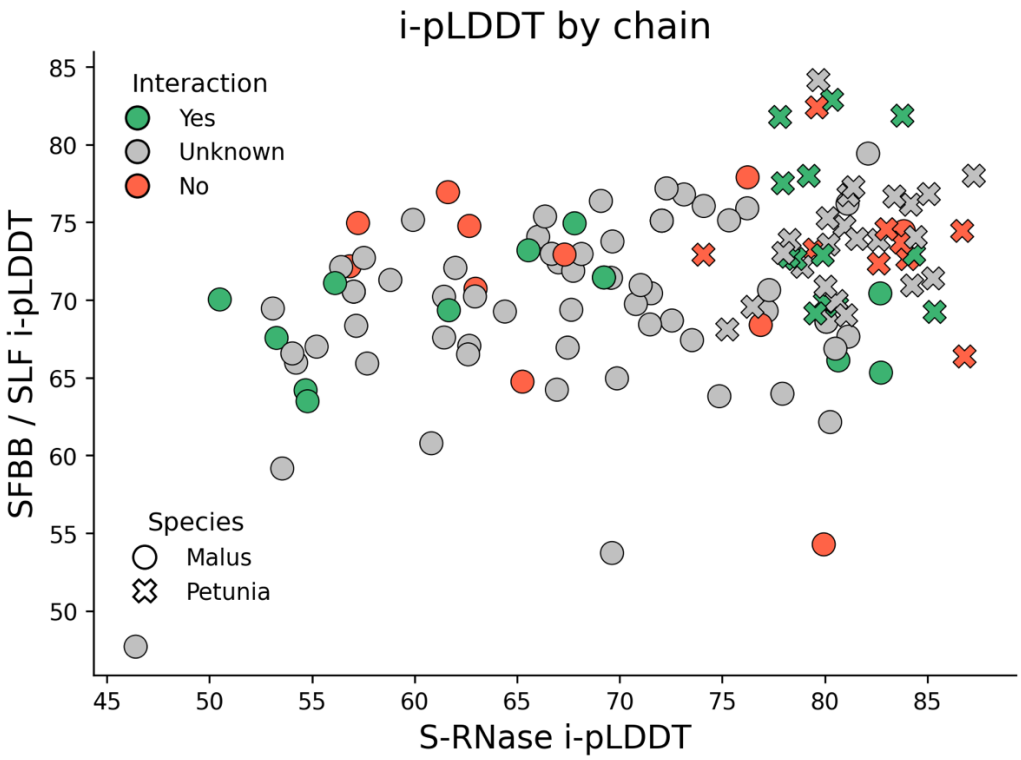

Supplementary Fig. 22: Relationship between S-RNase and SFBB/SLF interaction confidence across predicted complexes. Each point represents a predicted S-RNase–SFBB/SLF complex, plotted by the i-pLDDT score of each partner. Colors indicate expected interaction status, and symbol shapes distinguish *Malus* (circles) and *Petunia* (crosses). Although *Petunia* complexes tend to show higher i-pLDDT values overall, the ranges overlap across interaction categories, including several experimentally validated pairs. This indicates limited predictive resolution for interaction specificity based on Boltz-1 docking confidence alone.

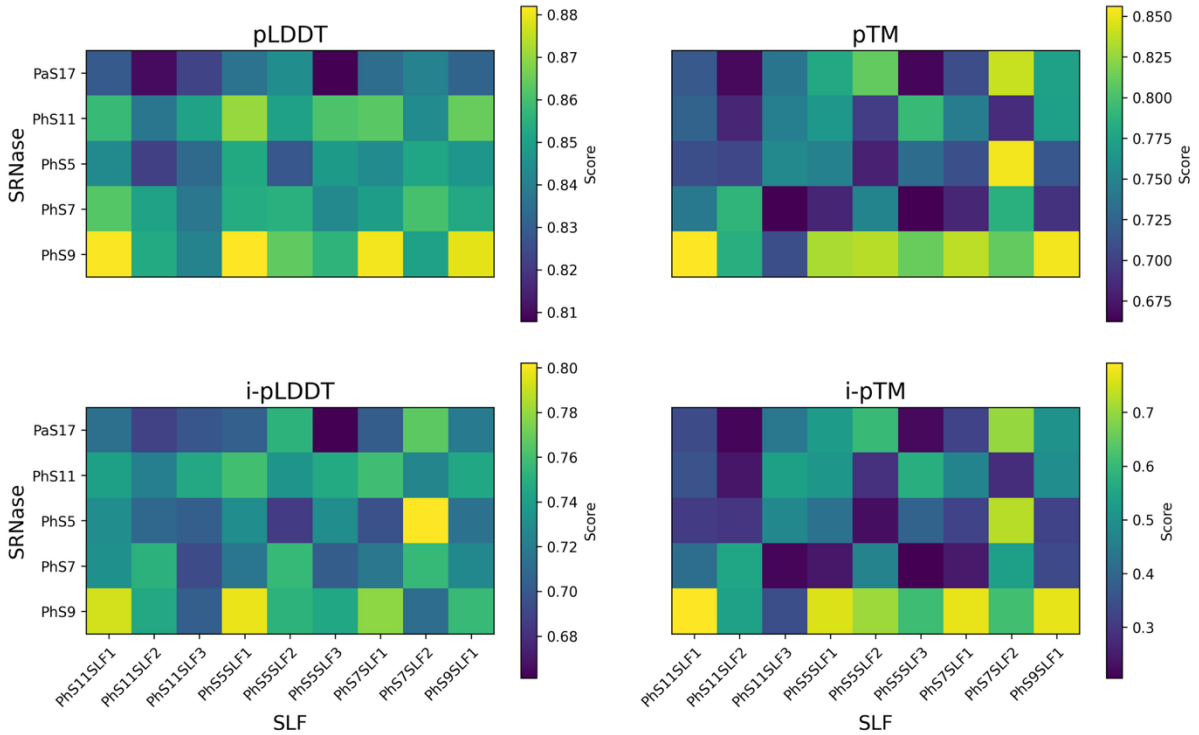

Supplementary Fig. 23: Predicted interaction scores between *Petunia* SLF proteins and S-RNases. Interaction predictions were computed using the Boltz-1 model for all pairwise combinations of 9 SLF proteins (x-axis) and five S-RNase proteins (y-axis). Four different metrics are shown: pLDDT (predicted local distance difference test, top left), pTM (predicted template modeling score, top right), i-pLDDT (interface pLDDT, bottom left), and i-pTM (interface pTM, bottom right), each representing different confidence measures of the predicted protein–protein interaction. Lighter colors indicate higher predicted interaction scores. SLF and S-RNase identifiers include haplotype and gene id.

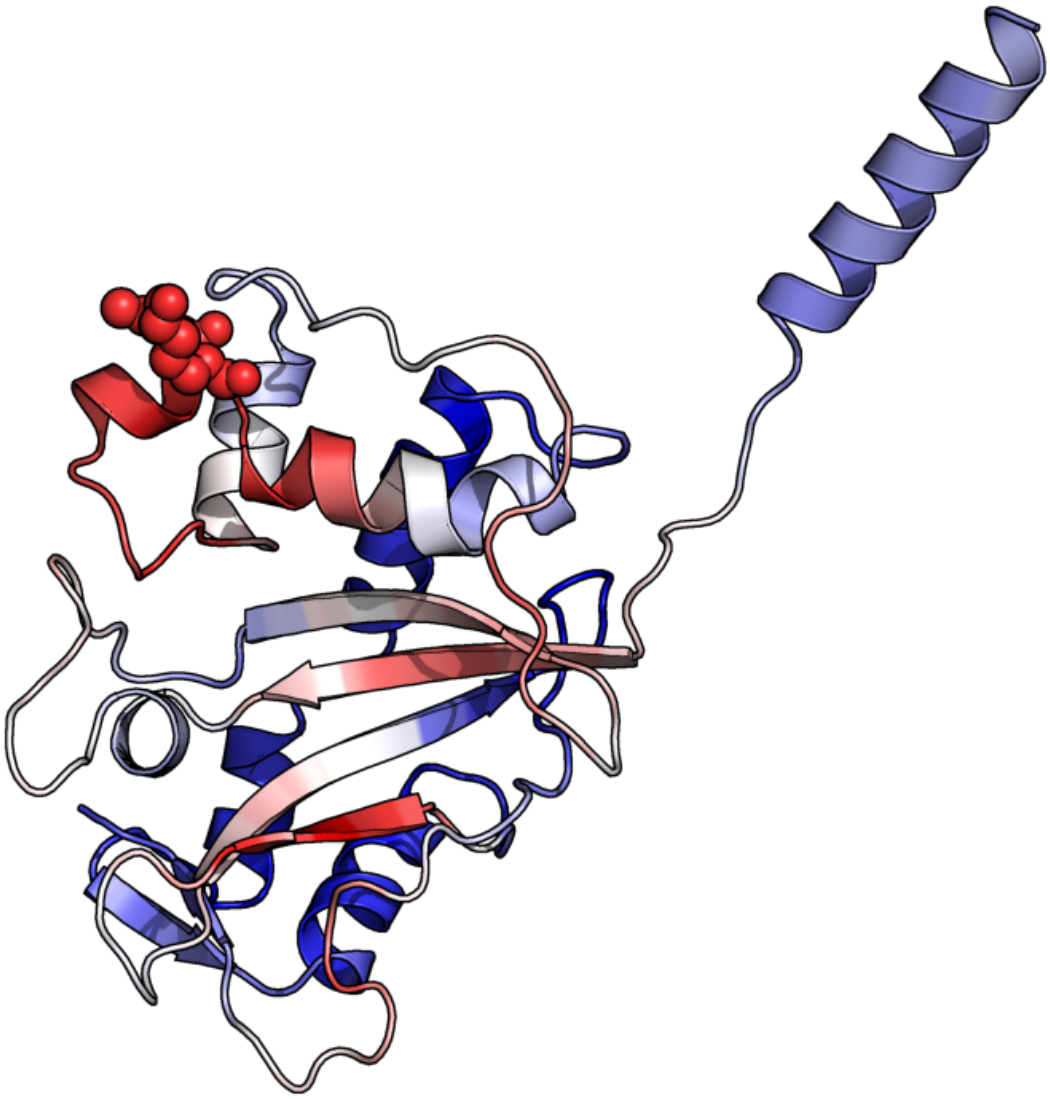

Supplementary Fig. 24: Structural representation of a *Petunia* S-RNase highlighting positively selected sites. Ribbon diagram of a representative S-RNase protein structure (Accession LC819199), showing the typical α/β fold. The spheres indicate amino acid residues inferred to be under positive selection across S-haplotypes (posterior probability > 0.95, Bayes Empirical Bayes analysis, CodeML). These selected sites are broadly distributed on the surface of the protein, suggesting their potential involvement in allele-specific recognition or interaction with pollen determinants. Structural elements are colored according to MuLAN attention score. Red-to-white colors correspond to high while blue tones to low scores.

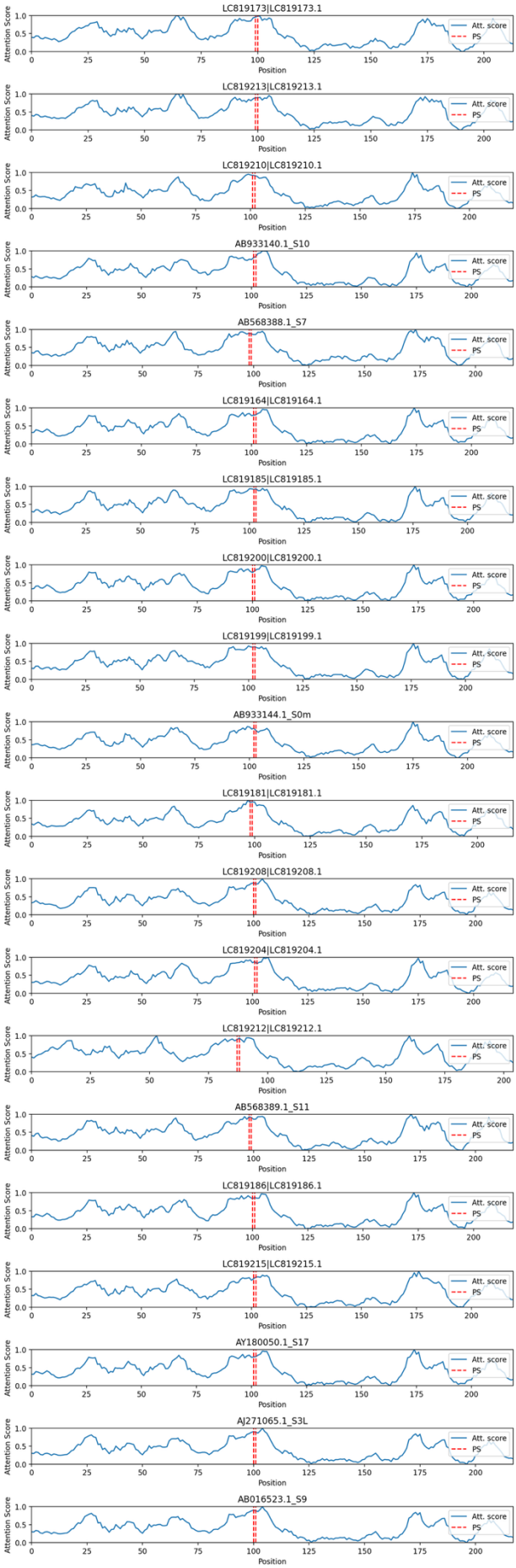

Supplementary Fig. 25: Comparison of MuLAN attention scores and positively selected sites across *Petunia* S-RNase sequences. MuLAN attention scores (blue) are shown along the amino acid sequences of several S-RNases. Vertical red lines mark positions inferred to be under positive selection (posterior probability > 0.95, CodeML analysis). Positively selected sites coincide with peaks in attention scores.

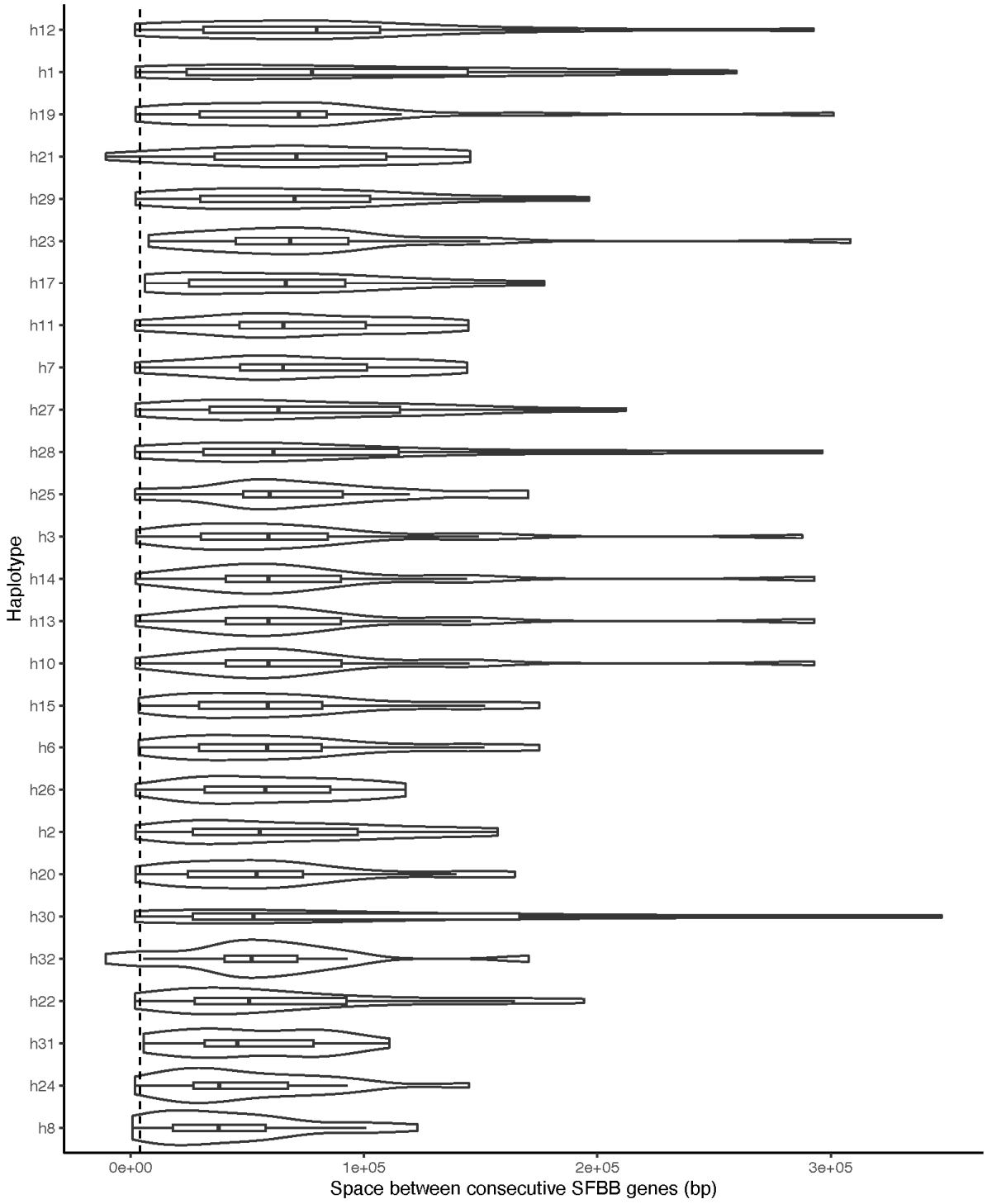

Supplementary Fig. 26: Distribution of intergenic distances between adjacent SFBB genes across S-locus haplotypes. Violin plots show the full distribution of distances (in base pairs), while boxplots indicate the median (horizontal line) and interquartile range. Haplotypes are ordered according to their median spacing. The dashed vertical line marks the 4 kb threshold, used as a reference for genomic proximity.

Supplementary text 1: SFBB families' determination and validation

To determine SFBB families of the 500 complete SFBB sequences, the amino acid sequences were aligned with sequences from the database (Supplementary Table 5), and phylogeny was constructed with 1000 bootstraps. *Eriobotya japonica* (Loquat) Fbox sequence (accession AGM21636.1) was used as an outgroup. Then, Ward hierarchical clustering (Ward, 1963) based on cophenetic distances between tree nodes (R package *stats,*) as well as orthogroups determination using Orthofinder (Emms & Kelly, 2019) were applied. Ward clustering segregated SFBB sequences in 18 groups while Orthofinder defined 16 orthogroups (Fig. 1). The main difference is that a big Orthofinder orthogroup contains 3 Ward groups.

We took advantage of publicly available SFBB gene accessions, for which the family they belong is known, to determine the family of SFBB genes identified from the assemblies we used. In most cases, public accessions, tagged with identical SFBB families, clustered together, allowing us, to attribute the SFBB family to all the cluster. But in some cases, we found that public accessions tagged with identical SFBB families, belong to several groups in our phylogeny. For instance, public accessions tagged with SFBB3 family, are found in two distant groups (Fig. 1). Public accessions tagged with SFBB1 family clustered together in our phylogenetic tree (Fig. 1). However, hierarchical clustering and Orthofinder allowed to split the group they form into two groups. The same conclusions can be made for public accessions tagged with SFBB8 family (Fig. 1).

To validate that these families should indeed be divided into two distinct groups, we compared the pairwise similarity distribution among sequences, considering both inter- and intra-group sequence similarity. We observed that sequences within each proposed subgroup displayed significantly higher similarity to one another compared to sequences from the other subgroup, supporting the hypothesis of functional divergence between these groups. Furthermore, when examining gene structure and conserved motifs, we identified differences that were consistent with the proposed division. This evidence collectively supports the reclassification of SFBB1, SFBB3, and SFBB8 families into two distinct families each, respectively SFBB1 and SFBB15, SFBB3 and SFBB4, SFBB8 and SFBB13 (Fig. 2, A,B and C).

On the contrary, families SFBB4 and SFBB12 can be brought together. Computing intra-family identity percentages considering that these two families form only one, showed that all intra-superfamily identity percentages are higher than 90% (Fig. 2,D). For families SFBB9 and SFBB10, Ward hierarchical clustering and Orthofinder defined two groups (Fig. 1), but whose limits are not the same as original SFBB families. The best thing to do is probably to redefine SFBB9 and SFBB10 boundaries, as the Ward groups and orthogroups are supported by branch bootstrap of 100%. Finally, some new families were created because no SFBBs with family associated was present in some groups. Eighteen updated SFBB families were finally defined (Table 1, Figure 1). SFBB genes annotated on *Malus* haplotypes, coordinates and families are synthetized in Supplementary Table 6.

Table 1: Original and updated SFBB families, based on Ward hierarchical clustering, Orthofinder results and phylogenetic relationships among SFBB protein sequences.

Original SFBB families	**Updated SFBB families proposition**	**Supported by**
SFBB1	SFBB1	Ward, Orthofinder, phylogeny, identity percentages
	SFBB15	Ward, Orthofinder, phylogeny, identity percentages
SFBB2	SFBB2	Ward, Orthofinder, phylogeny, identity percentages
SFBB3	SFBB3	Ward, Orthofinder, phylogeny, identity percentages
	SFBB4	Ward, Orthofinder, phylogeny, identity percentages
	SFBB17	Ward, Orthofinder, phylogeny, identity percentages
SFBB8	SFBB8	Ward, phylogeny, identity percentages
	SFBB13	Ward, phylogeny, identity percentages
SFBB4	SFBB12	Ward, phylogeny, identity percentages
SFBB12		
SFBB9	~SFBB9	Ward, Orthofinder, phylogeny, identity percentages
SFBB10	~SFBB10	Ward, Orthofinder, phylogeny, identity percentages
SFBB11	SFBB11	Ward, Orthofinder, phylogeny, identity percentages
SFBB5	SFBB5	Ward, phylogeny, identity percentages
SFBB6	SFBB6	Ward, phylogeny, identity percentages
SFBB7	SFBB7	Ward, phylogeny, identity percentages
-	SFBB14	Ward, orthofinder, phylogeny, identity percentages
-	SFBB16	Ward, Orthofinder, phylogeny, identity percentages
-	SFBB18	Ward, Orthofinder, phylogeny, identity percentages

Considering these updated SFBB families, their presence was checked in each haplotype (figure 1, B). In each haplotype, zero to two genes of each family of *SFBB* were identified. Since some S alleles are

represented in this dataset by multiple haplotypes, it was possible to compare them, and observe that some SFBB families are absent from all haplotypes with the same S allele. For instance, SFBB11 is absent from all MdS4 (h20 and h22) and MdS5 (h2 and h26) haplotypes. SFBB2 family is absent from all MdS2 haplotypes except h23 (h3, h10, h13 and h14). Absent SFBB families'products could target theses S-RNases. Concerning haplotypes from S allele MdSf, all identified SFBB families are present, suggesting that the SFBB family whose products target this S-RNase was not identified from our dataset, or that one of the SFBB families identified contain unfunctional products (although the protein sequences are complete).

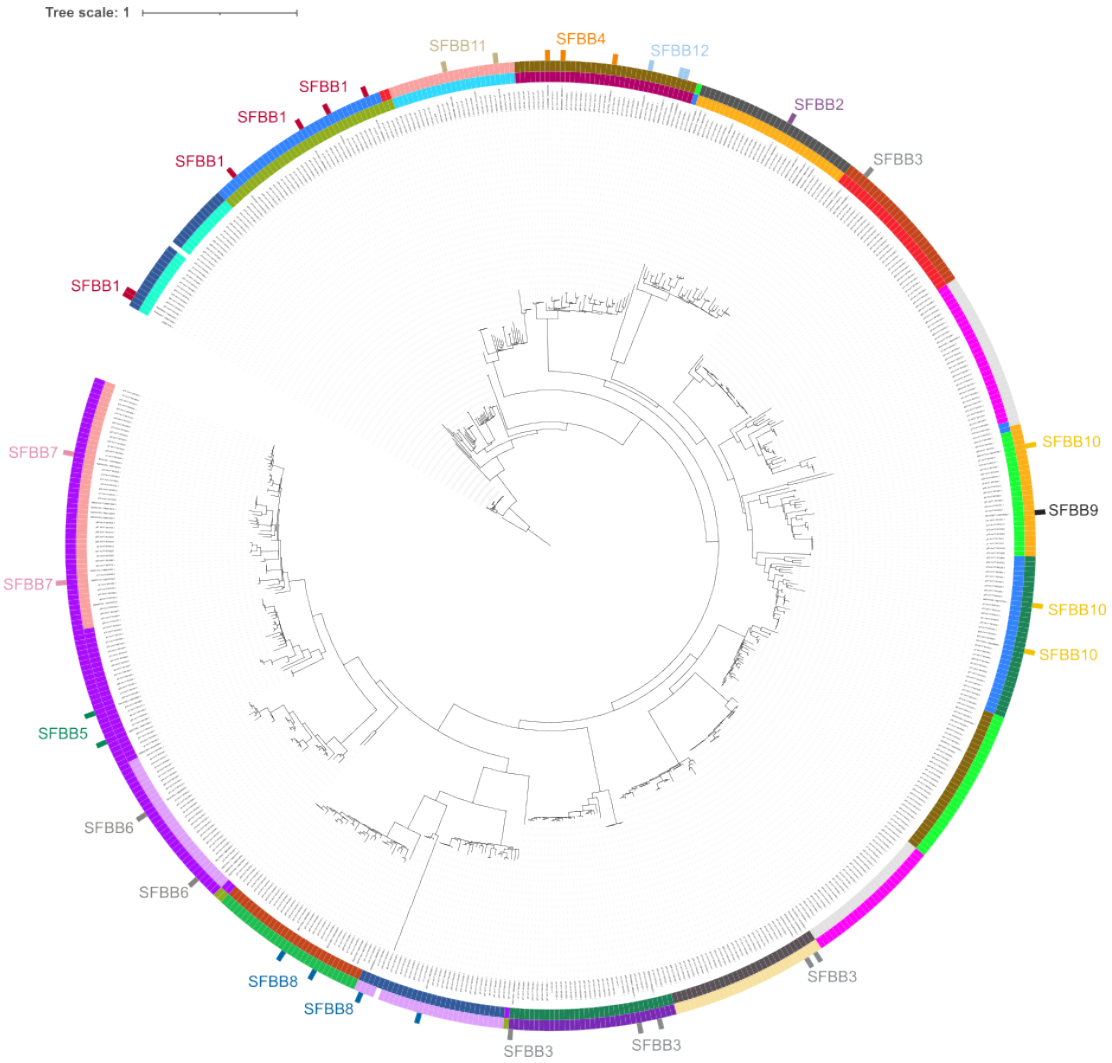

Fig. 1: SFBB clustering results from Ward hierarchical clustering (k=18) (Ward, 1963) and Orthofinder (Emms & Kelly, 2019). In this circular phylogenetic tree, the innermost layer represents the families determined using Ward's method. The intermediate layer corresponds to families identified through Orthofinder. The outermost layer, when available, indicates the known families associated with the public accessions. This visualization highlights the consistency between the different approaches and known classifications.

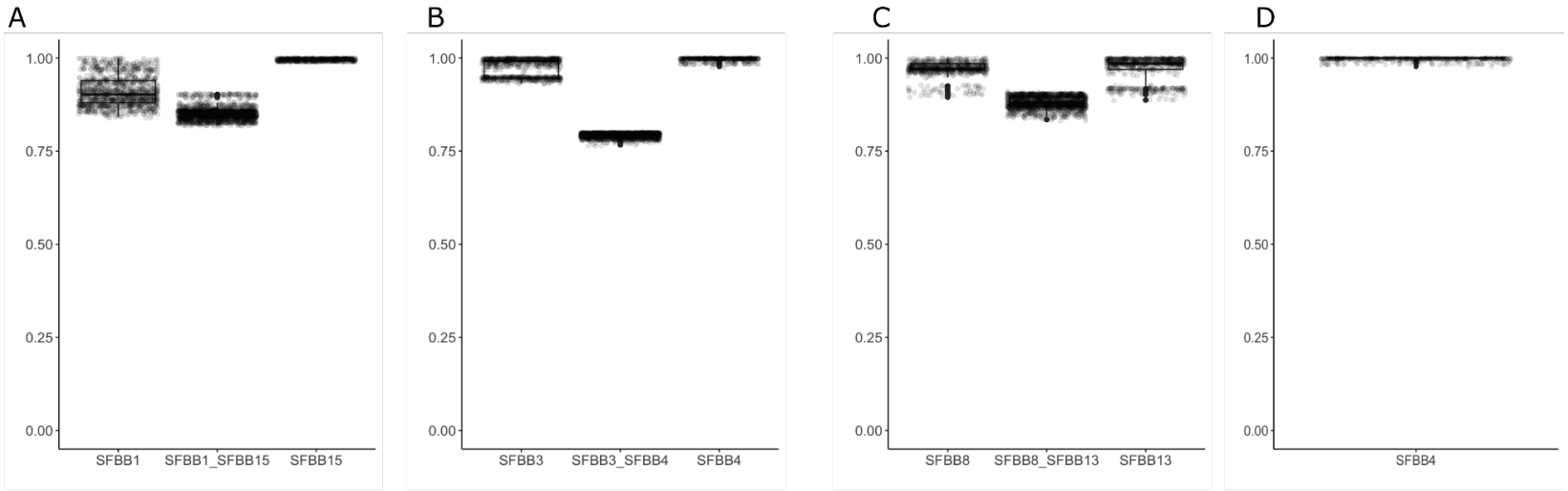

Fig. 2: Pairwise similarity distribution of SFBB gene groups before and after proposed reclassification. Boxplots display the pairwise similarity values among sequences within and between different SFBB groups. (A) SFBB1 group and its proposed subdivision into SFBB1 and SFBB15. (B) SFBB3 group and its proposed subdivision into SFBB3 and SFBB4. (C) SFBB8 group and its proposed subdivision into SFBB8 and SFBB13. (D) SFBB4 group, resulting from the merging of two previously separate families. For (D), the high pairwise similarity observed among sequences supports the merging of these two families into a single SFBB4 family. Each boxplot represents the distribution of pairwise similarity values within the corresponding group or subgroup, with the proposed subdivisions and merging reflecting patterns of sequence similarity consistent with functional or evolutionary divergence.

References:

Emms, D. M., & Kelly, S. (2019). OrthoFinder: Phylogenetic orthology inference for comparative genomics. *Genome Biology*, *20*(1). https://doi.org/10.1186/s13059-019-1832-y

Ward, J. H. (1963). Hierarchical Grouping to Optimize an Objective Function. *Journal of the American Statistical Association*, *58*(301), 236–244. https://doi.org/10.1080/01621459.1963.10500845

Supplementary text 2: Details on dataset used, DNA extraction, PacBio sequencing, assembly of the new genomes, TEs and genes annotation

Our dataset included 15 already available haplotype assemblies and 12 new sequenced haplotypes from which only chromosome 17 were kept for this study as this chromosome hosts the SI loci in *Malus* (Aguiar et al., 2015). All high-quality assembled genomes of apples available in 2022 were retrieved from public repositories. One haplotype from the *M. domestica* double-haploid GDDH13 reference genome (Daccord et al., 2017), two phased haplotypes of a Gala cultivar (Sun et al., 2020), two available phased haplotypes of a Fuji cultivar (Li et al., 2024) were used. For cultivars Red Delicious (Han et al., 2017), Honeycrisp (Khan et al., 2022), Hanfu (Qin et al., 2023), Brown Snout, Costard, Bardsey Island and Newtons (Könyves et al., 2022), only one phased haplotype was available, and used in this study. In the same way, for individuals *M. sieversii* native to Central Asia (Sun et al., 2020), *M. sylvestris,* native to Germany (Sun et al., 2020), and native to England (Ruhsam et al., 2022), only one phased haplotype was available and collected for this study. In total, 12 *M. domestica,* two *M. sylvestris* and one *M. sieversii* haplotypes were therefore retrieved from public repositories (Supplementary Table 1).

To complete this dataset, *M. sylvestris* individuals from Austria, Denmark, France and Romania, one *M. orientalis* individual native to Armenia, and one Spanish Cider *M. domestica* cultivar, were grown in IDEEV facilities, in order to sequence their genomes sequenced using PacBio Sequel II. Assembly pipeline used allowed us to have the two parental haplotypes for these genotypes, so twelve supplementary haplotypes. Ultimately, 16 *M. domestica*, 11 *M. sylvestris*, one *M. sieversii* and two *M. orientalis* haplotypes, in total, 27 haplotypes, were available for this study.

Most individuals used to make this dataset are diploids and, in most cases, two assembled haplotypes were obtained by individual (double haploid Golden Delicious, tri-haploid Hanfu, Gala and Fuji cultivars, the cider individual, *the M. orientalis* individual, the *M. sieversii* individual and the four *M. sylvestris* individuals grown at IDEEV). For eight diploids genotypes (Double haploid golden delicious, Hanfu, Red delicious, Honeycrisp, Brown snout, Costard, Bardsey Island and Newtons cultivars, *M. sieversii* and *M. sylvestris* from previous studies), we only have one assembled haplotype. In total, 14 haplotypes of *M. domestica*, 10 haplotypes of *M. sylvestris*, one haplotype of *M. sieversii* and two haplotypes of *M. orientalis* were used for further analyses (Supplementary table 1). For convenience, all haplotypes were identifed with id from h1 to h32. Finally, two haplotypes were collected from haploids individuals: the double haploid Golden Delicious individual used to construct the GDDH13 *M. domestica* reference genome (Daccord et al., 2017), and the *M. domestica* cultivar Hanfu individual (Qin et al., 2023), which is a tri-haploid.

DNA extraction, libraries constructions and sequencing

For h21 to h32, Genomic DNA was extracted from whole plant material using the QIAGEN Genomic-tips 100/G kit (Cat No./ID: 10243) following the tissue protocol. Briefly, ~ 1g of plant tissue were frozen and ground in liquid nitrogen with a mortar and pestle. After 2h of lysis at 50°C and a single centrifugation step, DNA was bound to the column, washed and subsequently eluted. The eluate was desalted and concentrated by alcohol precipitation and DNA was finally resuspended in EB buffer.
DNA concentration and purity were assessed using a NanoDrop One spectrophotometer (Thermo Scientific) and a Qubit 3 Fluorometer using the Qubit dsDNA BR assay (Invitrogen), respectively. DNA integrity and fragment size distribution were evaluated using a Femto Pulse system (Agilent, Santa

Clara, CA, USA). Then, DNA was submitted to Leiden Genome Technology Center (Netherlands) for PacBio® HiFi library construction and sequencing.

Genome assemblies and scaffold anchoring

Raw PacBio reads were assembled with hifiasm (Cheng et al., 2021), with default parameters, that allowed to obtain two phased haplotypes. TIDK (Brown et al., 2025) was used to detect telomere repeats on resulting contigs. Contigs were anchored to chromosomes with ALLMAPS JCVI (Tang et al., 2015), which allows combining several genetic maps to order and orientate contigs, and using RagTag scaffold (Alonge et al., 2022), which allows to use whole-genome alignments to a reference assembly to scaffold query sequences. The comparison of agp files resulting from ALLMAPS and from RagTag was performed using homemade perl scripts available on https://github.com/CornilleEclecticLab/ART_pipeline/tree/main, and AGPTOOLS (Ricemeyer et al., 2025). Briefly, perl scripts allow to select contigs associated with a specific chromosome in several agp files, and to make a final agp file synthesizing all results. Then, this final agp file was used as input with AGPTOOLS.

Concerning ALLMAPS anchoring, a integrated genetic maps from Di Pierro et al., (2016), and from Howard et al., (2021) with SNP markers from IRSC pear Infinium® II 1 K array (Montanari et al., 2019) and the apple 20K SNP array (Bianco et al., 2014) were used. Concerning RagTag scaffold, GDDH13 genome (Daccord et al., 2017) was used as reference to scaffold assembly contigs. Only chromosome 17 was then kept for further analyses.

Gene and transposable element annotation

In order to eliminate the bias of genome annotation caused by different pipelines, gene annotation was performed using a unique pipeline. First, TEs libraries were constructed using REPET TEdenovo (Flutre et al., 2011) using 8 assemblies from several *Malus* species (GDDH13, cider, MSYL_AUT, MSYL_DNK, MSYL_FRA, MSYL_ROU, Msiev, MORI_ARM), in order to capture maximal diversity of TE content. Then, these TEs libraries were merged and redundancy was removed using PASTEC (Hoede et al., 2014). Finally, TEs were annotated in all assemblies using the constructed TEs panlibrairy, and REPET TEannot (Quesneville et al., 2005). TE sequences were softmasked from assemblies using BEDOPS (Neph et al., 2012), to convert gff files to bed files and BEDTOOLS maskfasta (Quinlan & Hall, 2010) to softmask TE sequences.

The quality of repetitive genomic regions was assessed using the LTR Assembly Index (LAI) (Quesneville et al., 2005): (1) LTRharvest in GenomeTools v1.6.2 (Ellinghaus et al., 2008) was used to de novo predict the candidate LTR-RTs (full-length LTRs retrotransposon) in the haplotypes assembly sequences for chromosome 17, and (2) LTR_retriever v2.9.5 (Ou & Jiang, 2018) was then used to combine and refactor all the candidates to get the final full-length LTR-RTs. LAI was calculated based on the formula: LAI = (intact LTR-RT length/total LTR-RT length) × 100.
LAI values in the S-loci vary among haplotypes but are mostly above 10 (Supplementary fig. 4), except in Gala haplotypes (h2 and h3), where assembly quality may not be sufficient and must lead to be careful with conclusions made on these haplotypes.

To predict genes, Helixer (Stiehler et al., 2021) was run on softmasked haplotype fasta files using land_plant as –lineage model. Gffread (Pertea & Pertea, 2020) allowed to get cds and protein sequences

for predicted genes. Finally, gene functional annotation was performed from protein sequences, using eggnog-mapper (Cantalapiedra et al., 2021; Huerta-Cepas et al., 2016, 2017).

To complete SFBB and S-RNase gene annotation, manual annotation was performed using Apollo (Dunn et al., 2019) to identify supplementary SFBB and S-RNase genes, and to check SFBB and SRNase genes structures.

References

Aguiar, B., Vieira, J., Cunha, A. E., Fonseca, N. A., Iezzoni, A., Van Nocker, S., & Vieira, C. P. (2015). Convergent Evolution at the Gametophytic Self-Incompatibility System in Malus and Prunus. *PLOS ONE*, *10*(5), e0126138. https://doi.org/10.1371/journal.pone.0126138

Alonge, M., Lebeigle, L., Kirsche, M., Jenike, K., Ou, S., Aganezov, S., Wang, X., Lippman, Z. B., Schatz, M. C., & Soyk, S. (2022). Automated assembly scaffolding using RagTag elevates a new tomato system for high-throughput genome editing. *Genome Biology*, *23*(1), 258. https://doi.org/10.1186/s13059-022-02823-7

Bianco, L., Cestaro, A., Sargent, D. J., Banchi, E., Derdak, S., Di Guardo, M., Salvi, S., Jansen, J., Viola, R., Gut, I., Laurens, F., Chagné, D., Velasco, R., Van De Weg, E., & Troggio, M. (2014). Development and Validation of a 20K Single Nucleotide Polymorphism (SNP) Whole Genome Genotyping Array for Apple (Malus × domestica Borkh). *PLoS ONE*, *9*(10), e110377. https://doi.org/10.1371/journal.pone.0110377

Brown, M. R., Manuel Gonzalez De La Rosa, P., & Blaxter, M. (2025). tidk: A toolkit to rapidly identify telomeric repeats from genomic datasets. *Bioinformatics*, *41*(2), btaf049. https://doi.org/10.1093/bioinformatics/btaf049

Cantalapiedra, C. P., Hernández-Plaza, A., Letunic, I., Bork, P., & Huerta-Cepas, J. (2021). eggNOG-mapper v2: Functional Annotation, Orthology Assignments, and Domain Prediction at the Metagenomic Scale. *Molecular Biology and Evolution*, *38*(12), 5825–5829. https://doi.org/10.1093/molbev/msab293

Cheng, H., Concepcion, G. T., Feng, X., Zhang, H., & Li, H. (2021). Haplotype-resolved de novo assembly using phased assembly graphs with hifiasm. *Nature Methods*, *18*(2), 170–175. https://doi.org/10.1038/s41592-020-01056-5

Daccord, N., Celton, J.-M., Linsmith, G., Becker, C., Choisne, N., Schijlen, E., van de Geest, H., Bianco, L., Micheletti, D., Velasco, R., Di Pierro, E. A., Gouzy, J., Rees, D. J. G., Guérif, P., Muranty, H., Durel, C.-E., Laurens, F., Lespinasse, Y., Gaillard, S., … Bucher, E. (2017). High-quality de novo assembly of the apple genome and methylome dynamics of early fruit development. *Nature Genetics*, *49*(7), 1099–1106. https://doi.org/10.1038/ng.3886

Di Pierro, E. A., Gianfranceschi, L., Di Guardo, M., Koehorst-van Putten, H. J., Kruisselbrink, J. W., Longhi, S., Troggio, M., Bianco, L., Muranty, H., Pagliarani, G., Tartarini, S., Letschka, T., Lozano Luis, L., Garkava-Gustavsson, L., Micheletti, D., Bink, M. C., Voorrips, R. E., Aziz, E., Velasco, R., … Van De Weg, W. E. (2016). A high-density, multi-parental SNP genetic map on apple validates a new mapping approach for outcrossing species. *Horticulture Research*, *3*(1), 16057. https://doi.org/10.1038/hortres.2016.57

Dunn, N. A., Unni, D. R., Diesh, C., Munoz-Torres, M., Harris, N. L., Yao, E., Rasche, H., Holmes, I. H., Elsik, C. G., & Lewis, S. E. (2019). Apollo: Democratizing genome annotation. *PLOS Computational Biology*, *15*(2), e1006790. https://doi.org/10.1371/journal.pcbi.1006790

Ellinghaus, D., Kurtz, S., & Willhoeft, U. (2008). LTRharvest, an efficient and flexible software for de novo detection of LTR retrotransposons. *BMC Bioinformatics*, *9*(1), 18. https://doi.org/10.1186/1471-2105-9-18

Flutre, T., Duprat, E., Feuillet, C., & Quesneville, H. (2011). Considering Transposable Element Diversification in De Novo Annotation Approaches. *PLoS ONE*, *6*(1), e16526. https://doi.org/10.1371/journal.pone.0016526

Han, M., Sun, Q., Zhou, J., Qiu, H., Guo, J., Lu, L., Mu, W., & Sun, J. (2017). Insertion of a solo LTR retrotransposon associates with spur mutations in 'Red Delicious' apple (Malus × domestica). *Plant Cell Reports*, *36*(9), 1375–1385. https://doi.org/10.1007/s00299-017-2160-x

Hoede, C., Arnoux, S., Moisset, M., Chaumier, T., Inizan, O., Jamilloux, V., & Quesneville, H. (2014). PASTEC: An Automatic Transposable Element Classification Tool. *PLoS ONE*, *9*(5), e91929. https://doi.org/10.1371/journal.pone.0091929

Howard, N. P., Troggio, M., Durel, C.-E., Muranty, H., Denancé, C., Bianco, L., Tillman, J., & Van De Weg, E. (2021). Integration of Infinium and Axiom SNP array data in the outcrossing species Malus × domestica and causes for seemingly incompatible calls. *BMC Genomics*, *22*(1), 246. https://doi.org/10.1186/s12864-021-07565-7

Huerta-Cepas, J., Forslund, K., Coelho, L. P., Szklarczyk, D., Jensen, L. J., von Mering, C., & Bork, P. (2017). Fast Genome-Wide Functional Annotation through Orthology Assignment by eggNOG-Mapper. *Molecular Biology and Evolution*, *34*(8), 2115–2122. https://doi.org/10.1093/molbev/msx148

Huerta-Cepas, J., Szklarczyk, D., Forslund, K., Cook, H., Heller, D., Walter, M. C., Rattei, T., Mende, D. R., Sunagawa, S., Kuhn, M., Jensen, L. J., von Mering, C., & Bork, P. (2016). eggNOG 4.5: A hierarchical orthology framework with improved functional annotations for eukaryotic, prokaryotic and viral sequences. *Nucleic Acids Research*, *44*(D1), D286–D293. https://doi.org/10.1093/nar/gkv1248

Khan, A., Carey, S. B., Serrano, A., Zhang, H., Hargarten, H., Hale, H., Harkess, A., & Honaas, L. (2022). A phased, chromosome-scale genome of 'Honeycrisp' apple (Malus domestica). *Gigabyte*, *2022*, 1–15. https://doi.org/10.46471/gigabyte.69

Könyves, K., Mian, S., Johns, J., Royal Botanic Garden Edinburgh Genome Acquisition Lab, Royal Botanic Gardens Kew Genome Acquisition Lab, Darwin Tree of Life Barcoding collective, Wellcome Sanger Institute Tree of Life programme, Wellcome Sanger Institute Scientific Operations: DNA Pipelines collective, Tree of Life Core Informatics collective, Ruhsam, M., Leitch, I. J., & Darwin Tree of Life Consortium. (2022). The genome sequence of the apple, Malus domestica (Suckow) Borkh., 1803. *Wellcome Open Research*, *7*, 297. https://doi.org/10.12688/wellcomeopenres.18646.1

Li, W., Chu, C., Li, H., Zhang, H., Sun, H., Wang, S., Wang, Z., Li, Y., Foster, T. M., López-Girona, E., Yu, J., Li, Y., Ma, Y., Zhang, K., Han, Y., Zhou, B., Fan, X., Xiong, Y., Deng, C. H., …

Han, Z. (2024). Near-gapless and haplotype-resolved apple genomes provide insights into the genetic basis of rootstock-induced dwarfing. *Nature Genetics*, *56*(3), 505–516. https://doi.org/10.1038/s41588-024-01657-2

Montanari, S., Bianco, L., Allen, B. J., Martínez-García, P. J., Bassil, N. V., Postman, J., Knäbel, M., Kitson, B., Deng, C. H., Chagné, D., Crepeau, M. W., Langley, C. H., Evans, K., Dhingra, A., Troggio, M., & Neale, D. B. (2019). Development of a highly efficient Axiom™ 70 K SNP array for Pyrus and evaluation for high-density mapping and germplasm characterization. *BMC Genomics*, *20*(1), 331. https://doi.org/10.1186/s12864-019-5712-3

Neph, S., Kuehn, M. S., Reynolds, A. P., Haugen, E., Thurman, R. E., Johnson, A. K., Rynes, E., Maurano, M. T., Vierstra, J., Thomas, S., Sandstrom, R., Humbert, R., & Stamatoyannopoulos, J. A. (2012). BEDOPS: High-performance genomic feature operations. *Bioinformatics*, *28*(14), 1919–1920. https://doi.org/10.1093/bioinformatics/bts277

Ou, S., Chen, J., & Jiang, N. (2018). Assessing genome assembly quality using the LTR Assembly Index (LAI). *Nucleic Acids Research*. https://doi.org/10.1093/nar/gky730

Ou, S., & Jiang, N. (2018). LTR_retriever: A Highly Accurate and Sensitive Program for Identification of Long Terminal Repeat Retrotransposons. *Plant Physiology*, *176*(2), 1410–1422. https://doi.org/10.1104/pp.17.01310

Pertea, G., & Pertea, M. (2020). GFF Utilities: GffRead and GffCompare. *F1000Research*, *9*, 304. https://doi.org/10.12688/f1000research.23297.2

Qin, S., Xu, G., He, J., Li, L., Ma, H., & Lyu, D. (2023). A chromosome-scale genome assembly of Malus domestica, a multi-stress resistant apple variety. *Genomics*, *115*(3), 110627. https://doi.org/10.1016/j.ygeno.2023.110627

Quesneville, H., Bergman, C. M., Andrieu, O., Autard, D., Nouaud, D., Ashburner, M., & Anxolabehere, D. (2005). Combined Evidence Annotation of Transposable Elements in Genome Sequences. *PLoS Computational Biology*, *1*(2), e22. https://doi.org/10.1371/journal.pcbi.0010022

Quinlan, A. R., & Hall, I. M. (2010). BEDTools: A flexible suite of utilities for comparing genomic features. *Bioinformatics*, *26*(6), 841–842. https://doi.org/10.1093/bioinformatics/btq033

Ricemeyer, E. S., Carroll, R. A., & Warren, W. C. (2025). Agptools: A utility suite for editing genome assemblies. *Bioinformatics*, *41*(7), btaf388. https://doi.org/10.1093/bioinformatics/btaf388

Ruhsam, M., Bell, D., Hart, M., Hollingsworth, P., Royal Botanic Garden Edinburgh Genome Acquisition Lab, Darwin Tree of Life Barcoding collective, Wellcome Sanger Institute Tree of Life programme, Wellcome Sanger Institute Scientific Operations: DNA Pipelines collective, Tree of Life Core Informatics collective, & Darwin Tree of Life Consortium. (2022). The genome sequence of the European crab apple, Malus sylvestris (L.) Mill., 1768. *Wellcome Open Research*, *7*, 296. https://doi.org/10.12688/wellcomeopenres.18645.1

Stiehler, F., Steinborn, M., Scholz, S., Dey, D., Weber, A. P. M., & Denton, A. K. (2021). Helixer: Cross-species gene annotation of large eukaryotic genomes using deep learning. *Bioinformatics*, *36*(22–23), 5291–5298. https://doi.org/10.1093/bioinformatics/btaa1044

Sun, X., Jiao, C., Schwaninger, H., Chao, C. T., Ma, Y., Duan, N., Khan, A., Ban, S., Xu, K., Cheng, L., Zhong, G.-Y., & Fei, Z. (2020). Phased diploid genome assemblies and pan-genomes provide insights into the genetic history of apple domestication. *Nature Genetics*, *52*(12), 1423–1432. https://doi.org/10.1038/s41588-020-00723-9

Tang, H., Zhang, X., Miao, C., Zhang, J., Ming, R., Schnable, J. C., Schnable, P. S., Lyons, E., & Lu, J. (2015). ALLMAPS: Robust scaffold ordering based on multiple maps. *Genome Biology*, *16*(1), 3. https://doi.org/10.1186/s13059-014-0573-1